University of Southampton

Faculty of Engineering, Science and Mathematics

Numerical Investigation of Slat Noise Attenuation using Acoustic Liners

Zhaokai Ma

Submitted for the degree of
Doctor of Philosophy

January 2008

Abstract

Noise generated by high-lift devices such as slats on a wing is a major contributor to the overall airframe noise during the landing approach of a commercial aircraft. In this work the concept of attenuating slat noise using absorptive acoustic liners in the slat/main element gap is explored using a time domain computational aeroacoustic (CAA) technique. The aims of the development and application of the computational method are to reveal the mechanism of the slat noise generation and demonstrate the feasibility of controlling the slat noise using acoustic liners. A model scale three-element high-lift airfoil comprising a main element, a leading edge slat and trailing edge flap geometry is employed in the investigation. Numerical simulations are performed to investigate the generation and far field propagation of the slat noise. A numerical approach is developed that combines near field flow computation with an integral radiation model to predict the far field acoustic signal. A time domain impedance boundary condition (TDIBC) is implemented to simulate the effect of the liner material directly.

Both the high frequency tonal noise and low frequency broadband noise generated from the slat are investigated.

For the high frequency tonal noise, an unsteady Reynolds-averaged Navier-Stokes (URANS) simulation using high-order spatial and temporal schemes for the wing without acoustic liners shows the presence of vortex shedding and associated high frequency acoustic sources behind the slat trailing edge. To evaluate the mitigating performance of liners on the generated noise and find an optimized liner impedance value, an exercise is conducted on a range of liner impedance values by solving the linearized Euler equations (LEE) for a modeled acoustic source located at the trailing edge of the slat to find a optimized one. Using the optimized impedance value, URANS computations for the wing with liner treatment are conducted. The results show that acoustic liners on the slat cove and on the main element can provide useful attenuation of the high frequency slat trailing edge noise.

For the low frequency broadband noise, the noise sources are calculated by both the pseudo-laminar zonal method and the stochastic noise generation and radiation

(SNGR) approach. The pseudo-laminar zonal calculation is basically an URANS calculation with the two-equation shear stress transport (SST) $\kappa - \omega$ model to model the effect of turbulence and a region in the slat cove is set as laminar zone. In the SNGR approach broadband sources of noise are modeled using stochastic noise generation method from a numerical solution of the steady Reynolds-averaged Navier-Stokes (RANS) equations using the $\kappa - \omega$ closure and then the acoustic field is calculated by solving the acoustic perturbation equations (APE) using high-order spatial and temporal schemes. By comparing the results of pseudo-laminar method and that of SNGR approach, the SNGR method has been shown to be a potentially useful method to model the generation of broadband slat noise and to investigate the attenuation of slat gap acoustic liners, for which the interest is in changes of noise level rather than the absolute value. The broadband noise attenuation effect of the acoustic liner treatment is studied by applying a broadband TDIBC to the acoustic field obtained by the SNGR method. The far-field directivity is obtained through an integral surface solution of Ffowcs Williams and Hawkings (FW-H) equation. Predictions for a non-optimized acoustic liner show a moderate amount of attenuation.

To accurately simulate the broadband noise generation and radiation, a LES using a high-order spatial scheme and implicit temporal integration is conducted for the high-lift configuration with slat deployed and the calculated results show the characteristic of the unsteady flow and the mechanisms of the broadband noise generation. The recorded noise sources are then used to drive the APE to simulate the noise propagation and the attenuation by acoustic liners. The source driven APE results agree well with that of LES in term of far field directivity and sound pressure level. Similar to the SNGR simulation, a moderate amount of attenuation is achieved by the acoustic liner treatment.

Acknowledgements

Foremost, I would like to acknowledge my supervisor, Professor Xin Zhang for his valuable guidance and huge encouragement throughout the course of my research. His professionalism and kindness make the study with him very rewarding and gratifying.

I am very grateful to Dr. Malcolm Smith for his valuable advice about the liner modeling method. I would also like to thank Dr. Xiaoxian Chen and Dr. Jae Wook Kim for their help on developing the high-order code described in this work. Thanks to Dr. Leung Chow for his patience and regular supervision and suggestions throughout the course of the project.

Thanks to my friends, Sammie, Dave, Koen, Ed and Xun for their assistance and friendship.

Finally, thanks to my parents, Ming Ma and Xiangfan Zhang, for their constant support and also to my wife, Xueman Xu, for her tremendous support and encouragement throughout the duration of my studies.

Nomenclature

Abbreviations

2D	Two-Dimensional
3D	Three-Dimensional
AB	Adams-Bashforth
APE	Acoustic Perturbation Equations
CAA	Computational Aeroacoustic
CFD	Computational Fluid Dynamics
CFL	Courant-Friedrichs-Levy
CFL3D	Computational Fluid Dynamics Laboratory Three-Dimensional
DES	Detached Eddy Simulation
DNS	Direct Numerical Simulation
DRP	Dispersion-Relation-Preserving
EET	Energy Efficient Transport
FFT	Fast Fourier Transform
FW-H	Ffowcs Williams and Hawkings
LDDRK	Low-Dissipation and Low-Dispersion Runge-Kutta
LEE	Linearized Euler Equations
LES	Large Eddy Simulation

MAE	Matched Asymptotic Expansions
NS	Navier-Stokes
PIV	Particle Image Velocimetry
PPW	Points Per Wavelength
PSD	Power Spectral Density
RANS	Reynolds-Averaged Navier-Stokes
RK	Runge-Kutta
RMS	Root Mean Square
SA	Spalart-Allmaras
SNGR	Stochastic Noise Generation and Radiation
SPL	Sound Pressure Level, with a Reference Pressure of 20 μPa
SST	Shear Stress Transport
TDIBC	Time Domain Impedance Boundary Condition
TKE	Turbulent Kinetic Energy
URANS	Unsteady Reynolds-Averaged Navier-Stokes

Greek Symbols

$\delta()$	Dirac Delta Function
δ_{ij}	Kronecker Delta
ℓ_i, ℓ_j, ℓ_k	Subgrid Scale Heat Flux Vector Components
Γ	Circulation
γ	Ratio of Specific Heat Coefficients
κ	Turbulent Kinetic Energy
Λ	Eddy-Viscosity Length Scale

$\lambda_{\hat{\mathbf{A}}}$	Eigenvalues of Flux Jacobian Matrix $\hat{\mathbf{A}}$
$\lambda_{\hat{\mathbf{B}}}$	Eigenvalues of Flux Jacobian Matrix $\hat{\mathbf{B}}$
$\lambda_{\hat{\mathbf{C}}}$	Eigenvalues of Flux Jacobian Matrix $\hat{\mathbf{C}}$
μ	Molecular Viscosity
ν_t	Turbulent Eddy Viscosity
ω	Specific Energy Dissipation Rate, or Angular Frequency
ϕ_M	Magnitude of the Rate-of-Strain Tensor
ϕ_{ij}	Rate-of-Strain Tensor
ρ	Fluid Density
σ_{ij}	Viscous Stress Tensor
τ	Pseudo-Time
τ_{ij}	Subgrid Scale Viscous Stress Tensor
Υ	Reflection Coefficient
ξ, η, ζ	Generalized Coordinates
ζ_L	Lagrangian Coordinate System

Alphanumeric Symbols

$\hat{\mathbf{A}}, \hat{\mathbf{B}}, \hat{\mathbf{C}}$	Flux Jacobian Matrixes
$\hat{\mathbf{F}}, \hat{\mathbf{G}}, \hat{\mathbf{H}}$	Inviscid Fluxes of Navier-Stokes Equations
$\hat{\mathbf{F}}_v, \hat{\mathbf{G}}_v, \hat{\mathbf{H}}_v$	Viscous Fluxes of Navier-Stokes Equations
$\hat{\mathbf{n}}$	Unit Outward Normal Vector to Surface, with Components $\hat{n}_i$
$\hat{\mathbf{Q}}$	Solution Vector of Navier-Stokes Equations
$\hat{\mathbf{r}}$	Unit Vector in the Radiation Direction, with Components $\hat{r}_i$
$\mathbf{I}$	Identity Matrix

$\mathbf{L}$	Lamb Vector
$\mathbf{q}_m$	Source Term Vector of Acoustic Perturbation Equations
$\mathbf{u}$	Cartesian Velocity Vector
$\mathbf{x}$	Observer Position Vector
$\mathbf{y}$	Source Position Vector
A	Space Averaged Attenuation
C	Chord Length
c	Sound Speed
c_p	Specific Heat Coefficient under Constant Pressure
c_v	Specific Heat Coefficient under Constant Volume
C_{sgs}	Eddy-Viscosity Model Constant
E	Specific Total Energy
e	Specific Internal Energy Density
f	Frequency
G	Generic Green's Function
G_0	Free Space Green's Function
$H()$	Heaviside Function
J	Coordinates Transformation Jacobian
J_2	Second-Order Bessel Functions of the First Kind
k_T	Thermal Conductivity Coefficient
L	Characteristic Length
L_i	Dipole Source Vector of FW-H Equation
p	Static Pressure
Pr	Prandtl Number

Pr_t	Turbulent Prandtl Number
q_i, q_j, q_k	Heat Flux Vector Components
R	Acoustic Resistance
R_0	Modeled Acoustic Resistance
Re	Reynolds Number
Re_D	Reynolds Number based on a Characteristic Diameter D
Re_L	Reynolds Number based on a Characteristic Length L
St	Strouhal number
T	Temperature
t	Time
T_{ij}	Lighthill Stress Tensor
U, V, W	Contravariant Velocities
u, v, w	Cartesian Velocity Components
U_i	Monopole Source Vector of FW-H Equation
u_i, u_j, u_k	Cartesian Velocity Vector Components $(u_1, u_2, u_3) \equiv (u, v, w)$
u_n	Normal Velocity
v_i, v_j, v_k	Integration Surface Cartesian Velocity Vector Components
V_M	Magnitude of Velocity Vector $\mathbf{u}$
X	Acoustic Reactance
x, y, z	Cartesian Coordinates
x_i, x_j, x_k	Cartesian Coordinates Vector Components $(x_1, x_2, x_3) \equiv (x, y, z)$
X_{-1}	Modeled Acoustic Stiffness
X_1	Modeled Acoustic Mass
Y_2	Second-Order Bessel Functions of the Second Kind

Z	Acoustic Impedance

Subscript or Superscript

$()'$	Perturbation Value
$()^*$	Reference Value
$()_0$	Mean Flow Value
$()_\infty$	Freestream Value

Contents

List of Figures

List of Tables

Chapter 1

Introduction

1.1 Overview

The noise defined as unpleasant, unexpected or undesired sound, is a major issue related to our modern life. Despite significant progress in reducing aircraft noise over the past thirty years, the increasing passenger growth has resulted in the increasing annoyance. The aircraft noise contains a broad range of noise sources, including jet noise, turbomachinery noise, combustor noise and airframe noise. Although the engine noise dominates during takeoff, the airframe noise is comparable to, or sometimes greater than the engine noise during final approach.

Airframe noise is defined as the nonpropulsive components of noise radiated from a flying aircraft. Past studies that focused on airframe noise identified high-lift devices and landing gear as dominant noise producing components [1, 2] (Figure 1.1). The significant contribution of the flows around the leading edge slat of a commercial aircraft to the airframe noise during approach and landing [3, 4, 5] motivates this research project to identify the mechanisms of leading edge slat noise and passively control these acoustic sources.

The thesis focuses on the numerical simulation of the noise generated by unsteady turbulent flows around the slat. Physical issues concerning the present studies are the mechanisms of noise generation and its propagation as well as the passive control of the acoustic noises using acoustic liners. All those problems are analyzed by using computational tools which combine the flow simulations with the acoustics calculations.

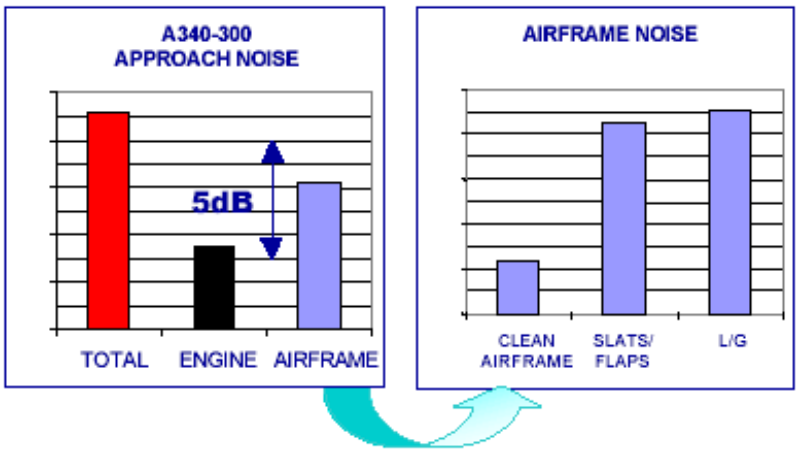

Figure 1.1: Approach noise of an Airbus A340–300 aircraft [1].

1.2 Literature Review

CAA methods relevant to this work are surveyed below. With respect to each topic there are different methods that are compared through the review, which helps to identify the most suitable methods to be employed in the rest of this work.

1.2.1 Aerodynamic Sound Theory

Sound is vibrations transmitted through an elastic solid or a liquid or gas, with frequencies in the approximate range of 20 to 20,000 Hz, capable of being detected by human organs of hearing. The subject of this report is within the area of aeroacoustics which deals with the generation of sound by flow, and its propagation within the flow. Since the pressure fluctuations within the airflow are mainly balanced by fluctuations of fluid acceleration, it is not clear what proportion of their energy is radiated as sound. Essential problems are: how the flow can generate noise and for a given fluid flow, how to estimate the sound radiated from it.

1.2.1.1 Noise Generation by Flow

The noise can be regarded as a pressure disturbance which propagates through a fluid at the acoustic velocity. The disturbances are usually small amplitude compared with the ambient atmospheric pressure and are emanated from certain sources.

For the noise generated aerodynamically, the sources maybe the free fluid motion or fluid passing a solid body. An Example of sources associated with free fluid motion is noise generated by a jet. In this phenomenon, the fine scale turbulence or small

eddies generate one of the dominant component of noise that radiates to the sideline directions [6]. A schematic of a turbulent jet is displayed in Figure 1.2. Downstream of the nozzle there is an annular shear-layer (turbulent mixing layer) which surrounds the potential core region of the jet. The mixing layer spreads outward and inward. The inward spreading of the mixing layer define the length of the potential core. The transition region is located at the end of the potential core. Downstream of this point the centerline velocity starts to decay. The turbulence mixing layer and the transition region are regarded as the noise generation region.

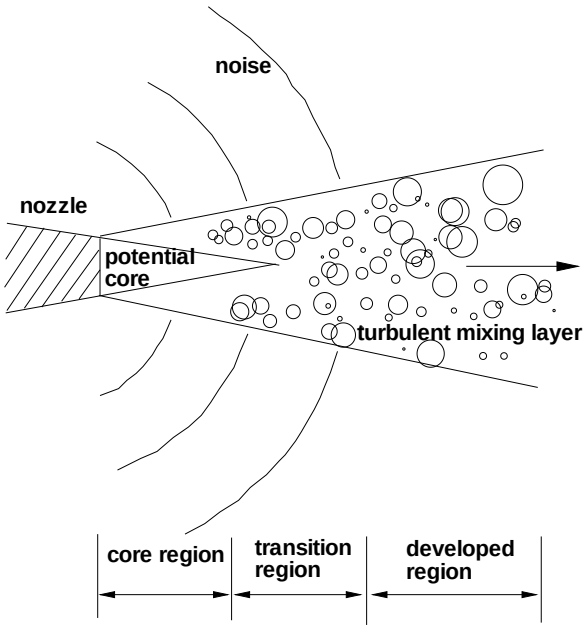

Figure 1.2: Schematic showing localized noise sources in the mixing layer of a jet; also shown are the core, transition, and developed region of the jet.

Sound sources can be generated also by the fluid flow interaction with a solid structure. The flow field around a rotor blade is shown in Figure 1.3. In this case, the boundary layer along the blade is laminar initially. Due to the high Reynolds number of the flow ($\sim O(10^6)$), the transition from the laminar to turbulent in the boundary layer is expected. Near the end of the blade, boundary layer separation is possible due to a sufficiently large adverse pressure gradient. Behind the trailing edge, due to the velocity difference between the suction and pressure surfaces, a region of absolute instability of sufficient length and growth rate may exist in the near-wake of the trailing edge. This results in periodical vortex shedding. At the tip

of the blade the pressure difference between the suction and pressure sides forms the tip vortex. All these aerodynamics phenomena contribute to the noise generation [7].

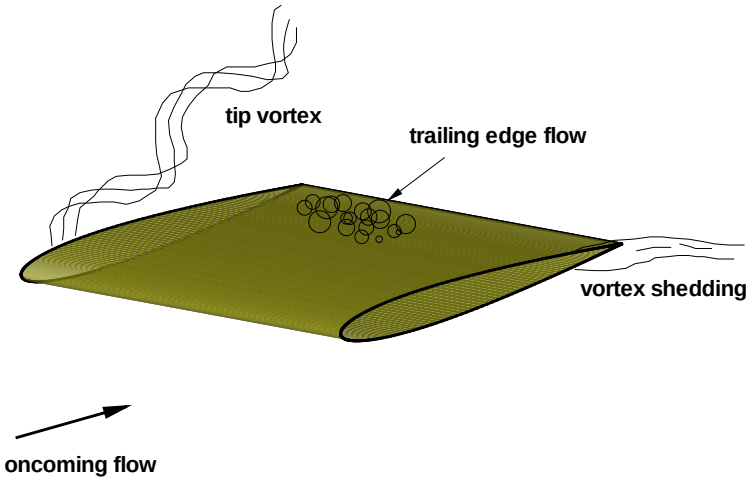

Figure 1.3: Schematic showing the possible noise sources in the flow around a rotor blade.

The flow generated noise can be described as the elementary solutions of the wave equation namely monopoles, dipoles and quadruples.

The sound produced by a monopole like acoustic source is associated with the displacement of the fluid due to the acceleration of the moving surface. The acoustic waves generated by a monopole are propagation equally in all directions. Thus, the directivity pattern looks like a circle as depicted in Figure 1.4(a).

A dipole consists of two monopoles of equal source strength and opposite phase, separated by a small distance compared with the wave length of the sources. The dipole is generated by fluctuating force acted on the solid surface. The directivity pattern of a dipole shows two lobes and it has maxima along upward and downward directions as shown in the Figure 1.4(b). At forward and backward direction the sound is totally canceled.

A quadruple consists of two identical dipoles which are opposite in phase. There are two kinds of quadruples: the lateral quadruple and the longitudinal quadruple. The axes of dipoles of the lateral quadruple do not lie on a same line, and it has a directivity with four lobes as shown in Figure 1.4(c). The lateral quadruple is associated with the shear stress and can be found in all turbulent flows. The longitudinal quadruple consist of two dipoles whose axes lie on the same line. The longitudinal quadruple has a directivity which behaviors similar to a dipole and is

associated with the normal stresses.

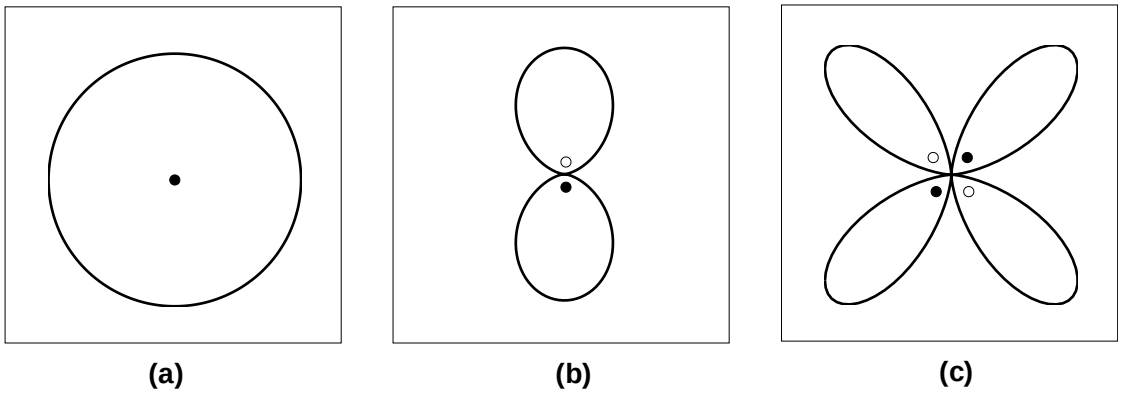

Figure 1.4: Directivity patterns for acoustic sources; (a) monopole, (b) dipole, (c) quadrupole.

1.2.1.2 The Acoustic Analogy

Lighthill's acoustic analogy was the first attempt to describe the radiation of the sound generated by a turbulent flow [8, 9]. The essential step taken by Lighthill was to incorporate, into a linear acoustic model, the non-linear features of aerodynamic sound generation through the concept of an acoustic analogy.

In his theory, Lighthill considered a fluctuation fluid flow embedded in a very large volume uniform fluid which is at rest. He rearranged the exact equations of continuity and momentum into an inhomogeneous wave equation, now known as Lighthill's equation

$$(\frac{1}{c_0^2}\frac{\partial^2}{\partial t^2} - \frac{\partial^2}{\partial x_i^2})[c_0^2(\rho - \rho_0)] = \frac{\partial^2 T_{ij}}{\partial x_i \partial x_j} \tag{1.1}$$

where ρ is the density, ρ_0 is the density of the uniform fluid, c_0 is the sound speed of the uniform fluid and the T_{ij} is the Lighthill stress tensor[1] which is given by

$$T_{ij} = \rho u_i u_j - \sigma_{ij} + [(p - p_0) - c_0^2(\rho - \rho_0)]\delta_{ij} \tag{1.2}$$

where δ_{ij} is Kronecker delta, u_i, p and σ_{ij} are the velocity components, the static pressure and the viscous stresses respectively and p_0 is the static pressure of the

[1]Suffix notation for vector components is used here and throughout this report, with the usual convention of vector and tensor analysis that terms containing a repeated suffix are to be regarded as summed over all possible values of the suffix.

uniform fluid.

By design, the left side of Eq. 1.1 represents acoustic wave propagation. It follows, therefore, that the right side of the equation must be the sources that generate the noise field.

One important result that can be derived from the Lighthill's theory is the noise scaling law. Lighthill showed that the acoustic power radiated from a jet at low Mach number scaled with the eighth power of the jet velocity, establishing the turbulence of the jet mixing layer as the main source of noise and showing jet speed to be the principle parameter determining the overall noise.

1.2.1.3 Extensions to Lighthill's Theory

The main drawback of Lighthill's acoustic analogy is its limitation to problems where solid surfaces do not play a major role in sound generation process. The first significant extension of Lighthill's theory was developed by Curle [10], who devised a technique to include the effect of stationary solid surfaces, showing that boundary terms give rise to dipole sources of fundamentally greater acoustic efficiency than Lighthill's volume quadrupoles at sufficient low Mach number flow. Curle's theory relates the sound to integrals of surface and volume source terms and specifies precisely what these terms are. As with Lighthill's theory, once these are known, so is the sound field.

Further extension of Lighthill's theory has been proposed by Ffowcs Williams and Hawkings [11]. In the extension the fluid is divided into different regions by a integration surface which is described by the equation $f_s = 0$. Inside the integration surface, f_s is negative and outside the integration surface, f_s is positive. With the definition of the f_s and the treatment that the flow variables are regarded as generalized functions, the validity of the equation of fluid motion may be extended to all space through the use of the Heaviside function. Using the mathematical theory of general function [12] and following the same steps as used by Lighthill to derive his acoustic analogy, the continuity and momentum equations have be cast into the form of a wave equation with two surface source terms and a volume source term on the right-hand side [11]. The integration surface could be the moving solid surface or the permeable off-body surface. This flexibility makes the FW-H method an attractive technique for predicting the far field acoustic signal.

All variants of the acoustic analogy theory presented above suffer from the deficiency that they lumped the interaction of sound with its parent flow together and included in the strength and distribution of the equivalent acoustic source field. To date no acoustic analogy theory has been successful in fully isolating sound gen-

eration from the interaction of acoustic waves with turbulence and the mean flow. Nevertheless, from a computational point of view it is possible, within the accuracy limits of the computation, to evaluate any particular 'exact' source terms of an acoustic analogy and predict the radiated acoustic field. This strategy now forms the basis of much work conducted in the numerical modeling of aerodynamically generated sound.

1.2.2 Computational Aeroacoustics

In general all aeroacoustic phenomena can be described by the equations of mass, momentum and energy conservation together with the equation of state. Basically these are the compressible transient Navier-Stokes equations, which shows that aeroacoustics is a special case of fluid dynamics. Needless to say, computational fluid dynamics (CFD) methods have been very successful for the aerodynamics computation. However in order to solve the aeroacoustic problem directly it is not possible to simply use existing CFD codes and solve the transient compressible Navier-Stokes equations from the location of sound generation up to the observer (microphone position). The nature, characteristics, and objectives of aeroacoustics problems are distinctly different from those commonly encountered in aerodynamics[13, 14]. In the followings, important considerations in the numerical simulation of aeroacoustic phenomena are first summarized. A brief review of the most common methods employed in CAA is then presented.

1.2.2.1 Physical Considerations

The numerical modeling of aeroacoustic phenomena is demanding for several specific reasons. Foremost is the fact that aeroacoustic problems are, by definition, time dependent. They must, therefor, be treated time-accurately with appropriate consideration of all relevant time scales. Since the human ear is sensitive to a wide range of frequencies (e.g. 20 Hz to 20,000 Hz) simulations dealing with such problems must in general span this broad spectrum.

Another important consideration is the disparity between the energy levels of the unsteady flow fluctuations and the acoustic waves. Based on the work of Lighthill [8] it can be shown that the ratio between radiated sound power P_{sound} and mechanical flow power P_{flow} is approximately $\frac{P_{sound}}{P_{flow}} \approx 10^{-4}M^5$. This means that the radiated sound power is many orders of magnitude lower than the mechanical flow power. Due to this a numerical procedure that is desired to solve the coupled flow and acoustic field at $M = 0.1$ needs to ensure an accuracy of at least 10^{-9}. Otherwise all

inaccuracies will be observed as numerical noise. It could actually happen that the numerical procedure is 'noisier' than the flow. This large disparity between acoustic and flow variables presents a severe challenge to numerical simulation.

Most aeroacoustic problems involve multiple length scales. The length scale of the acoustic source is usually very different from the acoustic wavelength. For example, in the slat noise calculations, the discrete eddies in the slat cove region generate the dominated component of noise which is normally in the low to middle frequency band. The eddies are very small compared with the chord of slat. The acoustic wave lengths, in the other hand, are typically more than one slat chord. That is the length scale of the source region and that of the acoustic far field region can be vastly different. Computational aeroacoustic methods must be designed to deal with problems with greatly different length scales in different parts of the computational domain.

The radiation of energy to the far field is a defining feature of many aeroacoustic problems. For aerodynamics problems, flow disturbances, generally tend to decay very fast away from a body or their source of generation. So the disturbances are small at the boundary of computation. The acoustic waves, on the other hand, decay very slowly and actually reach the boundaries of a finite computation domain. The numerical modeling of such phenomena requires the introduction of artificial boundaries which avoid the reflection of outgoing sound wave back into the computation domain and thus contamination of the solution. Although such exact non-reflecting or radiation boundary conditions are known for several specific problems, the derivation of more general, efficient and suitably accurate boundary conditions remains an active area of research.

1.2.2.2 Numerical Algorithm

With the development of more powerful computers and numerical algorithm, the field of CAA has become a practical engineering and research tool. Central to this success has been the adoption of high-order accurate schemes [13]. By high-order accurate it is meant a method for which the Taylor series truncation error scales with a power greater than two of either the mesh spacing or time step. The benefit of application of high-order schemes are: 1) The high-order schemes need less points per wavelength (PPW) to solve a wave. As a result, for a given grid high-order schemes can reach higher accuracy and capture more physical phenomena; 2) The low dissipation and dispersion characteristic of high-order schemes make the accurate calculation of long propagation wave possible.

For spatial discretization, the most popular scheme used in the CAA research

is high-order finite-different schemes because of the high-accuracy and simplicity of implement. Both explicit and implicit finite-difference spatial discretization schemes are commonly used [15].

The dispersion-relation-preserving (DRP) scheme of Tam *et al.* [16] is an explicit scheme with severn-point central-difference stencil,

$$\left(\frac{\partial \varphi}{\partial x}\right)_N = \left(\frac{\sum_{i=1}^{3} a_i(\varphi_{N+i} - \varphi_{N-i})}{\Delta x}\right) \tag{1.3}$$

where φ is a scalar quantity and a_i are the coefficients of the scheme.

Application of Fourier transform to the Eq. 1.3 shows the relationship of numerical wavenumber and analytical wavenumber. Two of the coefficients a_i are chosen so that Eq. 1.3 is accurate to the fourth order while the remaining coefficient is used as an optimization parameter to minimize the integrated error between the numerical wave number and analytical wavenumber. This results in an approximation with better resolution of high wave number or short waves as compared to the formally higher order but non-optimized scheme.

Explicit schemes employ large computational stencils for accuracy, whereas implicit schemes achieve high-order accuracy by solving for the spatial derivatives as independent variables at each grid point [17]. Hixon [18, 19] derived a class of compact schemes that obtain high-order accuracy while using a very small stencil. In Hixon's approach the derivative operator D_N was split into forward, D_N^F and backward, D_N^B, operators as $D_N = (D_N^F + D_N^B)/2$, and the discretized equations were written in the compact form

$$aD_{N+1}^F + (1-a-c)D_N^F + cD_{N-1}^F \approx \frac{b\varphi_{N+1} - (2b-1)\varphi_N - (1-b)\varphi_{N-1}}{\Delta x}, \tag{1.4}$$

$$cD_{N+1}^B + (1-a-c)D_N^B + aD_{N-1}^B \approx \frac{(1-b)\varphi_{N+1} + (2b-1)\varphi_N - b\varphi_{N-1}}{\Delta x} \tag{1.5}$$

where D_N denotes the spatial derivative $(\partial\varphi/\partial x)_N$ at the mesh node N.

Coefficients of Hixon's sixth-order scheme are

$$\begin{aligned} a &= \frac{1}{2} - \frac{1}{2\sqrt{5}}, \\ b &= 1 - \frac{1}{30a}, \\ c &= 0. \end{aligned} \tag{1.6}$$

Using Hixon's scheme, only three points are needed to obtain the derivatives

and only two independent bidiagonal matrices are needed to be reversed. Ashcroft and Zhang [20] extend Hixon's prefactored concept to a wider class of compact schemes allowing the incorporation of a wavenumber based optimization process which improved the wave propagation properties of the scheme.

The time-advancement scheme can also impact on the dissipation and dispersion errors. Two of the most popular schemes in the CAA community are single-step Runge-Kutta (RK) methods and multi-step Adams-Bashforth (AB) schemes.

Hu *et al.* [21] showed that the classical RK schemes require time steps much smaller than those allowed by the stability restriction for the numerical solution of a wave propagation problem to be accurate after long integration times. They developed the low-dissipation and low-dispersion Runge-Kutta (LDDRK) schemes whose coefficients were optimized to minimize the dissipation and dispersion error. Consequently, much larger time steps can be used which increases the computational efficiency.

Tam *et al.* [16] developed an optimized four-level Adams-Bashforth type time-marching scheme that advances the solution φ from $t = t_n$ to $t = t_n + \Delta t$ as

$$\varphi^{(n+1)} - \varphi^{(n)} = \Delta t \sum_{j=0}^{3} b_j (d\varphi/dt)^{(n-j)}. \tag{1.7}$$

By applying the Laplace transform with zero initial conditions to Eq. 1.7, it is easy to obtain the relation of numerical angular frequency and analytical angular frequency. Three of the four coefficients $b_j (j = 1, 2, 3)$ are chosen so that the scheme is formally third-order accurate. The remaining coefficient b_0 is used as an optimization parameter to minimize a weighted integral error between numerical angular frequency and analytical angular frequency.

Confined by the stability restrictions, the explicit temporal schemes is a poor choice for the viscous flow problem because the fine mesh spacing dictates a far too stringent time-step size constraint. This lead to the use of traditional implicit temporal schemes. Some implicit temporal schemes combined with compact high-order spatial schemes have been successfully applied in the complex unsteady subsonic flow problems [22, 23].

1.2.2.3 Computational Strategy

Different strategies can be used to solve an aeroacoustic problem. Roughly they can be classified as direct methods and hybrid methods.

Direct methods of the aerodynamically generated noise solve the flow and acous-

tic field simultaneously. Although there are successful cases of computational aeroacoustics which perform the direct calculation of the acoustic field by solving the unsteady compressible Navier-Stokes equations [24, 25], direct computation of the noise radiated by a subsonic three-dimensional (3D) flow remains difficult because of the large computing resources required. The cost of a direct numerical simulation (DNS) of a subsonic turbulent jet providing both local flow field and acoustic field is proportional to Re^3/M^4. In the same manner, the cost of a direct acoustic calculation using a large eddy simulation (LES) or detached eddy simulation (DES), assuming that the size of the resolved smallest eddies is given by the Taylor length scale, is proportional to Re^2/M^4 [26]. That's the reason why nowadays hybrid methods are widely used.

All hybrid methods subdivide the aeroacoustic problem into two parts, sound generation and sound propagation. This can be done due to the fundamental assumption that sound is generated by flow inhomogeneities, but the flow itself is not influenced by the acoustic field. If this assumption is valid the flow field can be simulated in a first step with standard CFD methods, only in those areas where sources of sound generation occur. The accuracy requirements for such types of CFD analysis are less high compared with the direct coupled approach since only the flow field inhomogeneities need to be resolved, rather than the superposed propagation of acoustic fluctuations. In a second step the acoustic field is calculated in the domain of interest based on the results of the CFD analysis.

In summary different hybrid computation strategies exist to solve decoupled aeroacoustic problems. Each of them has different advantages and disadvantages. Figure 1.5 shows the different hybrid approaches used for the noise prediction. Depending on the method to simulate the turbulence, the CFD methods for the calculation of the flow field can be subdivided into several categories:

1. **RANS+SNGR**

   In this approach, all of the stochastic unsteadiness are regarded as part of the turbulence and are averaged out. The steady turbulence flows are obtained by solving the RANS equations with an appropriate turbulence model. After that a method is used to reconstruct the time dependent turbulent flow field based on the averaged properties from the RANS calculation. The reconstruction is achieved by regarding the turbulence as a pseudo-stochastic phenomenon with many different length scales and time scales, and is called stochastic noise generation and radiation [27, 28, 29]. The numerical solution of the RANS equations is well established and relatively 'inexpensive', which

makes this approach attractive because of the time and memory efficiency.

2. **URANS**

   The time dependent turbulent flow field can be obtained by solving the URANS. In this approach, the turbulence is time averaged and the equations are closed by a turbulence model. Khorrami *et al.* [30] investigated the vortex shedding near the slat trailing edge of a high-lift wing model and the associated high frequency tonal noise using the computational fluid dynamics laboratory three-dimensional (CFL3D) code. The flow fields were simulated by solving the unsteady thin-layer Navier-Stokes equations with a finite volume formulation. The computed unsteady flow results were used as the input for the acoustic analysis tool based on the FW-H equations [31]. The analyzed results support the hypothesis that vortex shedding from the trailing edge of the slat is responsible for a loud, high-frequency noise observed in the experiment [30, 32].

3. **LES**, **DES** or **DNS**

   In a LES, the large turbulent scale eddies are solved while the small scale eddies are modeled with a subgrid-scale model. To circumvent the very fine near-wall mesh requirements of the LES method the DES approach was proposed by Spalart *et al.* [33] which reduces to RANS near solid boundaries and LES away form the wall. The most accurate approach to turbulence simulation is DNS in which all turbulent scales are to be described. Bogey *et al.* [26] performed the LES and DNS to get the flow generated noise, then the source term was used in the linearize Euler equation to obtain the acoustic field. The acoustic fields obtained using this hybrid method are in good agreement with the direct simulation result using DNS. Similar conclusion was found in Billson's work [34] in which the conservative form of the source term was applied.

1.2.3 Mechanisms of Slat Noise

For a typical wing of a commercial aircraft high-lift devices include slats ahead of the main element and flaps behind the main element (Figure 1.6). The geometry of the slat is determined by the condition that when retracted it must form the correct aerofoil geometry for the wing in cruising flight. Consequently, the slat has a highly curved under surface, referred to as the cove. When the slat is deflected

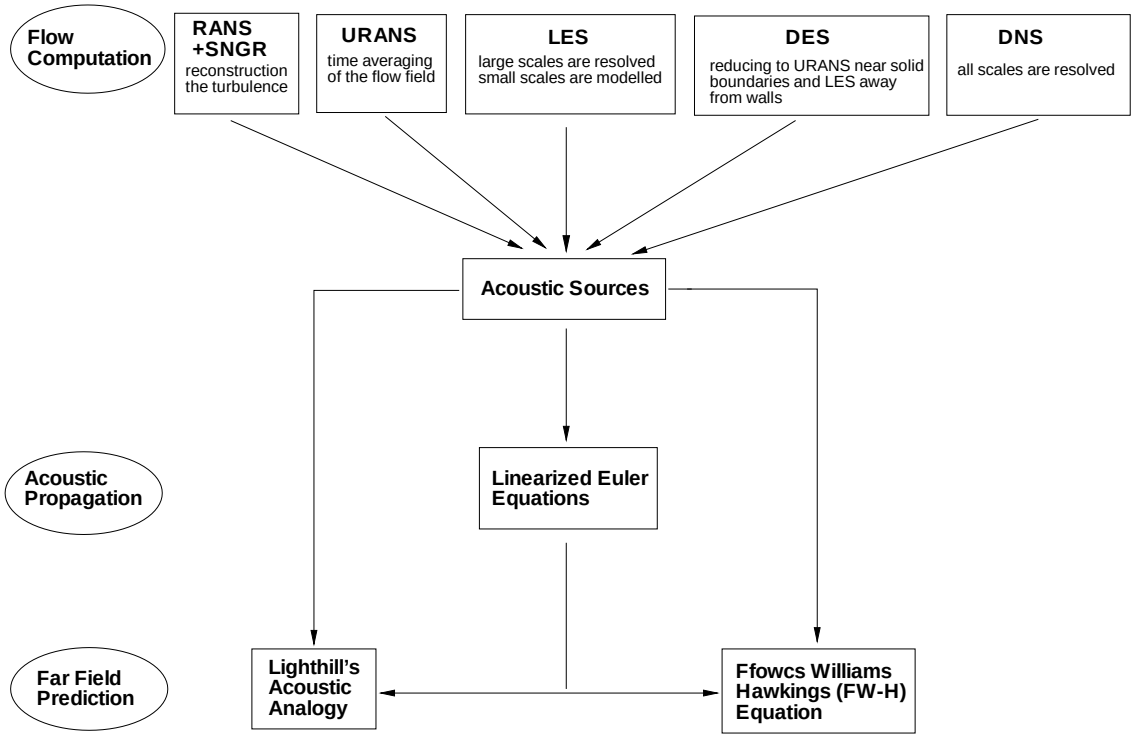

Figure 1.5: Different hybrid noise prediction approaches.

the flow in the slat cove region is separated [35]. Several flow phenomena are taking place due to the separated flow in the slat cove region and its interaction with the surrounding flow such as, low-speed recirculating flow, free shear layer, and ejections of large-scale structures merging with the slat wake. Other important phenomena can also exist, such as, the interaction of the slat wake with the wing boundary layer, referred to as the confluent boundary layer, and slat trailing edge vortex shedding (Figure 1.6). All of these aerodynamic fluctuation may cause the noise generation.

In general, the slat noise acoustic spectrum contains both high frequency tonal components and broadband components covering the lower and mid frequencies [4, 36]. For a commercial aircraft in flight, the broadband noise is more important since the A-weighted spectrum peaks at around 800Hz [37]. Recent experiments and numerical simulations have suggested that the high frequency tonal noise is caused by the vortex shedding from a region in the vicinity of the slat trailing edge [30, 31, 38] or it is a result of acoustic resonance [39, 40, 41] . The source of the broadband noise is less clear however. It has been shown to be associated with the unsteady flow in the slat cove region [42, 43, 44], but others have suggested that the actual noise source is located at the slat trailing edge, and that the source is

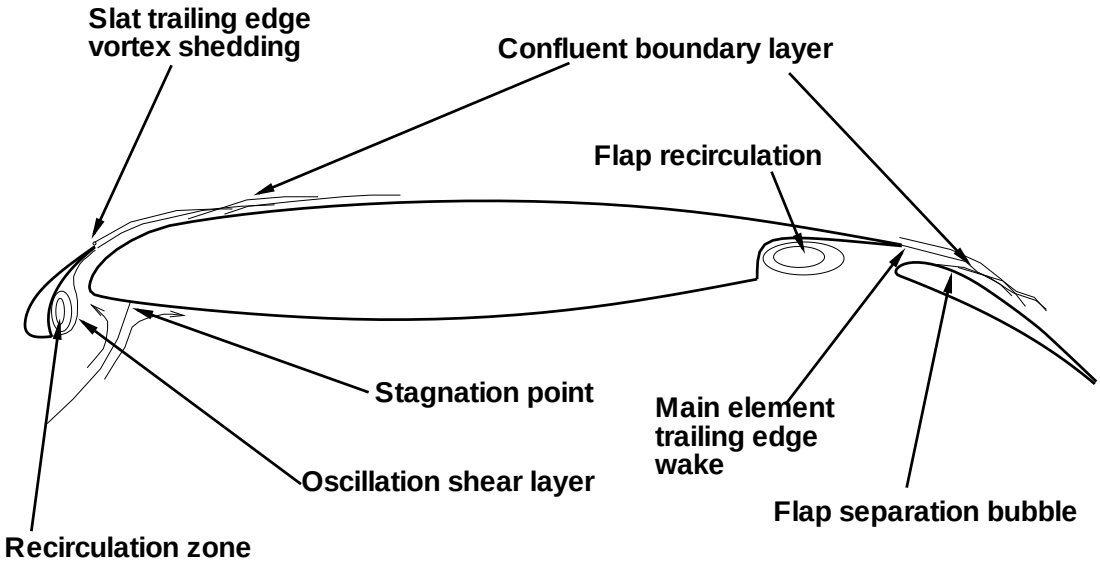

Figure 1.6: Schematic of typical high-lift system flow complexity.

due to the convection of the turbulence past that edge [37, 45].

Below is a summary on the previous slat noise investigation.

1.2.3.1 High-Frequency Tonal Noise

The presence of strong vortex shedding behind the blunt trailing edge of the slat is considered as one of the reasons for the generation of tonal noise.

Khorrami *et al.* [30] used URANS computations on the energy efficient transport (EET) high-lift configuration to identify and capture the associated aerodynamic noise sources. The simulation was performed at $M = 0.2$ and $Re = 7.2 \times 10^6$. A Fourier analysis of the pressure signal obtained from the URANS solution on the lower sharp corner at the slat trailing edge, and a nearby location, indicated a shedding frequency of approximately 45 kHz for a slat trailing edge thickness of 0.39 mm. The calculated results were compared with the experimental data and this shedding frequency was within the range of the measured high-frequency peak. The reduction in amplitude and the shift to a lower shedding frequency with decreasing Reynolds number were also consistent with the measured trends in the high-frequency peak from the slat acoustic spectra.

Singer *et al.* [31] performed an acoustic analysis based on the FW-H equation [11]

to compute the far-field acoustics from the URANS computation results of Khorrami *et al* [30]. The predicted radiated frequencies matched the computed shedding frequencies and the measured far-field acoustics. The computed directivity showed strong lobes upstream and downward toward the ground.

Agarwal and Morris [39] proposed another tonal sound noise generation mechanism. They conjectured that the observed high-frequency tone in the experiments was due to a whistling mechanism. The normal modes of the whistle are given by the transverse resonance frequencies of the gap between the slat and the main element. When the vortex shedding frequency, acting as an external source, matches any one of these modes resonance occurs, and a high amplitude tone is generated. Agarwal and Morris [39] showed that the whistling criterion is met for a slat deflection of 30 degrees.

1.2.3.2 Low Frequency Broadband Noise

Savory *et al.* [46] gave the first picture of the slat cove flow field by utilizing an airfoil model based on an A-300 series profile, with variable slat and flap geometry. A recirculation region in the slat cove, as well as acceleration of the flow through the cove region was shown when the slat was deflected at 25 degrees. Measurements of the mean velocity and turbulence intensity in and around the slat cove region provided data to improve numerical prediction models. This investigation was a first attempt at showing the complex flow around the slat. Further experimental investigations of the slat cove flow field by Alemdaroglu [47] enabled one to evaluate the effects of different gap and overhang settings on the size of the recirculation region and the influence on the pressure distributions.

Khorrami *et al.* [30] anticipated the slat free shear layer, along with the recirculation zone, to be an important source of flow unsteadiness and noise generation. In their numerical simulation [30] they found the self-excitation of the free shear layer but it was damped and did not last more than a few periods because of numerical dissipation. Therefore, they [48] introduced explicit forcing of the shear layer to excite and maintain the large-scale structures observed experimentally by Paschal *et al.* [43] and Takeda *et al.* [44]. Two-dimensional (2D) URANS computations were carried out in a fully-turbulent mode using the two-equation SST $\kappa - \omega$ turbulence model of Menter [49] on the EET model. Simulations were performed at an 8 degrees angle of attack with a slat deflection of 30 degrees. Vorticity contours obtained from the computations clearly displayed the spatial location of the free shear layer. The shear layer was a good amplifier of initial perturbations that resulted in a shear layer roll-up process and the formation of discrete vortices. The resulting acoustic

field had a broadband spectrum, similar to what was seen in the experimental data. Although amplitude was much less than what was measured, the spectrum shape in the mid-frequency range was similar. Khorrami *et al.* concluded that this similarity strongly suggested that growth of vorticity in the shear layer was largely responsible for radiated noise in the lower frequency range.

Khorrami *et al.* observed the rapid dissipation of the rolled-up vortices within a short spatial distance. Based on observations, they surmised that the cove flow field behaves in an unsteady quasi-laminar manner. Therefore, Khorrami *et al.* [50] try to circumvent the excessive diffusive effects of the turbulence model by switching off the turbulence model in a limited zone that enclosed the cove area. The same two-equation SST $\kappa - \omega$ turbulence model of Menter was used with the explained major alteration. 2D URANS simulations were performed for three angles of attack of 4, 6, and 8 degrees, to provide a direct comparison with the previous computations [48]. In addition, the simulations provided an understanding of the effects of angle of attack variation on the shear layer instability modes, the dynamics of the cove flow field, and the radiated acoustic field. In contrast to the fully turbulent simulations, the partially laminar simulation at an 8 degrees angle of attack showed extremely complex and highly nonlinear flow dynamics in the cove region. The shear layer was self-exciting and no external forcing was used. Vortices did escape through the slat gap and were severely deformed by the accelerating local flow. This behavior was in agreement with the particle image velocimetry (PIV) measurements of Paschal *et al.* [43] and Takeda *et al.* [44].

More recently, Deck [51] performed a zonal-detached-eddy simulation of the flow around a high-lift configuration and the results show good agreement of the computed and measured mean flows. The calculation captured the important unsteadiness in the slat cove such as rollup and formation of discrete vortices. In Ref. [52] a 3D simulation with the pseudo-laminar approach was performed and the computation was compared with the PIV measurements. The results indicate that the broadband band noise sources are driven by the significant turbulent fluctuations in the slat cove region.

1.2.4 Acoustic Liners

1.2.4.1 Introduction of Typical Acoustic Liners

Conventional acoustic liners are generally used on the inside surface of commercial aircraft jet engines for fan noise reduction. They are based on arrays of Helmholtz resonators. A Helmholtz resonator (Figure 1.7) has a short neck and then widens out

into a large volume chamber [53]. Resonance of a Helmoltz resonator is established when the mass of the plug of air in the neck oscillates against the large volume of air in the chamber. At resonance, small pressure perturbations give rise to large oscillating mass fluxes in the neck. These in turn induce large viscous losses, and narrow band sound absorption is achieved for frequencies close to resonance. In the absence of a mean flow, the absorption coefficient, defined as the proportion of incident energy absorbed, is a non-linear function of the acoustic pressure. High incident acoustic pressures are required before the absorption becomes significant. In the presence of a mean flow, the absorption is linear and the absorption coefficient is independent of the magnitude of the acoustic pressure. In this instance, absorption is obtained over a wider range of frequencies [54].

Figure 1.7: Helmholtz resonator [55].

Conventional acoustic liners are normally composed of a perforated plate and honeycomb core (Figure 1.8). The honeycomb core is composed of cells which, when bonded to the face sheet, create cavities behind the face sheet. The attachment of an impervious backing facing sheet to the honeycomb core seals the honeycomb, isolating each cavity from its neighbours. The main geometric parameters for single-layer liner configurations are the diameter of the holes of the perforate, the porosity of the perforate, the thickness of the perforate, and the depth of the cavities.

Tam and Kurbatskii [55] investigated the mechanisms by which the acoustic energy is dissipated in acoustic liners, using direct numerical simulation of the flow field around and inside a liner resonator under the excitation of plane acoustic waves. A 2D model without outside flow was considered for this investigation. Results gave a better understanding of the flowfield and the physics around the opening of a liner resonator when excited by incident acoustic waves. At low sound intensity, a strong oscillatory boundary layer, with a jet-like velocity profile around the opening of the liner was observed. Most of the dissipation was contributed by the shear gradients of the unsteady boundary layer flows. At high sound intensity, the shedding of microvortices from the mouth of the resonator was observed. These

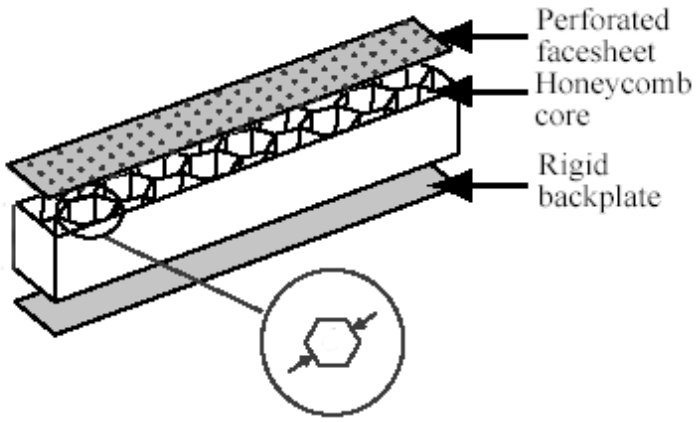

Figure 1.8: Single-layer acoustic liner [56].

microvortices carried with them a significant amount of kinetic energy that was eventually dissipated into heat. The shedding of microvortices is a very efficient energy dissipation mechanism.

Typical single-layer acoustic liners are characterized by a single complex quantity Z, called the acoustic impedance. In frequency domain, it is mathematically defined as

$$Z(\omega) = \frac{\hat{p'}(\omega)}{\hat{u'_n}(\omega)} = R + iX \tag{1.8}$$

where $\hat{p'}(\omega)$ and $\hat{u'_n}(\omega)$ are harmonic components with time factor $e^{i\omega t}$ of the perturbed pressure $p'(t)$ and its induced normal velocity component $u'_n(t)$ into a porous surface S. Here, angular frequency ω is normalized by sound speed c_0 and characteristic length L; $\hat{p'}$ by $\rho_0 c_0^2$ with mean air density ρ_0, $\hat{u'_n}$ by c_0, and Z by $\rho_0 c_0$. In general, the pressure and velocity are not in phase, thus the impedance is a complex quantity with a real and imaginary parts. The real part R is referred to as the acoustic resistance and the imaginary part X is referred to as the acoustic reactance. These quantities are generally frequency dependent. For a given frequency, the acoustic resistance is only a function of the perforate plate configuration. The acoustic reactance is a function of the perforate plate configuration and the cavity depth behind the perforate plate [56]. The acoustic resistance and reactance are usually measured empirically. Although, some semi-empirical formulas are available for their estimates, provided the construction of the panels is sufficiently simple.

Single-layer liners are only one class of a family of passive acoustic resonant liners. More advanced designs with increased degrees-of-freedom such as double layers, triple layers, and parallel elements, exist for achieving increased bandwidth

attenuation. Innovative liner concepts may involve either self-adjusting liners based on microeletromechanical systems technology, or a conventional passive liner with in-situ control of an impedance regulating parameter such as bias flow across the liner perforate [57]. Active control of liner impedance has been investigated by varying the perforate orifice geometry [58], using a bias flow concept that uses a steady bias flow (blowing or suction) through the liner, or by increasing the temperature of the liner to modify its acoustic properties [59, 60]. The bias flow concept opens up the possibility of controlling boundary layer flow simultaneously with noise control.

1.2.4.2 Time Domain Impedance Boundary Condition

Traditionally, the acoustic impedance condition has been limited to frequency domain methods, primarily because of the frequency dependent characteristics of lining materials. Time domain applications of such materials are difficult to simulate because of the computation of expensive convolutions. However, a suitable equivalent of the impedance boundary condition has to be developed in the time domain in order to apply CAA techniques for computing sound propagation from the unsteady flow field of the leading edge slat. Moreover, a time domain method is most suitable for the analysis of broadband frequency problems. For broadband noise problems, frequency domain methods are computationally intensive, while time domain methods have the ability to handle multi-frequency sources in one single simulation.

For the frequency domain relation Eq. 1.8, it has the equivalent time convolution of

$$p'(t) = \int_{-\infty}^{\infty} \bar{Z}(\tau) u_n'(t-\tau) d\tau, \tag{1.9}$$

where $\bar{Z}$ is the inverse Fourier transform of $Z(\omega)$. By Cauchy's theorem, unless all poles λ_k of $Z(\omega)$ lie in the upper complex ω-plane, i.e. $\mathrm{Img}(\lambda_k) > 0$, the current value of $p'(t)$ would involve future values of $u_n'(t)$ in $\int_{-\infty}^{0} \bar{Z}(\tau) u_n'(t-\tau) d\tau$, which is unphysical for the violation of causality. In order to evaluate the convolution practically, a time domain impedance boundary must be causality, stable and confine the infinite convolution to a finite time history.

Several approaches have been made toward the development of a TDIBC. Tam and Auriault developed their time domain single-frequency and broadband impedance boundary conditions for the three-parameter impedance model of the Helmholtz resonator type by implicitly using the derivative properties of the Fourier transform [61]. For the single frequency case, they propose a boundary condition

$$X < 0, \qquad \frac{\partial p'}{\partial t} = R \frac{\partial u_n'}{\partial t} + X \omega u_n', \tag{1.10}$$

$$X > 0, \qquad p' = Ru'_n - \frac{X}{\omega}\frac{\partial u'_n}{\partial t}. \tag{1.11}$$

For the broadband case, they propose a three-parameter model of impedance:

$$Z = R_0 + i[(X_{-1}/\omega) + X_1\omega] \tag{1.12}$$

where R_0 is the modeled acoustic resistance, X_{-1} is the modeled acoustic stiffness and X_1 is the modeled acoustic mass.

Figure 1.9 shows values of measured R and X for a 6.7% perforate acoustic treatment panel and the fitted curves by Tam and Auriault's model. Using this model, the corresponding time domain impedance boundary is

$$\frac{\partial p'}{\partial t} = R_0\frac{\partial u'_n}{\partial t} + X_{-1}u'_n - X_1\frac{\partial^2 u'_n}{\partial t^2}. \tag{1.13}$$

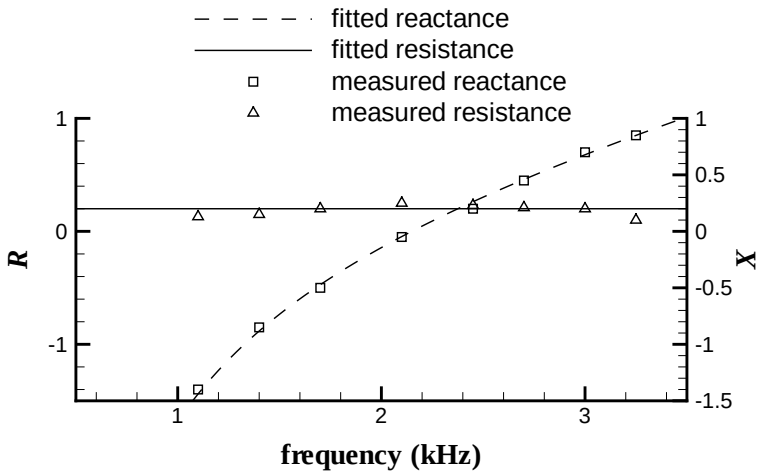

Figure 1.9: Measured and fitted frequency-dependent resistance R and reactance X of a 6.7% perforate treatment panel.

The stability analysis on the ω-plane shows that the single-frequency and broadband TDIBC is stable. They demonstrated this by the reflection of a banded pulse in one dimension. Their schemes were applied and verified on multidimensional acoustic problems by Zheng and Zhuang [62, 63].

Özyörük borrowed the idea from the computational electromagnetics community and proposed a time domain surface acoustic impedance condition based on the $\check{z}$-transform [64, 65]. The Eq. 1.9 can be considered as an acoustic system. The acoustic normal velocity is input; the acoustic pressure is output and the impedance terms that appears in the convolution integral is the response to the input. The

Özyörük's idea is to represent the output as a linear combination of the previous inputs and outputs. By this approach one can find an equivalent finite series to a convolution summation. The $\check{z}$-transform is a useful tool to accomplish this task. If the impedance Z can be expressed as a fraction of two finite polynomials in the complex variables $\check{z}$, using the shifting property of the $\check{z}$-transform, one could obtain a simple relation between the acoustic velocity and pressure. For example, let $Z(\check{z})$ be given by

$$Z(\check{z}) = \frac{a_0 + a_1\check{z}^{-1}}{1 - b_1\check{z}^{-1} - b_2\check{z}^{-2}} \tag{1.14}$$

where as and bs are the model coefficients. Then application of the impedance relation in $\check{z}$-plane yields

$$(1 - b_1\check{z}^{-1} - b_2\check{z}^{-2})\check{p'}(\check{z}) = -(a_0 + a_1\check{z}^{-1})\check{u'_n}(z) \tag{1.15}$$

where $\check{p'}$ and $\check{u'_n}$ are the $\check{z}$-transform of the acoustic pressure and normal velocity at the impedance boundary respectively. Then after the inverse $\check{z}$-transform using the shifting property, one obtain

$$p'^n = b_1 p'^{n-1} + b_2 p'^{n-2} - (a_0 u'^n_n + a_1 u'^{n-1}_n) \tag{1.16}$$

where the superscript n indicates the time level. In practical computation, the parameters of resistance and reactance of the impedance are found using a nonlinear least square fit algorithm to fit the measured value. The method was demonstrated on the reflection of a Gaussian pulse in one and two dimensions and on the absorption of waves in a flow duct with a partially lined impedance wall [66, 67].

More recently, Fung and Ju applied the inverse Fourier transforms to the reflection coefficient (Υ) instead of the corresponding impedance, resulting in a stable time domain impedance boundary condition [68, 69]. In their approach, they define the $u'^+(x-t)$ and $u'^-(x+t)$ as the uncoupled forward and backward propagating simple waves through the linear relation

$$\begin{bmatrix} u'^+ \\ u'^- \end{bmatrix} = \begin{bmatrix} 1 & 1 \\ 1 & -1 \end{bmatrix} \begin{bmatrix} u' \\ p' \end{bmatrix}. \tag{1.17}$$

In frequency domain the reflective wave at the right boundary is related to the incident wave by

$$\hat{u}'^- = \hat{\Upsilon}(\omega)\hat{u}'^+ \tag{1.18}$$

where $\hat{\Upsilon}(\omega) = \frac{1-Z}{1+Z}$ is the reflection coefficient in frequency domain. The complex

function $\hat{\Upsilon}$ is indeed a direct measure of the magnitude of the reflection and its relative phase with the incident wave. This bilinear mapping maps the right half-plane $\mathrm{Re}(Z) \geq 0$ analytically into the interior of the unit circle $|\hat{\Upsilon}| \leq 1$ ensuring that the reflection is not amplified.

The Eq. 1.18 is equivalent to the convolution process of

$$u'^{-}(t) = \int_{-\infty}^{\infty} \Upsilon(t-\tau) u'^{+}(\tau) d\tau. \tag{1.19}$$

The evaluation of the above convolution integral is computationally expensive and consequently impractical for CAA problems. However, the behaviors of $\Upsilon(t)$ depend on $Z(\omega)$. A suitable form of Z should yield a desirable numerical implementation of Eq. 1.19. Tam and Auriault's model [61] was adopted. Using this model, $\hat{\Upsilon}$ has the simple poles and if $X_1 > 0$ and $X_{-1} < 0$, both of the poles lie in the upper complex plane. This implies that the $\Upsilon(t)$ is causal. Figure 1.10 plots $\Upsilon(t) + \delta(t)$ for $0 < t < 40$ using the impedance value of Figure 1.9, where $\delta()$ is Dirac delta function and $\Upsilon(t)+\delta(t)$ is defined as reflection kernel. Beyond the range of $0 < t < 40$ the reflection kernel is either zero when $t < 0$, or insignificantly small ($|\Upsilon(t) + \delta(t)| < 0.002$) when $t \geq 40$. This implies the practicality of enforcing a full spectrum of wall reflectivity within a finite time history. This implies that the expensive convolution can be replaced by an integral sum. Using the recursive formula given in [69], the time domain impedance boundary condition can be implemented efficiently.

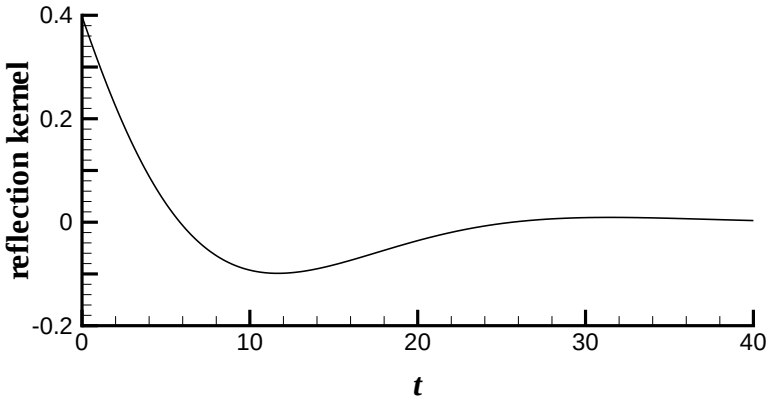

Figure 1.10: Time history of reflection kernel.

Fung *et al.* benchmarked their methods on the reflection of impulses in one dimension and on an analytically constructed Gaussian pulse reflection in two dimen-

sions. Their methods have since been extended to duct acoustics in three dimensions by Ju and Fung [70], acoustics in partially lined flow ducts in two dimensions [71], and reflection of acoustic sources by an impedance plane for outdoor acoustics [72].

TDIBC developed by Fung *et al.* is a numerically stable, accurate, and easily implementable schemes for waves and seems to be the most suitable technique to numerically investigate the effects of liners on the acoustic field generated by the slat flow. So this method is adopted in this work.

1.3 Aim of Research

In the literature review of the preceding section the issues central to this research have been outlined. The leading edge slat noise is a dominant component of the total airframe noise during approach and passive control using acoustic liner is a potential method to mitigate the noise. As the directivity of the slat noise source and its radiation characteristics into the slat gap is likely to be a complex function of frequency, flow and slat geometry. This creates problems for experimentation at model scale, and a good reason for developing some understanding through the use of numerical models. The specific aims of the research are to:

1. develop an efficient and accurate numerical method to study the generation and far field radiation of the slat noise of a high-lift wing.

2. implement a stable and efficient time domain impedance boundary condition to simulate the reflection characteristics of acoustic liners.

3. explore the concept of slat noise attenuation using acoustic liners by numerical simulation.

1.4 Thesis Structure

The rest of the thesis is organized as follows:

In Chapter 2, the numerical models used in the research are described. Firstly, the description of the CAA code SotonCAA is given and then the acoustic code SotonLEE is outlined. Finally the radiation model is presented.

After that, in Chapter 3 the numerical simulations of 2D slat trailing edge tonal noise are presented. The computational work of this chapter is divided into three parts: (1) an URANS simulation using high-order spatial and temporal schemes is conducted for wing with high-lift devices deployed; the computed flow shows

the presence of vortex shedding and acoustic sources behind the slat trailing edge; (2) an exercise is conducted on a range of liner impedance values by solving the linearized Euler equations with a representation of the computed acoustic sources at the trailing edge of the slat; (3) URANS computations with liner treatment are conducted for the case of a liner on the slat cove and the case of a combination of liner on the slat cove surface and liner on the main element respectively.

In Chapter 4 the 2D computational works for low frequency broadband slat noise are given. Computational results for acoustic field predicted by the pseudo-laminar zonal method and the SNGR method are presented and compared; the SNGR method is then used to study the broadband noise attenuation effect of the acoustic liner treatment on the slat and the main element.

In Chapter 5 the 3D computational works for low frequency broadband slat noise are presented. The broadband slat noise generation of a modified high-lift configuration (with flap retracted) are simulated using LES. The LES calculated noises sources are then used to drive the APE to investigate the broadband noise attenuation effect of the acoustic liner treatment on the slat and the main element.

Finally in Chapter 6 the main results obtained are summarized and future works are proposed.

Chapter 2

Numerical Models

The purpose of this second chapter is to describe the numerical models used in the research. Firstly, the description of the CAA code SotonCAA is given and then the acoustic code SotonLEE is outlined. Finally the radiation model is presented.

2.1 Introduction

The aim of the computational work is to investigate the noise produced by the slat flow and to explore the concept of attenuating the noise by acoustic liner. Three numerical tools are used for this purpose: a high-order accurate Navier-Stokes (N-S) flow solver SotonCAA, a high-order accurate linearized Euler acoustic solver SotonLEE and an integral radiation model based on the Ffowcs Williams and Hawkings equation. The CAA solver is used to model the time-dependent flow dynamics in the source region. The acoustic solver is used to explore the effect of different liners on noise attenuation. The radiation model is used to obtain the far field acoustic signal using the time-dependent flow data as input and gives the direct comparison for the hard wall wing and lined wing. Details of the three models are given in the following sections of this chapter.

2.2 Computational Aeroacoustic Solver

The CAA code SotonCAA is used for the high-left wing flow simulations. SotonCAA is a multi-block Navier-Stokes flow solver for structured grids. It is based on high-order accurate compact schemes and is at most sixth-order accurate in space and fourth-order accurate in time. The code possesses excellent wave propagation characteristics, with marginal dispersion, dissipation and anisotropy errors. By solv-

ing the governing equations in generalized coordinates in a multi-block fashion, the code is capable of accommodating complex geometries. The multi-block structure of the code also provides a convenient basis for the parallelization of the code. Further details of these features are given in the following sections.

2.2.1 Governing Equations

SotonCAA[1] solves the compressible three-dimensional Navier-Stokes equations. In the absence of body forces and external heat addition these equations may be written as follows

$$\frac{\partial \hat{\mathbf{Q}}}{\partial t} + \frac{\partial \hat{\mathbf{F}}}{\partial \xi} + \frac{\partial \hat{\mathbf{G}}}{\partial \eta} + \frac{\partial \hat{\mathbf{H}}}{\partial \zeta} = \frac{M_\infty}{Re_L}\left[\frac{\partial \hat{\mathbf{F}}_v}{\partial \xi} + \frac{\partial \hat{\mathbf{G}}_v}{\partial \eta} + \frac{\partial \hat{\mathbf{H}}_v}{\partial \zeta}\right] \tag{2.1}$$

where t is time, x, y, z are the Cartesian coordinates, $\hat{\mathbf{Q}} = (1/J)\left[\rho, \rho u, \rho v, \rho w, \rho E\right]^T$ denotes the solution vector and $J = |\partial(\xi, \eta, \varsigma)/\partial(x, y, z)|$ is the coordinates transformation Jacobian. The inviscid $\hat{\mathbf{F}}, \hat{\mathbf{G}}, \hat{\mathbf{H}}$ and viscous fluxes $\hat{\mathbf{F}}_v, \hat{\mathbf{G}}_v, \hat{\mathbf{H}}_v$ are

$$\hat{\mathbf{F}} = \frac{1}{J}\begin{bmatrix} \rho U \\ \rho U u + \xi_x p \\ \rho U v + \xi_y p \\ \rho U w + \xi_z p \\ (\rho E + p) U \end{bmatrix}, \hat{\mathbf{F}}_v = \frac{1}{J}\begin{bmatrix} 0 \\ \xi_x \sigma_{xx} + \xi_y \sigma_{xy} + \xi_z \sigma_{xz} \\ \xi_x \sigma_{xy} + \xi_y \sigma_{yy} + \xi_z \sigma_{yz} \\ \xi_x \sigma_{xz} + \xi_y \sigma_{yz} + \xi_z \sigma_{zz} \\ \xi_x b_x + \xi_y b_y + \xi_z b_z \end{bmatrix}, \tag{2.2}$$

$$\hat{\mathbf{G}} = \frac{1}{J}\begin{bmatrix} \rho V \\ \rho V u + \eta_x p \\ \rho V v + \eta_y p \\ \rho V w + \eta_z p \\ (\rho E + p) V \end{bmatrix}, \hat{\mathbf{G}}_v = \frac{1}{J}\begin{bmatrix} 0 \\ \eta_x \sigma_{xx} + \eta_y \sigma_{xy} + \eta_z \sigma_{xz} \\ \eta_x \sigma_{xy} + \eta_y \sigma_{yy} + \eta_z \sigma_{yz} \\ \eta_x \sigma_{xz} + \eta_y \sigma_{yz} + \eta_z \sigma_{zz} \\ \eta_x b_x + \eta_y b_y + \eta_z b_z \end{bmatrix}, \tag{2.3}$$

[1] In presenting the scheme, the notation u, v, w and x, y, z have been used to represent the Cartesian velocity components and Cartesian coordinates, respectively. However, for compactness, tensor notation is employed to denote these quantities in the expressions for the shear stress tensor and heat flux vector

$$\hat{\mathbf{H}} = \frac{1}{J}\begin{bmatrix} \rho W \\ \rho W u + \zeta_x p \\ \rho W v + \zeta_y p \\ \rho W w + \zeta_z p \\ (\rho E + p) W \end{bmatrix}, \hat{\mathbf{H}}_v = \frac{1}{J}\begin{bmatrix} 0 \\ \zeta_x \sigma_{xx} + \zeta_y \sigma_{xy} + \zeta_z \sigma_{xz} \\ \zeta_x \sigma_{xy} + \zeta_y \sigma_{yy} + \zeta_z \sigma_{yz} \\ \zeta_x \sigma_{xz} + \zeta_y \sigma_{yz} + \zeta_z \sigma_{zz} \\ \zeta_x b_x + \zeta_y b_y + \zeta_z b_z \end{bmatrix}, \tag{2.4}$$

where ρ, u, v, w, p and E are the fluid density, Cartesian velocity components, static pressure and specific total energy, respectively. The specific total energy is defined as

$$E = e + \frac{1}{2}(u^2 + v^2 + w^2) \tag{2.5}$$

where e is the specific internal energy density. The pressure is related to the other thermodynamic variables by the equation of state for an ideal gas

$$p = (\gamma - 1)\rho + \left(E - \frac{1}{2}(u^2 + v^2 + w^2)\right) \tag{2.6}$$

where $\gamma = c_p/c_v$ is the ratio of specific heat coefficients under constant pressure and constant volume. The terms U, V and W in the inviscid fluxes are the contravariant velocities. These are defined as follows

$$\begin{aligned} U &= \xi_x u + \xi_y v + \xi_z w \\ V &= \eta_x u + \eta_y v + \eta_z w \\ W &= \zeta_x u + \zeta_y v + \zeta_z w \end{aligned} \quad . \tag{2.7}$$

The terms σ_{ij} are the viscous stresses. These are related to the Cartesian velocity components by the equation

$$\sigma_{ij} = \mu \left[\left(\frac{\partial u_j}{\partial x_i} + \frac{\partial u_i}{\partial x_j} \right) - \frac{2}{3} \frac{\partial u_k}{\partial x_k} \delta_{ij} \right] \tag{2.8}$$

where μ is the molecular viscosity and δ_{ij} is the Kronecker delta. The terms b_j are defined as follows

$$b_j = u_i \sigma_{ij} + \frac{1}{(\gamma - 1)} \frac{\mu}{Pr} \frac{\partial c^2}{\partial x_j} \tag{2.9}$$

where c is the local sound speed.

The governing equations are non-dimensionalized with a reference length L^*, freestream values of density ρ^*_∞, sound speed c^*_∞ and viscosity μ^*_∞. The superscript notation $()^*$ denotes a reference quantity. On this basis the characteristic parameters

of Mach number M_∞, Reynolds number Re_L and Prandtl number Pr have the following definitions

$$M_\infty = \frac{|\mathbf{u}^*_\infty|}{c^*_\infty}, \qquad Re_L = \frac{\rho^*_\infty |\mathbf{u}^*_\infty| L^*}{\mu^*_\infty}, \qquad Pr = \frac{c^*_p \mu^*_\infty}{k^*_T} \tag{2.10}$$

where $\mathbf{u}^*_\infty$ is the freestream velocity vector, c^*_p is the specific heat coefficient at constant pressure and k^*_T is the thermal conductivity coefficient.

2.2.2 Spatial Discretization

A finite-difference approach is employed to discretize the governing equation. This choice is motivated by the relative ease of formal extension to higher-order accuracy, low operation count and general flexibility. For any scalar quantity φ, the first spatial derivative $(\partial\varphi/\partial\xi)_i$ at any point i is computed in the transformed plane by solving the following system of equations

$$\frac{1}{2}D^F_i = \frac{1}{2\beta_F \triangle\xi}\left[b_F(\varphi_{i+1}-\varphi_i) + d_F(\varphi_{i-1}-\varphi_i) + e_F(\varphi_{i-2}-\varphi_i\right] - \frac{\alpha_F}{2\beta_F} D^F_{i+1}, \tag{2.11}$$

$$\frac{1}{2}D^B_i = \frac{1}{2\beta_F \triangle\xi}\left[b_F(\varphi_i-\varphi_{i-1}) + d_F(\varphi_i-\varphi_{i+1}) + e_F(\varphi_i-\varphi_{i+2}\right] - \frac{\gamma_B}{2\beta_B} D^B_{i-1}, \tag{2.12}$$

$$D_i = \frac{1}{2}(D^F_i + D^B_i) \tag{2.13}$$

where D_i, the desired approximation of the spatial derivative, is obtained by adding the forward D^F_i and backward D^B_i estimates of the spatial derivative. The coefficients b_F, d_F, e_F etc. determine the spatial properties of the algorithm. The system of equations encompass a family of schemes ranging in accuracy from the standard three-point, second-order accurate explicit method to a compact seven-point, eight-order algorithm. In this work the fourth-order compact scheme of Ashcroft and Zhang [20] and sixth-order compact scheme of Hixon [19] are employed to evaluate the spatial derivatives.

The derivatives of the inviscid fluxes are obtained by first forming the fluxes at the nodes and subsequently differentiating each component using the above formulae. For the computation of the viscous terms, the primitive variables u, v, w and c are first differentiated to form the components of the stress tensor and the heat flux vector at each node. The viscous flux derivatives are then computed by a second application of the same scheme.

2.2.3 Filtering Scheme

The prefactored compact schemes described in the previous section are centered schemes, and therefore contain no inherent dissipation. Whilst this is desirable for wave propagation it does leaves such schemes susceptible to failure from the unchecked growth of high-frequency modes. Such modes can originate from mesh non-uniformity, boundary conditions, nonlinear flow feature, or poorly specified initial conditions. To overcome these difficulties and extend the flow solver to practical problems, while retaining the improved accuracy of the spatial compact discretization, the high-order implicit filtering technique due to Visbal and Gaitonde [73] has been incorporated.

If a component of the solution vector is denoted by φ, filtered values $\hat{\varphi}$ are obtained by solving the tridiagonal system

$$\alpha_f \hat{\varphi}_{i-1} + \hat{\varphi}_i + \alpha_f \hat{\varphi}_{i+1} = \sum_{n=0}^{N} \frac{a_n}{2} (\varphi_{i+n} + \varphi_{i-n}) \tag{2.14}$$

where the coefficient $\alpha_f, \alpha_0, \alpha_1, \cdots, \alpha_N$ determine the order and spectral response of the filter. With a proper choice of these coefficients, Equation 2.14 provides a $2N$th-order formula on a $2N+1$ point stencil. In Ref. [73] Visbal and Gainonde show, using a combination of Taylor- and Fourier-series analyses, that the $N+1$ coefficients $\alpha_0, \alpha_1, \cdots, \alpha_N$ can be expressed solely in terms of α_f. The adjustable parameter $\alpha_f \in (-0.5, 0.5]$ then determines the dissipative characteristics of the filter for a given degree of accuracy. For the work presented the eighth-order filter variant has been used, with $\alpha_f = 0.495$. This choice ensures the spectral characteristics of the filter closely match those of the spatial compact discretization, preserving accuracy.

The eighth-order formula requires a nine point stencil, it is therefore not suitable for use at and near boundary points. In these regions, the order of accuracy of the filter is reduced as the boundary is approached to the level for which a centered scheme is available. Values along the boundary points are left unfiltered. The filter is applied sequentially in each coordinate direction to the conserved variable once every time step.

2.2.4 Temporal Integration

2.2.4.1 Explicit Runge-Kutta Scheme

The explicit low-storage Runge-Kutta scheme due to Hu, *et al.* [21] is used to advance the solution in time. This is an optimized two-step alternating scheme, in which different coefficients are employed in the alternating steps. The scheme uses four

stages in the first time step and six stages in the second step of the cycle. If the semi-discretized governing equations are written

$$\begin{aligned}\frac{d\hat{\mathbf{Q}}}{dt} &= -\left(D_\xi\hat{\mathbf{F}} + D_\eta\hat{\mathbf{G}} + D_\varsigma\hat{\mathbf{H}}\right) + \frac{M_\infty}{Re_L}\left(D_\xi\hat{\mathbf{F}}_v + D_\eta\hat{\mathbf{G}}_v + D_\varsigma\hat{\mathbf{H}}_v\right) \\ &= \mathbf{R}(\hat{\mathbf{Q}}) \end{aligned} \tag{2.15}$$

where D_ξ, D_η and D_ς denote the spatial derivative operators, each step in the cycle may be written

$$\hat{\mathbf{Q}}^{n+1} = \hat{\mathbf{Q}}^n + \sum_{i=1}^{N} s_i\mathbf{K}_i \tag{2.16}$$

where

$$\mathbf{K}_i = \triangle t\mathbf{R}(\hat{\mathbf{Q}}^n + \sum_{j=1}^{i-1} e_{ij}\mathbf{K}_i) \qquad i = 1, 2, \ldots, N. \tag{2.17}$$

Here N denotes the number of stages in each step, and s_i and e_{ij} are the coefficients of the particular step. The superscript n indicates time level. Integration from time level n to level $n+2$, is accomplished by first using the four-stages schemes to integrate from time level n to $n+1$, and then six-stage scheme to integrate from time level $n+1$ to $n+2$. Two-step schemes are favored over single-step schemes as they permit a greater degree of optimization for wave propagation. In this way the dissipation and dispersion errors of the alternating two-step schemes are reduced below those attainable through optimization of either of the individual single steps. The optimization procedure itself extends the accuracy bounds of the alternating two-step scheme at the expense of the stability bound. The resulted stability condition for the two-step scheme is 2.52.

To lower computational overheads the two-step alternating scheme is implemented in a low storage format. In low storage format, each of the steps in the alternating scheme is evaluated by computing

$$\mathbf{K}_i = \triangle t\mathbf{R}(\hat{\mathbf{Q}}^n + \bar{e_i}\mathbf{K}_{i-1}) \tag{2.18}$$

for $i = 1, 2, \ldots, N$ (with $\bar{e_1} = 0$), and then evaluating

$$\hat{\mathbf{Q}}^{n+1} = \hat{\mathbf{Q}}^n + \mathbf{K}_p. \tag{2.19}$$

This implementation requires three levels of date storage, as opposed to four levels for the classical fourth-order Runge-Kutta scheme.

2.2.4.2 Implicit Lower-Upper Factorization Scheme

To overcome the CFL limit of explicit schemes, a temporal implicit lower-upper approximate factorization algorithm employing Newton-like subiterations is developed to efficiently solve the complex flow generated noise problem.

To achieve the second order accuracy, a pseudo-time τ is introduce to the Equation 2.1 and the original governing equations can be written as:

$$\frac{\partial \hat{\mathbf{Q}}}{\partial \tau} + \frac{\partial \hat{\mathbf{Q}}}{\partial t} + \frac{\partial \hat{\mathbf{F}}}{\partial \xi} + \frac{\partial \hat{\mathbf{G}}}{\partial \eta} + \frac{\partial \hat{\mathbf{H}}}{\partial \zeta} = \frac{M_\infty}{Re_L}[\frac{\partial \hat{\mathbf{F}}_v}{\partial \xi} + \frac{\partial \hat{\mathbf{G}}_v}{\partial \eta} + \frac{\partial \hat{\mathbf{H}}_v}{\partial \zeta}]. \tag{2.20}$$

Apply the lower-upper approximate factorization method [74, 75, 76] and a Newton-like subiteration to the Equation 2.20, it may be represented notationally as follow:

$$\begin{aligned}(\mathbf{L}+\mathbf{D})\mathbf{D}^{-1}(\mathbf{D}+\mathbf{U})\Delta\hat{\mathbf{Q}}^m = \quad & -\frac{3\hat{\mathbf{Q}}^m - 4\hat{\mathbf{Q}}^n + \hat{\mathbf{Q}}^{n-1}}{2} \\ & -\Delta t D_{\xi 6}(\hat{\mathbf{F}}^m - \frac{M_\infty}{Re_L}\hat{\mathbf{F}}_v^m) \\ & -\Delta t D_{\eta 6}(\hat{\mathbf{G}}^m - \frac{M_\infty}{Re_L}\hat{\mathbf{G}}_v^m) \\ & -\Delta t D_{\zeta 6}(\hat{\mathbf{H}}^m - \frac{M_\infty}{Re_L}\hat{\mathbf{H}}_v^m).\end{aligned} \tag{2.21}$$

To obtain this formula, a first order backward difference formula is used to discretize the pseudo-time derivative and a second order backward difference formula is used to discretize the physical time derivative. The implicit segment of the algorithm incorporates a second order special difference and the explicit segment of the algorithm is evaluated using the 6th order compact scheme [19]. The $D_{\xi 6}$, $D_{\eta 6}$ and $D_{\zeta 6}$ represent the 6th order difference in ξ, η and ζ direction respectively. To achieve second order temporal accuracy, subiterations are used to reduce the error due to factorization, linearization and explicit implement of boundary condition. In Equation 2.21, $\hat{\mathbf{Q}}^{m+1}$ is the m+1 subiteration to approximate $\hat{\mathbf{Q}}$ at n+1 time level and $\Delta\hat{\mathbf{Q}} = \hat{\mathbf{Q}}^{m+1} - \hat{\mathbf{Q}}^m$. At time level n, the solution is advanced from m=1 and $\hat{\mathbf{Q}}^m = \hat{\mathbf{Q}}^n$. Three to five subiterations per time step is suitable for flow calculation which was shown in Ref. [77, 78] and validated in Appendix D.

In Equation 2.21,

$$\begin{aligned}\mathbf{L} &= -\Delta t(\hat{\mathbf{A}}^+_{i-1,j,k} + \hat{\mathbf{B}}^+_{i,j-1,k} + \hat{\mathbf{C}}^+_{i,j,k-1}), \\ \mathbf{D} &= [3/2 + \Delta t(r_{\hat{\mathbf{A}}} + r_{\hat{\mathbf{B}}} + r_{\hat{\mathbf{C}}})]\mathbf{I},\end{aligned} \tag{2.22}$$

$$\mathbf{U} = \Delta t(\hat{\mathbf{A}}^{-}_{i+1,j,k} + \hat{\mathbf{B}}^{-}_{i,j+1,k} + \hat{\mathbf{C}}^{-}_{i,j,k+1})$$

where

$$\begin{aligned}\hat{\mathbf{A}}^{+} = \frac{\hat{\mathbf{A}} + r_{\hat{\mathbf{A}}}\mathbf{I}}{2}, \hat{\mathbf{B}}^{+} = \frac{\hat{\mathbf{B}} + r_{\hat{\mathbf{B}}}\mathbf{I}}{2}, \hat{\mathbf{C}}^{+} = \frac{\hat{\mathbf{C}} + r_{\hat{\mathbf{C}}}\mathbf{I}}{2}, \\ \hat{\mathbf{A}}^{-} = \frac{\hat{\mathbf{A}} - r_{\hat{\mathbf{A}}}\mathbf{I}}{2}, \hat{\mathbf{B}}^{-} = \frac{\hat{\mathbf{B}} - r_{\hat{\mathbf{B}}}\mathbf{I}}{2}, \hat{\mathbf{C}}^{-} = \frac{\hat{\mathbf{C}} - r_{\hat{\mathbf{C}}}\mathbf{I}}{2}\end{aligned} \tag{2.23}$$

and the $r_{\hat{\mathbf{A}}} = \max(|\lambda_{\hat{\mathbf{A}}}|)$, $r_{\hat{\mathbf{B}}} = \max(|\lambda_{\hat{\mathbf{B}}}|)$ and $r_{\hat{\mathbf{C}}} = \max(|\lambda_{\hat{\mathbf{C}}}|)$ where $\lambda_{\hat{\mathbf{A}}}$, $\lambda_{\hat{\mathbf{B}}}$ and $\lambda_{\hat{\mathbf{C}}}$ are the eigenvalues of flux Jacobian matrixes $\hat{\mathbf{A}}$, $\hat{\mathbf{B}}$ and $\hat{\mathbf{C}}$ respectively. The flux Jacobian matrixes are calculated from their Cartesian counterparts by:

$$\begin{aligned}\hat{\mathbf{A}} &= \xi_x\mathbf{A} + \xi_y\mathbf{B} + \xi_z\mathbf{C} \\ \hat{\mathbf{B}} &= \eta_x\mathbf{A} + \eta_y\mathbf{B} + \eta_z\mathbf{C} \\ \hat{\mathbf{C}} &= \zeta_x\mathbf{A} + \zeta_y\mathbf{B} + \zeta_z\mathbf{C}\end{aligned} \tag{2.24}$$

where

$$\mathbf{A} = \begin{bmatrix} 0 & 1 & 0 & 0 & 0 \\ -u^2 + \frac{\gamma-1}{2}V_M^2 & (3-\gamma)u & (1-\gamma)v & (1-\gamma)w & \gamma - 1 \\ -vu & v & u & 0 & 0 \\ -wu & w & 0 & u & 0 \\ -\gamma eu + u(\gamma-1)V_M^2 & \gamma e - \frac{(\gamma-1)}{2}(2u^2 + V_M^2) & (1-\gamma)uv & (1-\gamma)uw & \gamma u \end{bmatrix}, \tag{2.25}$$

$$\mathbf{B} = \begin{bmatrix} 0 & 0 & 1 & 0 & 0 \\ -uv & v & u & 0 & 0 \\ -v^2 + \frac{\gamma-1}{2}V_M^2 & (1-\gamma)u & (3-\gamma)v & (1-\gamma)w & \gamma - 1 \\ -wv & 0 & w & v & 0 \\ -\gamma ev + v(\gamma-1)V_M^2 & (1-\gamma)uv & \gamma e - \frac{(\gamma-1)}{2}(2v^2 + V_M^2) & (1-\gamma)vw & \gamma v \end{bmatrix}, \tag{2.26}$$

$$\mathbf{C} = \begin{bmatrix} 0 & 0 & 0 & 1 & 0 \\ -uw & w & 0 & u & 0 \\ -vw & 0 & w & v & 0 \\ -w^2 + \frac{\gamma-1}{2}V_M^2 & (1-\gamma)u & (1-\gamma)v & (3-\gamma)w & \gamma - 1 \\ -\gamma ew + w(\gamma-1)V_M^2 & (1-\gamma)uw & (1-\gamma)vw & \gamma e - \frac{(\gamma-1)}{2}(2w^2 + V_M^2) & \gamma w \end{bmatrix} \tag{2.27}$$

and $V_M^2 = u^2 + v^2 + w^2$.

The eigenvalues of $\hat{\mathbf{A}}$ are: $U, U, U, U + c\sqrt{\xi_x^2 + \xi_y^2 + \xi_z^2}$ and $U - c\sqrt{\xi_x^2 + \xi_y^2 + \xi_z^2}$; the eigenvalues of $\hat{\mathbf{B}}$ are: $V, V, V, V + c\sqrt{\eta_x^2 + \eta_y^2 + \eta_z^2}$ and $V - c\sqrt{\eta_x^2 + \eta_y^2 + \eta_z^2}$; the eigenvalues of $\hat{\mathbf{C}}$ are: $W, W, W, W + c\sqrt{\zeta_x^2 + \zeta_y^2 + \zeta_z^2}$ and $W - c\sqrt{\zeta_x^2 + \zeta_y^2 + \zeta_z^2}$.

2.2.5 Turbulence Model

The turbulence model implemented in the SotonCAA code is Spalart-Allmaras (SA) [79] one-equation turbulence model which solves a single partial differential equation for a working variables related to the turbulent viscosity. It is written as

$$\begin{aligned} \frac{\partial \hat{\nu}}{\partial t} + u_j \frac{\partial \hat{\nu}}{\partial x_j} = & C_{b_1}[1 - f_{t_2}]\Omega\hat{\nu} \\ & + \frac{M_\infty}{Re_L}\left\{C_{b_1}[(1-f_{t_2})f_{\nu_2} + f_{t_2}]\frac{1}{\kappa^2} - C_{w_1}f_w\right\}\left(\frac{\hat{\nu}}{d}\right)^2 \\ & - \frac{M_\infty}{Re_L}\frac{C_{b_2}}{\sigma}\hat{\nu}\frac{\partial^2\hat{\nu}}{\partial x_j^2} \\ & + \frac{M_\infty}{Re_L}\frac{1}{\sigma}\frac{\partial}{\partial x_j}\left[(\nu + (1+C_{b_2})\hat{\nu})\frac{\partial\hat{\nu}}{\partial x_j}\right] \end{aligned} \tag{2.28}$$

where d is the distance to the closest wall and $\hat{\nu}$ is the working variable. The turbulent eddy viscosity ν_t is obtained from,

$$\nu_t = \rho\hat{\nu}f_{\nu_1}, \qquad f_{\nu_1} = \frac{\chi^3}{\chi^3 + C_{\nu_1}^3}, \qquad \chi \equiv \frac{\hat{\nu}}{\nu}. \tag{2.29}$$

The other variables in Equation 2.28 can be determined by

$$f_{t_2} = C_{t_3}\exp(-C_{t_4}\chi^2), \tag{2.30}$$

$$f_W = g\left[\frac{1 + C_{W_3}^6}{g^6 + C_{W_3}^6}\right]\frac{1}{6} = \left[\frac{g^{-6} + C_{W_3}^{-6}}{1 + C_{W_3}^{-6}}\right]^{-\frac{1}{6}}, \tag{2.31}$$

$$g = r + C_{W_2}(r^6 - r), \tag{2.32}$$

$$r = \frac{\hat{\nu}}{\hat{S}\left(\frac{Re}{M_\infty}\right)\kappa^2 d^2} \tag{2.33}$$

where

$$\hat{S} = \Omega + \frac{\hat{\nu} f_{\nu_2}}{\left(\frac{Re}{M_\infty}\right)\kappa^2 d^2}, \tag{2.34}$$

$$f_{\nu_2} = 1 - \frac{\chi}{1 + \chi f_{\nu_1}}, \tag{2.35}$$

$$C_{W_1} = \frac{C_{b_1}}{\kappa^2} + \frac{(1 + C_{b_2})}{\sigma}. \tag{2.36}$$

The constants are

$$\begin{array}{lll} C_{b_1} = 0.1355, & \sigma = \frac{2}{3}, & C_{b_2} = 0.622, \\ \kappa = 0.41, & C_{W_3} = 2.0, & C_{W_2} = 0.3, \\ C_{\nu_1} = 7.1, & C_{t_3} = 1.2, & C_{t_4} = 0.5. \end{array} \tag{2.37}$$

2.2.6 Subgrid Stress Model for LES

The idea of large eddy simulation is that as the large scale eddies of flow are dependent on the geometry and the small scale structures are more universal, it is possible to solve the large scale eddies explicitly and model the effect of small scale structures. To decompose an arbitrary variable φ into its large scale and small scale (the so called subgrid scales in LES) components, the variable is filtered as:

$$\bar{\varphi} = \int_\vartheta \aleph \varphi d\vartheta \tag{2.38}$$

where $\aleph$ is the grid filtering function and the integration is carried out over the entire flow domain. Then the φ can be written as:

$$\varphi = \bar{\varphi} + \varphi_{sg} \tag{2.39}$$

where the $\bar{\varphi}$ is the large scale component and the φ_{sg} is the subgrid scales component of φ. The Favre-averaged variable is defined as

$$\tilde{\varphi} = \frac{\overline{\rho\varphi}}{\bar{\rho}} \tag{2.40}$$

with this formulation, the $\hat{\mathbf{Q}}$ in Equation 2.1 can be write as $\hat{\mathbf{Q}} = (1/J)[\bar{\rho}, \bar{\rho}\tilde{u}, \bar{\rho}\tilde{v}, \bar{\rho}\tilde{w}, \bar{\rho}\tilde{E}]$ and the Equations 2.2$\sim$ 2.4 become:

$$\hat{\mathbf{F}} = \frac{1}{J}\begin{bmatrix} \bar{\rho}\tilde{U} \\ \bar{\rho}\tilde{u}\tilde{U} + \xi_x\bar{p} \\ \bar{\rho}\tilde{v}\tilde{U} + \xi_y\bar{p} \\ \bar{\rho}\tilde{w}\tilde{U} + \xi_z\bar{p} \\ \bar{\rho}\tilde{E}\tilde{U} + \xi_{x_i}u_i\bar{p} \end{bmatrix}, \tag{2.41}$$

$$\hat{\mathbf{G}} = \frac{1}{J}\begin{bmatrix} \bar{\rho}\tilde{V} \\ \bar{\rho}\tilde{u}\tilde{V} + \eta_x\bar{p} \\ \bar{\rho}\tilde{v}\tilde{V} + \eta_y\bar{p} \\ \bar{\rho}\tilde{w}\tilde{V} + \eta_z\bar{p} \\ \bar{\rho}\tilde{E}\tilde{V} + \eta_{x_i}u_i\bar{p} \end{bmatrix}, \tag{2.42}$$

$$\hat{\mathbf{H}} = \frac{1}{J}\begin{bmatrix} \bar{\rho}\tilde{W} \\ \bar{\rho}\tilde{u}\tilde{W} + \zeta_x\bar{p} \\ \bar{\rho}\tilde{v}\tilde{W} + \zeta_y\bar{p} \\ \bar{\rho}\tilde{w}\tilde{W} + \zeta_z\bar{p} \\ \bar{\rho}\tilde{E}\tilde{W} + \zeta_{x_i}u_i\bar{p} \end{bmatrix}, \tag{2.43}$$

$$\hat{\mathbf{F}}_v = \frac{1}{J}\begin{bmatrix} 0 \\ \xi_{x_i}(\tilde{\sigma}_{i1} + \tau_{i1}) \\ \xi_{x_i}(\tilde{\sigma}_{i2} + \tau_{i2}) \\ \xi_{x_i}(\tilde{\sigma}_{i3} + \tau_{i3}) \\ \xi_{x_i}[\tilde{u}_j(\tilde{\sigma}_{ij} + \tau_{ij}) - \tilde{q}_i - \ell_i] \end{bmatrix}, \tag{2.44}$$

$$\hat{\mathbf{G}}_v = \frac{1}{J}\begin{bmatrix} 0 \\ \eta_{x_i}(\tilde{\sigma}_{i1} + \tau_{i1}) \\ \eta_{x_i}(\tilde{\sigma}_{i2} + \tau_{i2}) \\ \eta_{x_i}(\tilde{\sigma}_{i3} + \tau_{i3}) \\ \eta_{x_i}[\tilde{u}_j(\tilde{\sigma}_{ij} + \tau_{ij}) - \tilde{q}_i - \ell_i] \end{bmatrix}, \tag{2.45}$$

$$\hat{\mathbf{H}}_v = \frac{1}{J}\begin{bmatrix} 0 \\ \zeta_{x_i}(\tilde{\sigma}_{i1} + \tau_{i1}) \\ \zeta_{x_i}(\tilde{\sigma}_{i2} + \tau_{i2}) \\ \zeta_{x_i}(\tilde{\sigma}_{i3} + \tau_{i3}) \\ \zeta_{x_i}[\tilde{u}_j(\tilde{\sigma}_{ij} + \tau_{ij}) - \tilde{q}_i - \ell_i] \end{bmatrix}. \tag{2.46}$$

In this expression, the components of the stress tensor and heat flux vector are:

$$\tilde{\sigma}_{ij} = \tilde{\mu}\left(\frac{\partial\xi_k}{\partial x_j}\frac{\partial\tilde{u}_i}{\partial\xi_k} + \frac{\partial\xi_k}{\partial x_i}\frac{\partial\tilde{u}_j}{\partial\xi_k} - \frac{2}{3}\delta_{ij}\frac{\partial\xi_l}{\partial x_k}\frac{\partial\tilde{u}_k}{\partial\xi_l}\right), \tag{2.47}$$

$$\tilde{q}_i = -\left[\frac{\tilde{\mu}}{(\gamma-1)Pr}\right]\frac{\partial \xi_j}{\partial x_i}\frac{\partial \tilde{T}}{\partial \xi_j} \tag{2.48}$$

and the corresponding subgrid scale stress and heat flux are given as:

$$\tau_{ij} = -\frac{Re_L}{M_\infty}\bar{\rho}(\widetilde{u_i u_j} - \tilde{u}_i\tilde{u}_j), \tag{2.49}$$

$$\ell_i = \frac{Re_L}{M_\infty}\bar{\rho}(\widetilde{u_i T} - \tilde{u}_i\tilde{T}). \tag{2.50}$$

They are obtained from the Smagorinsky subgrid stress (SGS) model [80]:

$$\tau_{ij} - \frac{1}{3}\tau_{kk}\delta_{ij} = -2\mu_t\left(\tilde{\phi}_{ij} - \frac{1}{3}\tilde{\phi}_{kk}\delta_{ij}\right) \tag{2.51}$$

where

$$\tilde{\phi}_{ij} = \frac{1}{2}\left(\frac{\partial \xi_k}{\partial x_j}\frac{\partial \tilde{u}_i}{\partial \xi_k} + \frac{\partial \xi_k}{\partial x_i}\frac{\partial \tilde{u}_j}{\partial \xi_k}\right) \tag{2.52}$$

and

$$\mu_t = \frac{Re_L}{M_\infty}C_{sgs}\Delta^2\bar{\rho}\tilde{\phi}_M. \tag{2.53}$$

The subgrid scale heat flux vector is calculated with a constant turbulent Prandtl number assumption:

$$\ell_i = -\left(\frac{\mu_t}{Pr_t}\right)\frac{\partial \xi_j}{\partial x_i}\frac{\partial \tilde{T}}{\partial \xi_j}. \tag{2.54}$$

In the model, C_{sgs} is the eddy-viscosity model constant which is chosen as 0.008464. The $\tilde{\phi}_M$ is the magnitude of the rate-of-strain tensor which is defined as:

$$\tilde{\phi}_M = (2\tilde{\phi}_{ij}\tilde{\phi}_{ij})^{1/2} \tag{2.55}$$

and the eddy-viscosity length scale is obtained as:

$$\Lambda = \left(\frac{1}{J}\right)^{1/3}. \tag{2.56}$$

The isotropic part of the stress tensor in Equations 2.51, $\frac{1}{3}\tau_{kk}$, is commonly neglected in a low Mach number flow calculation.

2.2.7 Boundary Conditions

Several boundary condition types are used in numerical simulations: no-slip, farfield boundary, impedance boundary condition, etc.

2.2.7.1 No-slip Boundary

The no-slip boundary condition is an adiabatic, viscous surface boundary condition. The no-slip condition is imposed by setting the three Cartesian velocity components to zero. The pressure on the wall is determined from linear extrapolation from the first two adjacent interior mesh points. The wall temperature is set to ensure that the adiabatic condition is satisfied.

2.2.7.2 Farfield Boundary

The farfield boundary condition is obtained using an explicit buffer zone method [81]. The computational grid is extended to create an extra layer, buffer zone, surrounding the main computational domain and in the buffer zone, the solution vector is explicitly damped after each time step using

$$\mathbf{Q}^{n+1} = \acute{\mathbf{Q}}^{n+1} - \varsigma(\acute{\mathbf{Q}}^{n+1} - \mathbf{Q}_{target}) \tag{2.57}$$

where $\acute{\mathbf{Q}}^{n+1}$ is the solution vector after each time step and $\mathbf{Q}_{target}$ is the expected value in the buffer zone. The damping coefficient, ς , varies smoothly according to the function,

$$\varsigma(x_{bz}) = \varsigma_{max}(1 + \frac{x_{bz} - L_{bz}}{L_{bz}})^{\beta_{bz}} \tag{2.58}$$

where L_{bz} is the width of the buffer zone, x_{bz} is the distance measured from the inner boundary of the buffer zone and ς_{max} and β_{bz} are coefficients which determine the shape of the damping function. In the present study, ς_{max}=1.0, β_{bz}=2.5 are used. The target values of the solution vector are set equal to the initial free stream values.

2.2.7.3 Impedance Boundary

On the acoustically treated wall, the time domain impedance boundary condition proposed by Fung *et al.* [68] is applied. The details of the method are given in Appendix A. In the viscous simulation, the acoustic variables are obtained by subtracting the local mean values from the total unsteady solutions. The tangential velocity of wall are set as zero to satisfy the no-slip condition in that direction. The wall temperature is set to ensure that the adiabatic condition is satisfied.

2.3 Linearized Acoustics Solver

The computational acoustics code SotonLEE is used for the computation of the sound field. SotonLEE is an explicit multi-block solver for structured grids which solves the linearized Euler equations. In Cartesian system, the linearized Euler equation can be written as

$$\begin{aligned} &\frac{\partial \rho'}{\partial t} + \nabla \cdot (\rho_0 \mathbf{u}' + \mathbf{u}_0 \rho') = 0 \\ &\frac{\partial \mathbf{u}'}{\partial t} + (\mathbf{u}_0 \cdot \nabla)\mathbf{u}' + (\mathbf{u}' \cdot \nabla)\mathbf{u}_0 + \frac{\nabla p'}{\rho_0} = 0 \end{aligned} \tag{2.59}$$

where the differential operator ∇ is given by

$$\nabla = \frac{\partial}{\partial x}\hat{\underline{i}} + \frac{\partial}{\partial y}\hat{\underline{j}} + \frac{\partial}{\partial z}\hat{\underline{k}} \tag{2.60}$$

and x, y, z are Cartesian coordinates; ρ is density, p is pressure and $\mathbf{u}$ is the velocity vector. Subscript $()_0$ sign denotes time averaged mean value and prime sign denotes the perturbation value.

To model the acoustic sources, the acoustic perturbation equations (APE) proposed in Ref. [82] are adopted here:

$$\begin{aligned} &\frac{\partial \rho'}{\partial t} + \nabla \cdot (\rho_0 \mathbf{u}' + \mathbf{u}_0 \rho') = 0 \\ &\frac{\partial \mathbf{u}'}{\partial t} + \nabla(\mathbf{u}_0 \cdot \mathbf{u}') + \nabla(\frac{p'}{\rho_0}) = \mathbf{q}_m \end{aligned} \tag{2.61}$$

where $\mathbf{q}_m$ is the source term vector which is defined in APE-4 system of Ref. [82] as the negative value of the perturbation of the Lamb vector ($\mathbf{L}$):

$$\mathbf{q}_m = -\mathbf{L}' = -(\omega \times \mathbf{u})' \tag{2.62}$$

where $\omega = \nabla \times \mathbf{u}$.

The spatial discretization and filtering scheme of SotonLEE are same as that of SotonCAA. The temporal integration scheme is the explicit Runge-Kutta scheme [21] and the buffer zone is applied surrounding the computation domain where the target values are set using the mean values. The slip wall condition is applied for the hard wall and the impedance boundary condition is applied for the lined wall.

2.4 Radiation Model

To resolve the acoustic field in the far field an integral technique, based on the Ffowcs Williams and Hawkings equation [11] has been implemented. The FW-H equation is an exact rearrangement of the Navier-Stokes equation and is appropriate for computing the acoustic field when solid boundaries play a direct role in the generation of sound. The solution of the FW-H equation is obtained in the terms of volume and surface integrals and may be used to predict the far field acoustic signal based solely on near field data. The FW-H method has typically been applied by having the integration surface coincide with solid boundaries, but the method is still applicable when the surface is off the body and permeable. Thus the FW-H equation is valid even if the integration surface lies in the nonlinear region [83]. This flexibility, coupled with the fact that the solution is often well approximated by the surface integrals alone, makes the FW-H method an attractive technique for predicting the far field acoustic signal. In the followings a derivation of the FW-H equation, as employed in the acoustic propagation code, is given.

The FW-H equation may be derived by considering a generic body with surface S, described by the equation $f_s = 0$, immersed in a fluid. If the flow variables are regarded as generalized functions the validity of the equation of fluid motion may be extended to all space through the use of the Heaviside function. The resulting equations may then be combined in the manner originally proposed by Lighthill to form an inhomogeneous wave equation valid throughout all space. The equation is known as FW-H equation and in differential form may be written

$$\left(\frac{1}{c_0^2}\frac{\partial^2}{\partial t^2} - \frac{\partial^2}{\partial x_i^2}\right)\left(c_0^2(\rho-\rho_0)H(f_s)\right) = \frac{\partial^2}{\partial x_i \partial x_j}\left(T_{ij}H(f_s)\right) - \frac{\partial}{\partial x_i}\left(L_i\delta(f_s)\right) + \frac{\partial}{\partial t}\left(U_n\delta(f_s)\right) \quad (2.63)$$

where

$$T_{ij} = \rho u_i u_j - \sigma_{ij} + [(p-p_o) - c_o^2(\rho-\rho_0)]\delta_{ij}, \quad (2.64)$$

$$L_i = L_{ij}\hat{n_j} = [\rho u_i(u_j - v_j) + (p-p_0)\delta_{ij} - \sigma_{ij}]\hat{n_j}, \quad (2.65)$$

$$U_n = U_i\hat{n_i} = [\rho(u_i - v_i) + \rho_0 v_i]\hat{n_i} \quad (2.66)$$

and $H()$ is the Heaviside function, $\delta()$ is the Dirac delta function, u_i is the fluid velocity component in the x_i direction, v_i is the integration surface S velocity component in the x_i direction and $\hat{n_i}$ is the component of the unit outward normal vector $\hat{\mathbf{n}}$ to surface S in the x_i direction.

T_{ij} is known as the Lighthill stress tensor, and represents the volume quadrupole sources. The components of T_{ij} are the Reynolds stresses, the viscous stresses and terms relating to entropy and fluid inhomogeneity. L_i is a surface dipole. The first term of L_i relates to the flux of momentum across the surface S, while the rest terms of L_i, $(p - p_0)\delta_{ij} - \sigma_{ij}$, is the force per unit area applied over S. U_n is a surface monopole. It is composed of two components. The first represents the mass flux through the surface, while the second is the equivalent mass flux due to the surface motion.

Away from the source region Equation 2.63 reduces to the homogenous wave equation and the term $c_0^2(\rho - \rho_0)$ tends to the acoustic pressure. An integral formula expressing the solution of Equation 2.63 may be obtained in terms of a Green's function $G(\mathbf{x}, t|\mathbf{y}, \tau)$ satisfying the equation

$$\left(\frac{1}{c_0^2}\frac{\partial^2}{\partial t^2} - \frac{\partial^2}{\partial x_i^2}\right) G(\mathbf{x}, t|\mathbf{y}, \tau) = \delta(\mathbf{x} - \mathbf{y})\delta(t - \tau) \tag{2.67}$$

for an impulsive point source. The Green's function $G(\mathbf{x}, t|\mathbf{y}, \tau)$ may be thought of as representing the response at $\mathbf{x}$ and the time t due to an impulsive forcing at the point $\mathbf{y}$ and the time τ. The solution is formed by multiplying Equation 2.67 by the right-hand-side of Equation 2.63 at position $\mathbf{y}$ and the time τ and integrating over all space and time, including the volume interior to S. Exploiting the sifting property of the Dirac delta functions in Equation 2.67, an integral equation for the acoustic pressure p' at time t and position $\mathbf{x}$ may be written

$$\begin{aligned} p'(\mathbf{x}, t) \quad &= \int_{-\infty}^{\infty} \iiint_V \left[G \frac{\partial^2}{\partial y_i \partial y_j} \left(T_{ij} H(f_s) \right) \right] dV(\mathbf{y}) d\tau \\ &- \int_{-\infty}^{\infty} \iiint_V \left[G \frac{\partial}{\partial\, y_i} \left(L_i \delta(f_s) \right) - G \frac{\partial}{\partial \tau} \left(U_n \delta(f_s) \right) \right] dV(\mathbf{y}) d\tau. \end{aligned} \tag{2.68}$$

Assuming the volume sources are limited to a finite region of space, the spatial and temporal derivative may be moved from the source terms to the Green's function using partial integration to obtain

$$p'(\mathbf{x}, t) \quad = \int_{-\infty}^{\infty} \iiint_{V(\tau)} T_{ij} \frac{\partial^2 G}{\partial y_i \partial y_j} dV(\mathbf{y}) d\tau + \int_{-\infty}^{\infty} \iint_{S(\tau)} L_i \frac{\partial G}{\partial y_i} dS(\mathbf{y}) d\tau$$

$$-\int_{-\infty}^{\infty}\iint_{S(\tau)} U_n \frac{\partial G}{\partial \tau} dS(\mathbf{y}) d\tau \tag{2.69}$$

where the properties of the Heaviside function have been used to limit the first volume integral to the region external to S, and the sifting property of the Dirac delta functions has been used to reduce the remaining volume integrals to surface integrals.

Equation 2.69 is the fundamental equation governing the generation of sound in the presence of solid boundaries. It is exact and applies to any region which is bounded by permeable surfaces in arbitrary motion. When the righthand side of this equation is known the pressure perturbations in the sound field can be calculated. Substitution of a Green's function appropriate to the particular problem considered completes the solution. In this work the free space Green's function is used. The three-dimensional free space Green's function is

$$G_0(\mathbf{x}, t|\mathbf{y}, \tau)) = \frac{\delta(g)}{4\pi r} \tag{2.70}$$

where $g = \tau - t + r/c_0$ and $r = |\mathbf{x} - \mathbf{y}|$ is the distance between observer and source.

To obtain the specific formulation of the FW-H equation implemented numerically we first recall the elementary symmetry properties of the free space Green's function

$$\frac{\partial G_0}{\partial t} = -\frac{\partial G_0}{\partial \tau} \qquad \text{and} \qquad \frac{\partial G_0}{\partial x_i} = \frac{\partial G_0}{\partial y_i}. \tag{2.71}$$

Using these properties the spatial and temporal derivatives of G_0 with respect to source coordinate $\mathbf{y}$ and time τ are replaced by derivatives with respect to observer coordinate $\mathbf{x}$ and time t. Then, as the integration is performed on the source coordinate $\mathbf{y}$ and time τ, the spatial and temporal derivatives may be moved out of the integrals to obtain

$$\begin{aligned} p'(\mathbf{x}, t) \quad &= \frac{\partial^2}{\partial x_i \partial x_j} \int_{-\infty}^{\infty} \iiint_{V(\tau)} T_{ij} \frac{\delta(g)}{4\pi r} dV(\mathbf{y}) d\tau - \frac{1}{c_0} \frac{\partial}{\partial t} \int_{-\infty}^{\infty} \iint_{S(\tau)} L_i \hat{r}_i \frac{\delta(g)}{4\pi r} dS(\mathbf{y}) d\tau \\ &+ \int_{-\infty}^{\infty} \iint_{S(\tau)} L_i \hat{r}_i \frac{\delta(g)}{4\pi r^2} dS(\mathbf{y}) d\tau + \frac{\partial}{\partial t} \int_{-\infty}^{\infty} \iint_{S(\tau)} U_n \frac{\delta(g)}{4\pi r} dS(\mathbf{y}) d\tau \end{aligned} \tag{2.72}$$

where $\hat{r}_i$ is the component of the unit vector $\hat{\mathbf{r}}$ in the x_i direction and $\hat{\mathbf{r}} = (\mathbf{x} - \mathbf{y})/|(\mathbf{x} - \mathbf{y})|$.

The identity [84]

$$\frac{\partial}{\partial x_i}\left(\frac{\delta(g)}{4\pi r}\right) = \frac{1}{c_0}\frac{\partial}{\partial t}\left(\frac{\hat{r}_i\delta(g)}{4\pi r}\right) - \frac{\hat{r}_i\delta(g)}{4\pi r^2} \tag{2.73}$$

has been used to eliminate the spatial derivative in the second source term. To evaluate the integrals over the delta functions it is convenient to introduce a coordinate system in which the surface $S(\tau)$ is stationary. In general, the surface may move arbitrarily and it would be appropriate to introduce a Lagrangian coordinate $\zeta_L(\mathbf{y},\tau)$. However, for the work undertaken here, it is sufficient to consider the surface to be rigid, and restrict our attention to a Cartesian coordinate system that simply translates with velocity U_s. The Jacobian of the transform between the two Cartesian coordinate is taken to be unity, as is the ratio of the area elements $dS(\zeta_L)/dS(\mathbf{y})$. In the translating coordinate system ζ_L the volume and surface integrals are independent of τ. Therefore, the order of the integration may be interchanged and integration with respect to τ can be carried out to obtain the FW-H equation in source fixed coordinates

$$\begin{aligned} 4\pi p'(\mathbf{x},t) \quad &= \frac{\partial^2}{\partial x_i \partial x_j}\iiint_V \left[\frac{T_{ij}}{r|1-M_r|}\right]_{r^+} dV(\zeta_L) + \iint_S \left[\frac{L_r}{r^2|1-M_r|}\right]_{r^+} dS(\zeta_L) \\ &\quad + \frac{1}{c_0}\frac{\partial}{\partial t}\iint_S \left[\frac{U_0 c_0 - L_r}{r|1-M_r|}\right]_{r^+} dS(\zeta_L) \end{aligned} \tag{2.74}$$

where $M_r = M_i\hat{r}_i$ is the projection of the local surface Mach number $M_i = v_i/c_0$ in the radiation direction, $L_r = L_i\hat{r}_i$, and the notation $[]_{r^+}$ indicates the quantity enclosed within the brackets is to be evaluated at position ζ_L and the retarded time $\tau^+ = t - |\mathbf{x} - \mathbf{y}(\zeta_L,\tau^+)|/c_0$.

To complete the derivation we note that as $r = |\mathbf{x} - \mathbf{y}(\zeta_L,\tau)|$ is a function of τ, the relation for retarded time $g = \tau - t + r/c_0$ may be used to show

$$\frac{\partial}{\partial t}\Big|_{\mathbf{x}} = \left[\frac{1}{1-M_r}\frac{\partial}{\partial \tau}\Big|_{\mathbf{x}}\right] \tag{2.75}$$

which enables the time derivative to be taken inside the final integral, and evaluated analytically to obtain

$$4\pi p'(\mathbf{x},t) \quad = \frac{\partial^2}{\partial x_i \partial x_j}\iiint_V \left[\frac{T_{ij}}{r|1-M_r|}\right]_{\tau^+} dV(\zeta_L) + \iint_S \left[\frac{\dot{U}_n + U_{\dot{n}}}{r(1-M_r)^2}\right]_{\tau^+} dS(\zeta_L)$$

$$+\frac{1}{c_0}\iint_S\left[\frac{\dot{L}_r}{r(1-M_r)^2}\right]_{\tau^+}dS(\zeta_L)+\iint_S\left[\frac{L_r-L_M}{r^2(1-M_r)^2}\right]_{\tau^+}dS(\zeta_L)$$
$$+\frac{1}{c_0}\iint_S\left[\frac{L_r(r\dot{M}_r+c_0M_r-c_0M^2)}{r^2(1-M_r)^3}\right]_{\tau^+}dS(\zeta_L)$$
$$+\iint_S\left[\frac{U_n(r\dot{M}_r+c_0M_r-c_0M^2)}{r^2(1-M_r)^3}\right]_{\tau^+}dS(\zeta_L) \tag{2.76}$$

where a dot indicates differentiation with respect to τ. Equation 2.76, with the volume quadrupole term neglected, is known as formulation $1A$ of Farassat [85]. It forms the basis of the acoustic propagation code and, expecting the neglection of the quadrupole term, is exact and therefore valid both in the near and far field.

2.5 Summary

This chapter has presented details of the numerical methods employed in this research. Results obtained with these tools are presented in the following chapters.

Chapter 3

2D Slat Trailing Edge Tonal Noise Simulations

3.1 Introduction

Lighthill demonstrated that aerodynamic noise is caused by shear stresses distributed through the fluid [9]. In jet noise, where the sources radiate independently of solid surfaces, the sources are relatively inefficient and obey an M^8 power law. When the sources are associated with flow over a bluff body, such as an aircraft landing gear, the noise obeys an M^6 power law [10]. Noise radiated by turbulence convected past a trailing edge is an efficient type of aerodynamic noise source, and Ffowcs Williams and Hall demonstrated that the scattering effect of the trailing edge increases the efficiency of the sources to an M^5 power law [86]. The fact that slat noise measured for aircraft in flight obeys an M^5 power law [87] is a key point in favour of the slat trailing edge being the dominant sources of noise radiation, although this says nothing about the origins of the turbulence that drives the sources.

The importance of slat noise as a source of community noise disturbance is partly a function of its directivity, with slat noise tending to dominate when the aircraft is in the overhead position, when the aircraft is at its point of closest approach to an observer. It has been argued that this directivity may be associated with the acoustic characteristics of the slat gap, with the local geometry and flow combining to increase further the acoustic efficiency of the trailing edge source and to redirect the sound towards the ground, as illustrated in Figure 3.1.

Besides being dependent on the slat gap geometry, the directivity of slat trailing edge noise will also be a function of the directivity of the source. For a compact aerofoil, such as a helicopter blade, Amiet showed that the trailing edge source

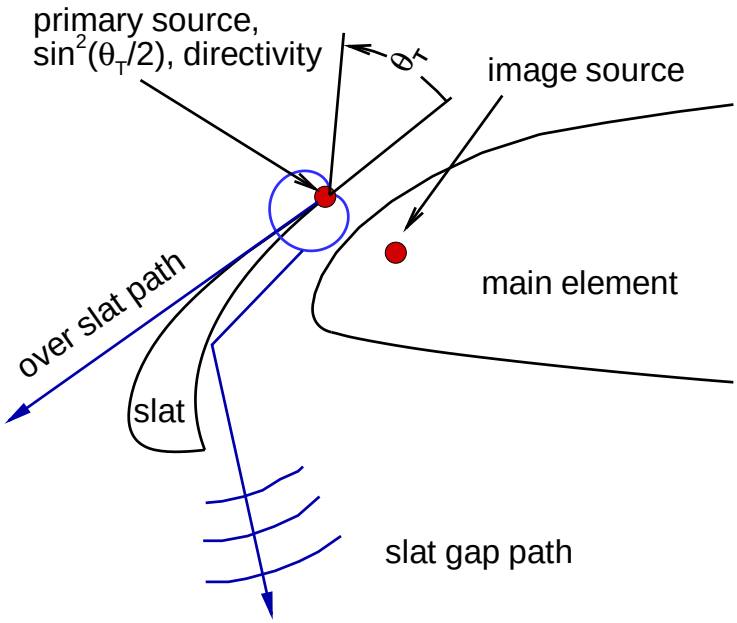

Figure 3.1: Notional acoustic model for slat noise trailing edge sources directivity.

would have a dipole-like $\sin^2(\theta_T)$ directivity [88], whereas Ffowcs Williams and Hall showed that for a semi-infinite plate the directivity would be a $\sin^2(\theta_T/2)$ cardioid shape [86]. The θ_T is the angel relative to the trailing edge as show in Figure 3.1. The directivity of the source and its radiation characteristics into the slat gap is likely to be a complex function of frequency, flow and slat geometry. This creates problems for experimentation at model scale, and a good reason for developing some understanding through the use of numerical models.

The computational work of this chapter is divided into three parts: (1) an URANS simulation using high-order spatial and temporal schemes is conducted for wing with high-lift devices deployed; the computed flow shows the presence of vortex shedding and acoustic sources behind the slat trailing edge; (2) an exercise is conducted on a range of liner impedance values by solving the linearized Euler equations with a representation of the computed acoustic source at the trailing edge of the slat; (3) URANS computations with liner treatment are conducted for the case of a liner on the slat cove and the case of a combination of liner on the slat cove surface and liner on the main element respectively.

Unless indicated otherwise, all values in the followings of this chapter are shown in non-dimensionalized form and all the length scales are non-dimensionalized by $C^* = 0.8$ m which is the chord length of the wing without the slat and flap deployed,

velocities are non-dimensionalized by $c^*_\infty = 340$ m/s, density is non-dimensionalized by $\rho^*_\infty = 1.225$ kg/m^3, pressure is non-dimensionalized by $\rho^*_\infty c^{*2}_\infty$.

3.2 Aeroacoustic Simulation with Hard Wall Condition

3.2.1 Geometry and Flow Condition

A simulation of the viscous flow field without acoustic liner treatment is performed first to capture the pattern of the acoustic field induced by the flow over the slat of the standard high-lift wing. The wing model comprises a main element, a leading edge slat and trailing edge flap geometry (Figure 3.2).

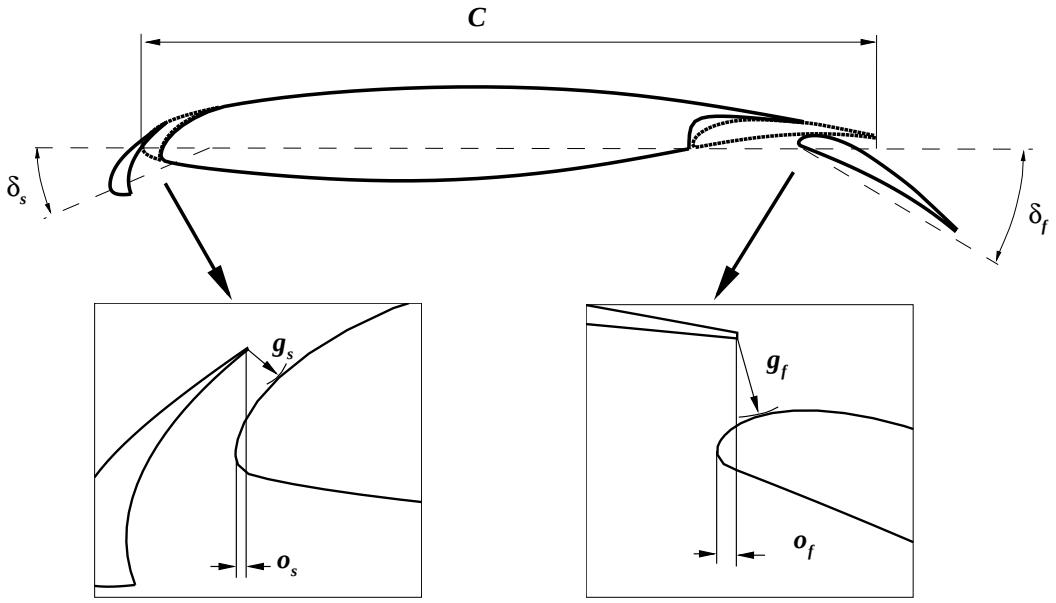

Figure 3.2: Geometry of three-element wing model.

The model has a chord length C of 0.8m without the slat and flap deployed. The slat and flap chords are 12% and 26% of the overall chord length, respectively. The main geometry settings are listed in Table 3.1, where the distances are given as percentages of the chord in the stowed configuration and the angles are the relative angles of the stowed position and the deployed position. The freestream Mach number is 0.2 and the main element angle of attack is 5 degrees, corresponding to a typical approach condition. Reynolds number is 3.6 million, based on the airfoil chord with the high-lift devices retracted.

Parameter	Setting
Slat angle δ_s, degrees	23
Slat gap g_s, %	1.7
Slat overhang o_s, %	0.5
Flap angle δ_f, degrees	32
Flap gap g_f, %	2.0
Flap overhang o_f, %	0.55

Table 3.1: Geometrical settings for high-lift devices.

3.2.2 Grid and Computational Details

The computational domains were designed to resolve the turbulence flow of the high-lift wing. An overview of the grid surrounding the wing is given in Figure 3.3 and the total computational domain ranges form -10 to 10 in both x and y directions. For this high-lift flow computation the grid must be handled with care so that accurate results are obtained with an acceptable number of grid points. The two-dimensional grids have 34 zones, with a total of 393,574 grid points and the 1-1 matched grid block topology is used to achieve the necessary high accuracy.

In the computations, mesh clustering is enforced near solid surfaces, the trailing edge of the slat, in the wake behind the slat, and around the cove of the slat as shown in Figure 3.4. In order to capture the vortex shedding near the trailing-edge, the tailing edge of the slat had a thickness of 7.375×10^{-4} rather than an idealized sharp edge (Figure 3.5) and 49 grid points are used along the thickness of the slat trailing edge. The meshes were designed to ensure $y^+ = O(1)$ along all solid walls. Near the leading-edge slat, the boundary layers were resolved with a minimum of 30 mesh points.

For the URANS simulations, the SA turbulence model is applied and the sixth-order compact scheme [19] is used to approximate the spatial derivatives with the eighth-order filter [73] to prevent the numerical instability. The first step of the explicit LDDRK method [21] is adopted to advance the solution in time with a time step size of 1.0×10^{-6} corresponding to a Courant-Friedrichs-Levy (CFL) number of 0.3. Based on eight 2.2 GHz AMD Opterons CPUs with 16 GB of RAM, 1.16 second CPU time per time step is needed. After the initial transient phase, 2,000,000 steps are advanced for the hard wall case. The hard wall result is used as the initial condition for the lined wall cases and 680,000 steps are calculated for each lined wall case.

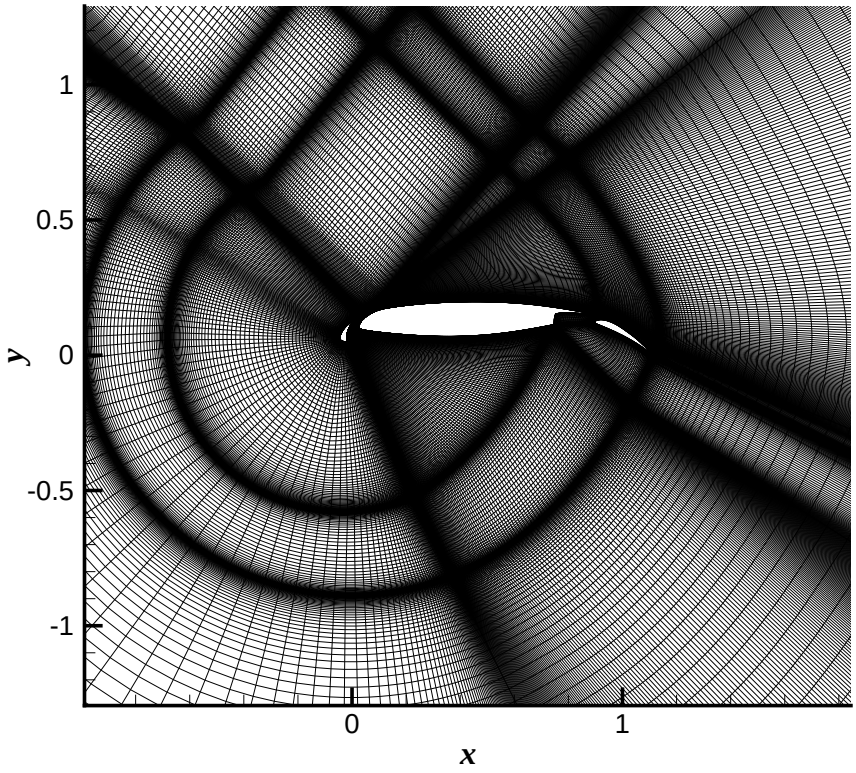

Figure 3.3: A view of the grid surrounding the high-lift wing.

3.2.3 Aeroacoustic Field

The time-accurate solution is quasi-periodic after the initial transient phase. The time-averaged Mach contours near the slat (Figure 3.6) display a recirculation zone in the slat cove, a shear layer originating from the slat cusp and acceleration of the local flow through the gap. In Figure 3.6 the shear layer is seen to separate the gap flow and the recirculation zone. The shear layer thickens as it curves up and reattaches to the cove surface near the slat trailing edge. The shear layer is a good amplifier of the unsteadiness generated near the cusp of the slat. In fact features such as shear layer instabilities and roll-up of large vortical structures were reported in earlier model tests [44, 89]. Due to the excessive dissipative effect of the turbulence model the present simulations fail to capture these phenomena. Figure 3.7 shows an instantaneous vorticity field near the slat cove region, where vorticity is defined as the curl of velocity vector. In the slat cove region the vorticity field is nearly stable and no large scale coherent structures are captured in the current URANS simulations.

Periodic flow fluctuations are mainly concentrated at the slat trailing edge, and

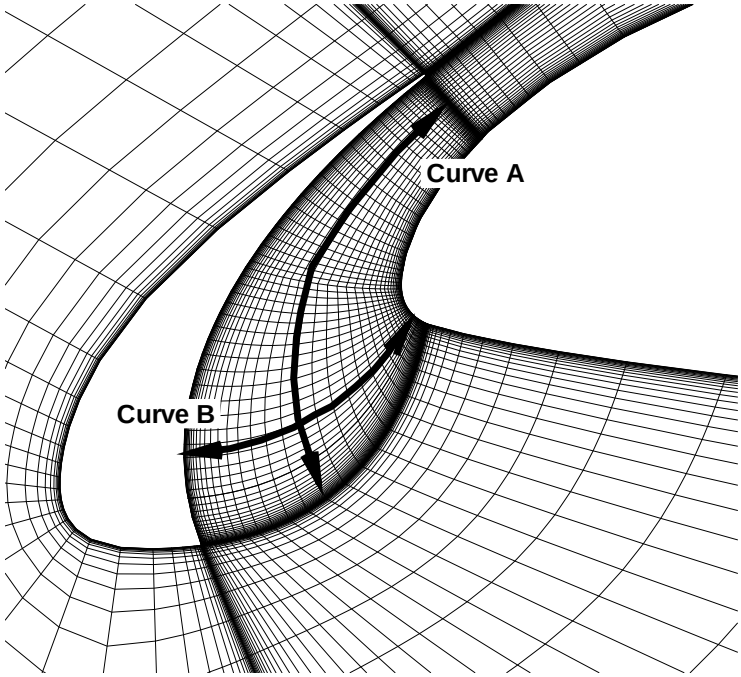

Figure 3.4: A view of the grid in the vicinity of the slat (every 4th point is shown).

are caused by the vortex shedding at that edge because of global wake instability [90, 91]. A region of absolute instability of sufficient length and growth rate existing in the near-wake of a body is a necessary condition for the existence of the shedding. In Figure 3.8, the time-averaged Mach contours near the slat trailing edge show some characteristics of the trailing wake. Because the flow through the gap moves faster, the wake is asymmetric and exhibits an upward deflection. Close to the edge, the wake possesses a region of reversed flow. This region suggests the existence of absolute instabilities which cause the vortex shedding phenomenon. The instantaneous vorticity field behind the slat trailing edge is shown in Figure 3.9. The established vortex street shows the existence of vortex shedding at the trailing edge.

Figure 3.10 shows fluctuating pressure field and established wave patterns near the trailing edge and cove region of the slat. The fluctuating field is obtained by subtracting the local mean values from the total unsteady solutions. The waves are seen to emanate from the trailing edge, impinge on the surface of main element and be reflected, as depicted by the image acoustic source in Figure 3.1. As the waves propagate downward along the slat cove and main element surface there is a distinct interference pattern across the gap and in the cove area, which is indicative

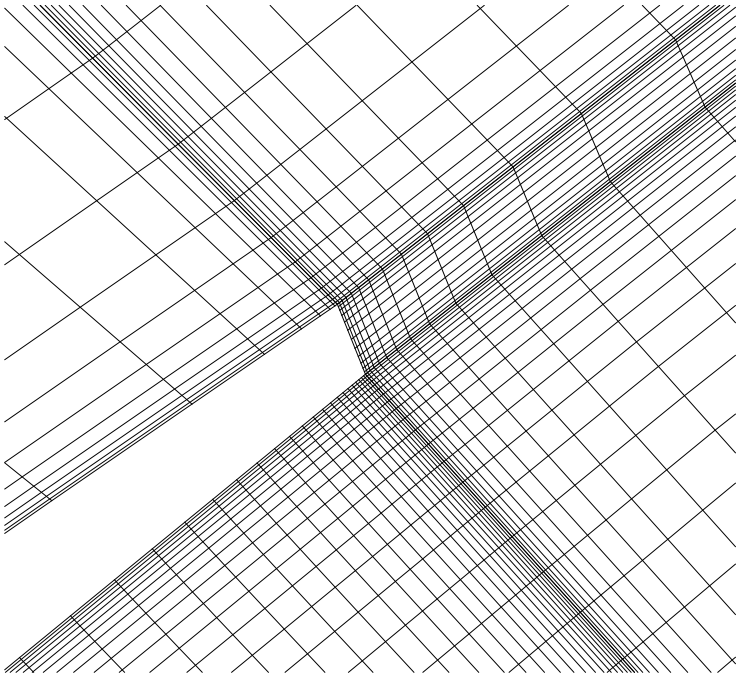

Figure 3.5: A view of the gird near the trailing edge of the slat (every 4th point is shown).

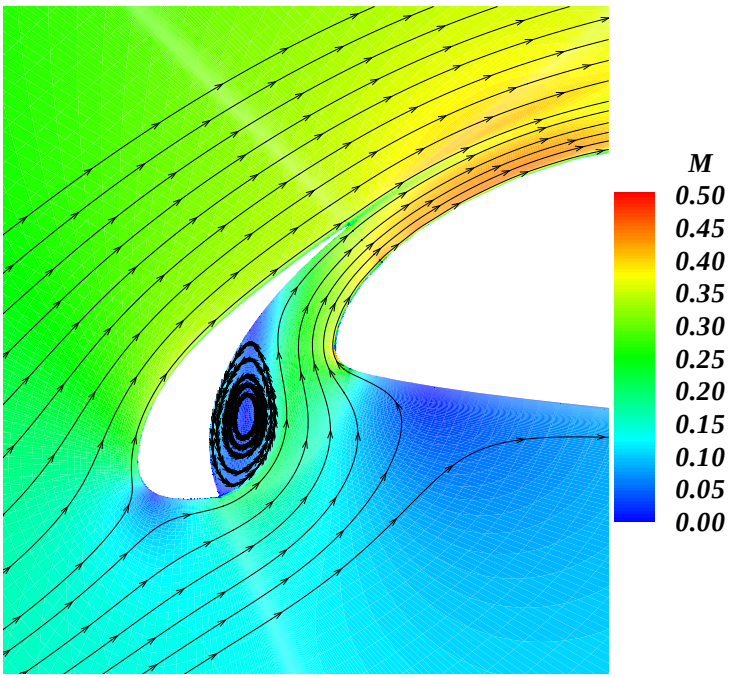

Figure 3.6: Time-averaged Mach contours near the leading edge slat.

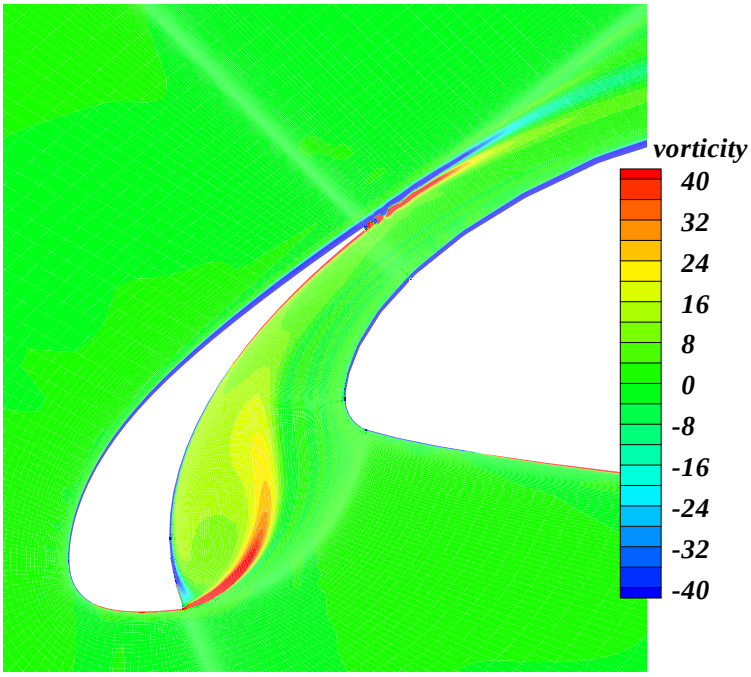

Figure 3.7: Instantaneous vorticity contours near the leading edge slat.

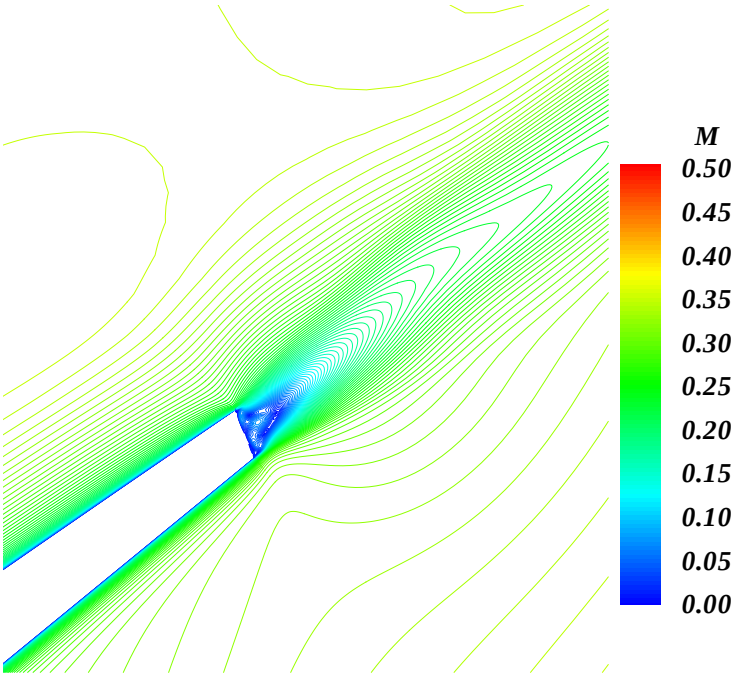

Figure 3.8: Time-averaged Mach contours near the trailing edge of the slat.

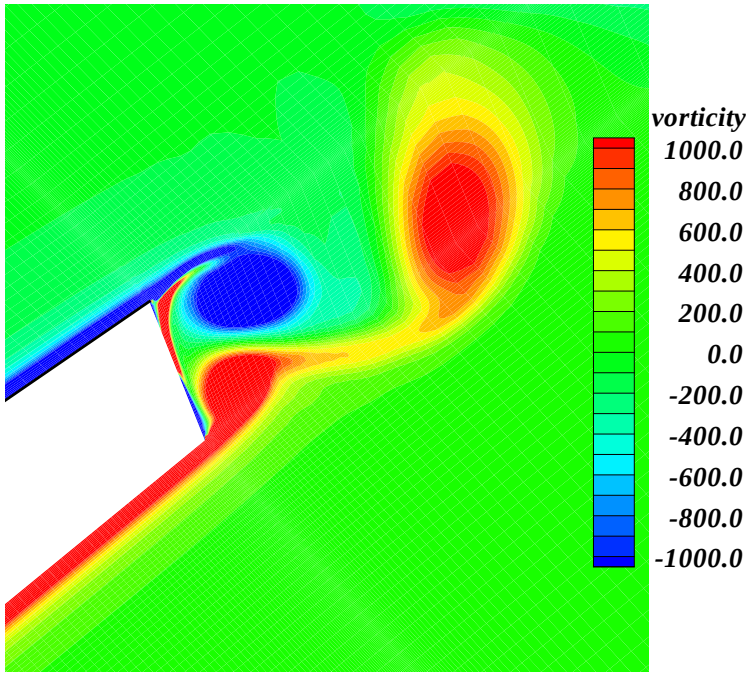

Figure 3.9: Instantaneous vorticity field near the trailing edge of the slat.

of modal propagation in the slat gap and as illustrated by the reflected ray path in Figure 3.1. The waves are channeled down the slowly expanding channel of the slat gap and is diffracted around the edge of the main element and the cusp of the slat. It is directed towards the ground when the aircraft attitude is taken into account. The frequency spectra of the pressure fluctuations near the slat trailing edge is shown in Figure 3.11. The pressure monitoring point is located along the slat chord line and at a distance of 1.475×10^{-3} from the trailing edge of the slat. The spectra is obtained by performing a fast Fourier transform (FFT) of the monitored pressure history. The sampling rate is 1.0×10^5 and a total of 54,400 samples are used corresponding to 32 periods of oscillation. The resulting frequency resolution is about 1.8. Figure 3.11 shows that the self-excited hydrodynamic resonance - vortex shedding - produces sharp peaks in the spectra at harmonics of the fundamental vortex shedding frequency of 58.824 which corresponds a Strouhal number of 0.21 which agrees with the computational and experimental results of the slat trailing edge noise of a EET model [30]. There are elements of broadband noise but it should be noted that the URANS simulation is likely to suppress the broadband noise component.

A refined-grid aeroacoustic calculation with hard wall condition is performed to test the accuracy obtained in the preceding results. The details of the grids are

given in; Grid 2 is the grid used in earlier calculation. The Fourier transform of the monitored pressure history shows that the shedding frequency is 56.471 for the refined-grid calculation. The sound pressure level (SPL) at the monitor point is 127dB for the refined-grid solution and 129 dB for the original-grid solution. Here the SPL is defined as

$$\mathrm{SPL} = 20 \log_{10} \left(p'_{\mathrm{RMS}} / p_{ref} \right) \mathrm{dB} \tag{3.1}$$

where p'_{RMS} is the root mean square (RMS) value of the pressure perturbation and p_{ref} is a reference pressure which equals to 20 μPa.

The small difference in amplitude and frequency of the monitored pressure reveals that the results of original computation have little grid dependency and their accuracy is verified sufficiently.

	Grid 1	**Grid 2**
Grid points along curve A	401	353
Grid points along curve B	257	197
Grid points along slat trailing edge	65	49

Table 3.2: Grid distributions near the trailing edge slat; Curve A and curve B are shown in Figure 3.4.

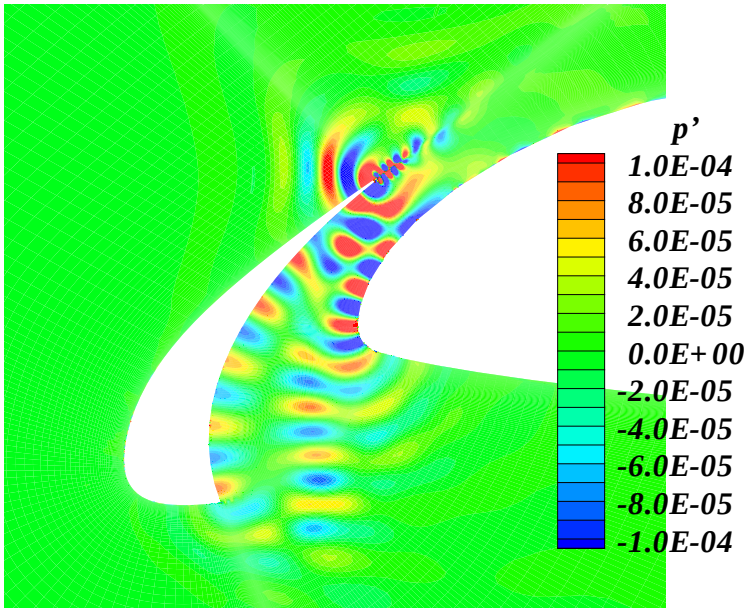

Figure 3.10: Fluctuating pressure field around the slat.

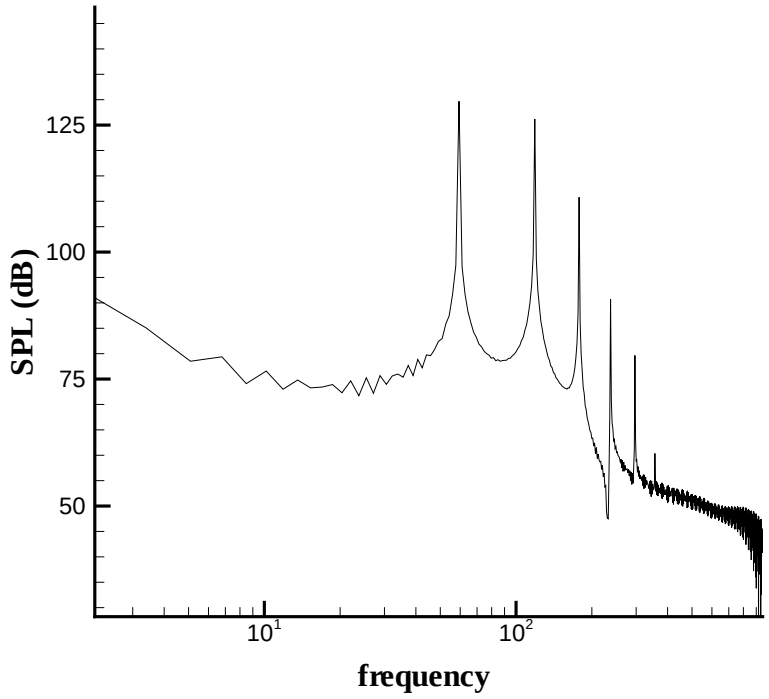

Figure 3.11: Fluctuating pressure spectra near the trailing edge of the slat.

3.3 Acoustic Field Simulation and Liner Impedance Evaluation

3.3.1 Acoustic Modelling and Computation Setup

To assess the noise mitigation effect of the acoustic liners for the slat trailing edge noise and try to find an optimized liner impedance, the acoustic field of the high-lift wing with lined wall is investigated. This part of the study is conducted using the idealized case of zero mean flow. The computational grid used for the slat gap LEE liner study is shown in Figure 3.12. A total of 87,498 grid points are used and the maximum grid size is 1.25×10^{-3}, which gives an equivalent grid resolution of at least 12 PPW for a wave frequency up to 58.824. In the modeling process, the trailing edge of the slat is treated as a sharp edge rather than a blunt one used in the viscous calculation in order to avoid the unnecessary fine grid near the trailing edge of the slat. The fourth-order optimized compact scheme [20] is used to approximate the spatial derivatives with the eighth-order filter [73] to prevent the numerical instability. The explicit LDDRK method [21] is used to advance the solution in time with a time step size of 1.0×10^{-4} corresponding to a CFL number of 0.5. Based on a 3.0 GHz Intel XEON CPU with 2 GB of RAM, 0.9 second CPU

time per time step is required. Every case required 1 hour 42 minutes to complete and a total of 66 cases are assessed.

Based on the viscous flow result the source of noise near the trailing edge is replaced with a dipole with a frequency of 58.824. The dipole is realized by adding a source term q_e to the energy equation of the LEE that can be written as:

$$q_e = A_m \cdot \sin(\omega t) \cdot \exp\left[-\ln(2)\frac{(x-x_1)^2+(y-y_1)^2}{r_{dipole}^2}\right] \\ -A_m \cdot \sin(\omega t) \cdot \exp\left[-\ln(2)\frac{(x-x_2)^2+(y-y_2)^2}{r_{dipole}^2}\right] \tag{3.2}$$

where ω=462, A_m=0.0025ω and r_{dipole}=0.005. Setting the trailing edge of the slat as the origin, (x_1, y_1) and (x_2, y_2) are given as (-0.0001875, 0.000225) and (0.0001875, -0.000225) respectively.

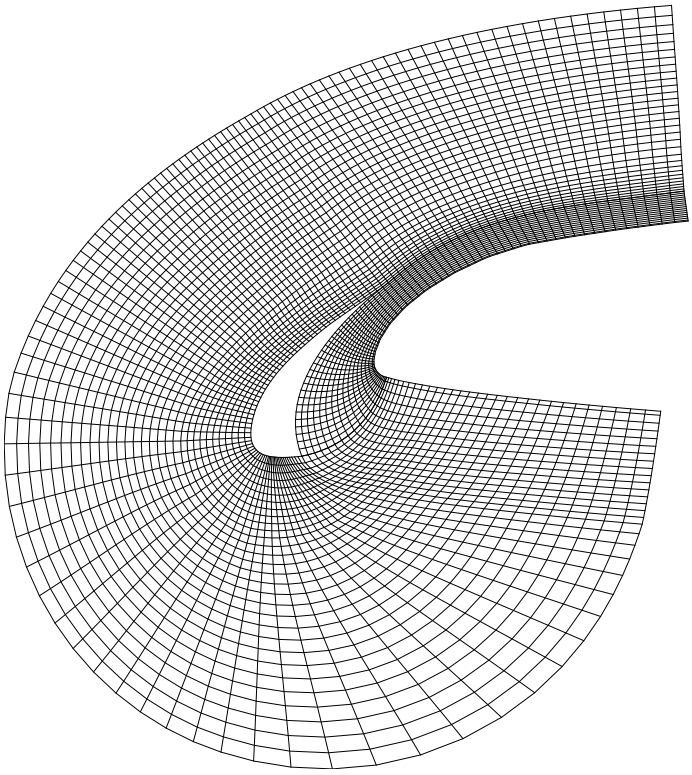

Figure 3.12: Computational grid for liner evaluation (every 4th point is shown).

The liner condition is applied to the slat cove surface and part of the main element surface as shown in Figure 3.13. The slat cove liner starts from the cusp

of the slat, but at the slat trailing edge the available depth is too small to apply a practical liner, the liner treatment is thus only extended to a position where at least 6.25×10^{-3} depth is available The liner length is 76% of the total slat cove surface length. On the basis that the acoustic liner on the main element should probably avoid the leading edge stagnation point, so as to minimize any possible aerodynamic penalty, the liner is started from a position on the suction surface at a distance of 0.01 from the leading edge and is extended for a distance of about six wavelengths at the frequency of 58.824. When slat is at retracted position, the liner on the main element is covered totally by the slat. Numerical tests show that any further extension of the liner treatment on main element would have an insignificant effect on the noise attenuation performance.

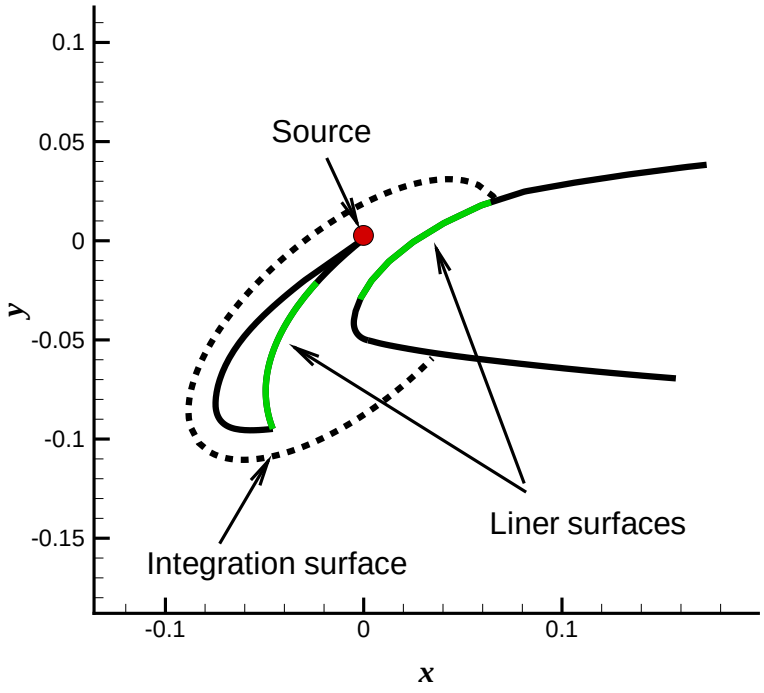

Figure 3.13: A schematic of the LEE liner study.

To provide an assessment of the benefit of the acoustic liners, the farfield directivity is obtained by solving the FW-H equation using formulation 1A of Farassat [85] in which the volume quadrupole terms are neglected. The integration surface for solving the FW-H equation is generated by extruding a curve in the spanwise direction with a span from -0.625 to 0.625. Setting the trailing edge of the slat as the origin, the curve is a portion of an ellipse which is generated by rotating the ellipse anticlockwise by 40 degrees and the ellipse is centered at $x = -0.0085, y = -0.04025$ with a major axis of 0.09675 and a minor axis of 0.0465. The integration surface

is truncated by the main element. The observers are positioned at z=0 on a circle with the radius of 12.5 from the trailing edge of the slat. The objective function for the evaluation process needs to show the difference between the acoustic fields of the wing with hard wall and lined wall as a function of the liner resistance R and reactance X; and the same impedance value are used on both the slat cove liner and the main wing liner. Optimum liner impedance characteristics are found by minimizing the averaged SPL, in decibels, along the observe circle. The objective function can be written as

$$A = 20\log_{10}\frac{\int_{s_0}^{s_1} \mid p'_{rms} \mid_{hard} / \mid p'_{rms} \mid_{lined} ds}{\int_{s_0}^{s_1} ds} \tag{3.3}$$

where A stands for the space averaged attenuation, $\mid p'_{rms} \mid_{hard}$ is the RMS acoustic pressure for the hard wall case and $\mid p'_{rms} \mid_{lined}$ is the RMS acoustic pressure for the lined wall case. s denotes the distance measured along the observe circle. The position of the acoustic source, the integration surface around the slat and the location of the acoustic liners are shown in Figure 3.13.

3.3.2 Acoustic Field Results and Liner Performance

The liner impedance optimization is performed with the slat cove surface and part of the main element surface both lined. The contours of attenuation are plotted in plane of the impedance design variables to obtain the maximum of the objective function (Figures 3.14 and 3.15). A 6×11 grid in the design variable space is used so that a total of 66 cases are assessed. Two evaluations are performed using different monitoring lengths. In the first evaluation (case I) the space averaged attenuation is obtained along the whole observe circle while in the second evaluation (case II) the attenuation is evaluated on a truncated portion of the observe circle, between the observation angles of 240 degrees and 340 degrees. The angle is relative to the x direction and increases anti-clockwise. The results are shown in Figures 3.14 and 3.15; there is a well-defined optimum point: R=1.3 X=-1.9. The different maximum attenuations, 3.2dB for case I and 7.1 dB for case II, indicate the direction dependent characteristics of the attenuation performance. The relatively large region of the impedance plane over which optimal or near optimal liner behavior is predicted suggests that a liner designed with no mean flow should also perform well for the case with a mean flow up to perhaps Mach number 0.3 [92], although the negative mean flow (sound propagating upstream) may be expected to increase the attenuation

slightly, and may result in a slightly different optimum impedance value.

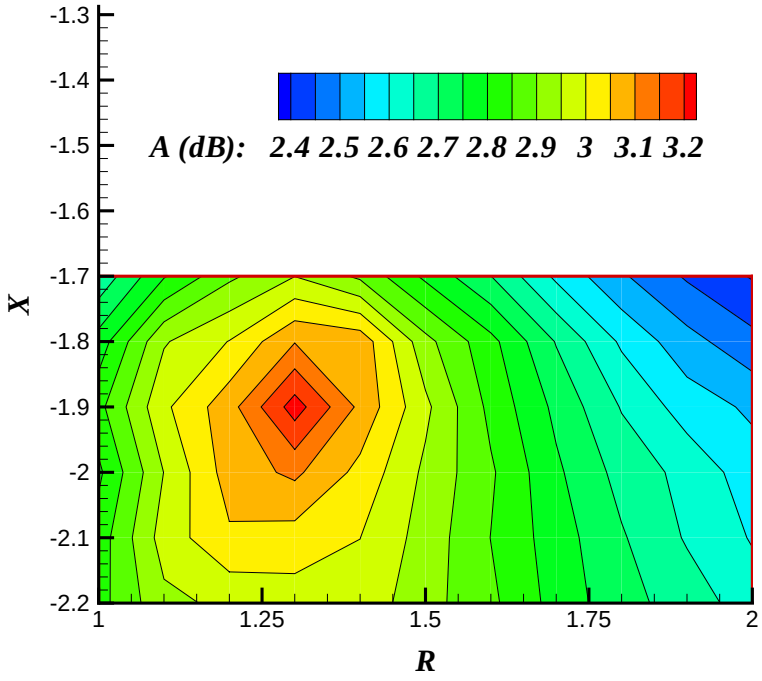

Figure 3.14: Attenuation contour map for the complete observe circle.

The effect of liner arrangement is now considered. The instantaneous acoustic pressure contours for four different cases (hard wall, slat lined, main element lined and both slat and main element lined) are shown in Figures 3.16 to 3.19.

The liner positions are highlighted by the solid black lines in the figures. The characteristics of the acoustic field with and without the liners can be seen clearly.

Figures 3.20 to 3.24 show the farfield directivity for the different liner arrangements considered. In Figures 3.20 to 3.23 the complete directivity plot is shown, with the distance of the line from the origin at any angle being proportional to the integrated root mean square pressure that radiates in that direction and the x-direction in Figure 3.13 is defined as $\theta = 0$ degree with the angle increasing anti-clockwise. In Figure 3.24 the important angles radiating through the slat gap are shown as decibel level. In Figures 3.20 to 3.24 the solid line with the square symbol represents the directivity of hard wall case; there are large radiation peaks in the upward direction and smaller peaks in the forward direction as well as the downward direction through the slat gap. As might be expected, the presence of the main element blocks downstream radiated noise. It should be noted however that the details of this radiated sound field does not agree with the pressure field shown in Figure 3.10, where the predominant noise radiation is through the slat gap. This

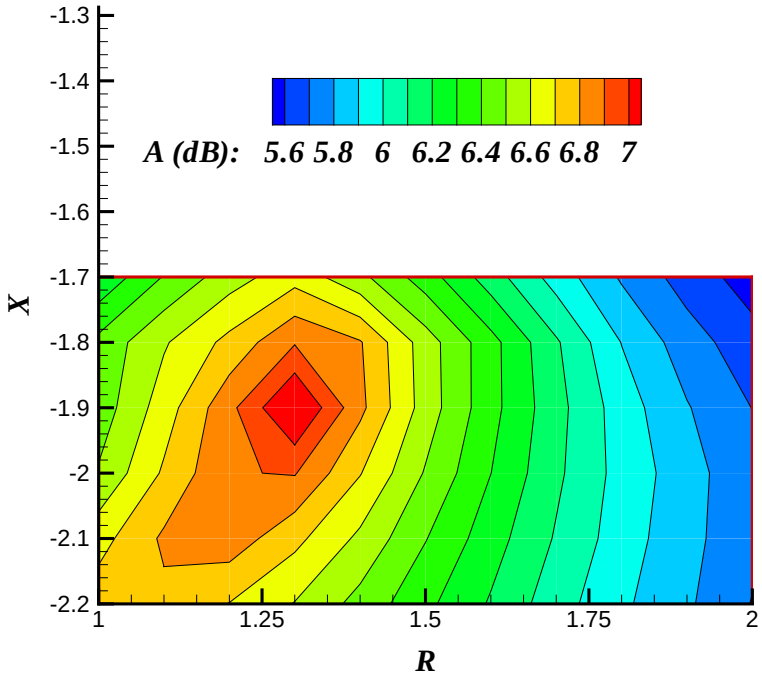

Figure 3.15: Attenuation contour map for the partial observe circle.

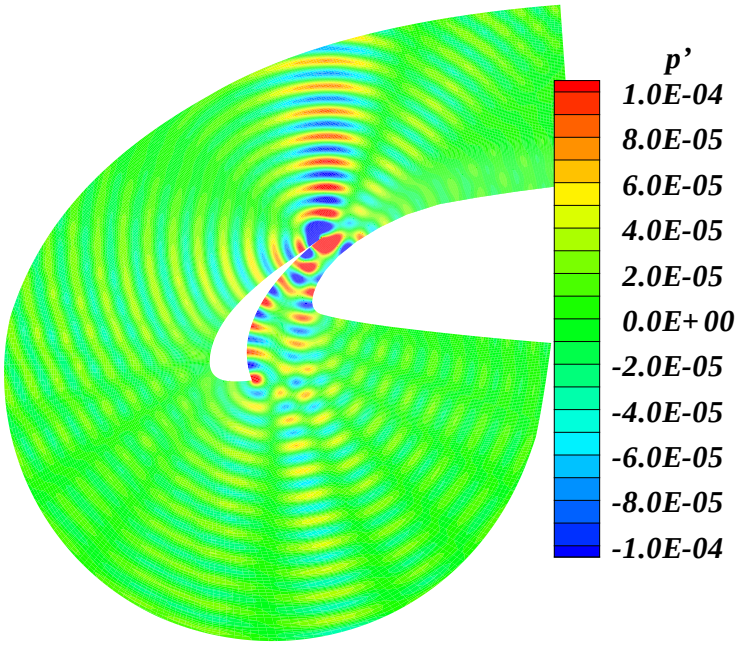

Figure 3.16: Contours of acoustic pressure for hard wall case.

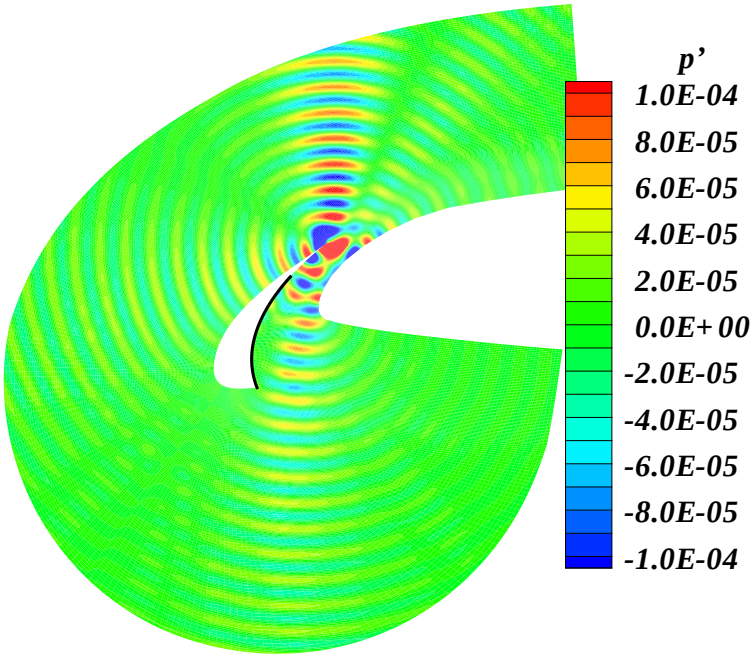

Figure 3.17: Contours of acoustic pressure for slat lined case.

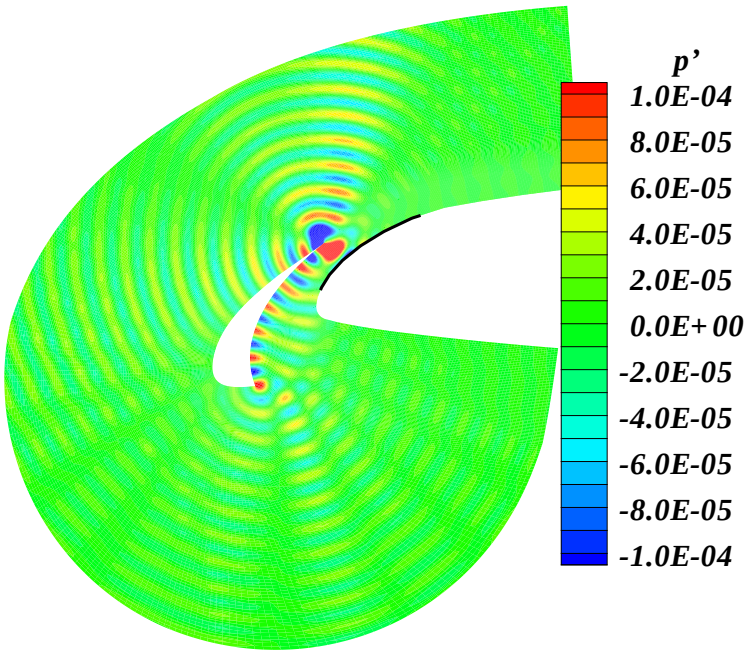

Figure 3.18: Contours of acoustic pressure for main element lined case.

suggests that the dipole source used in the acoustic predictions may not be fully representative of the actual aerodynamic source. The other lines in Figures 3.20

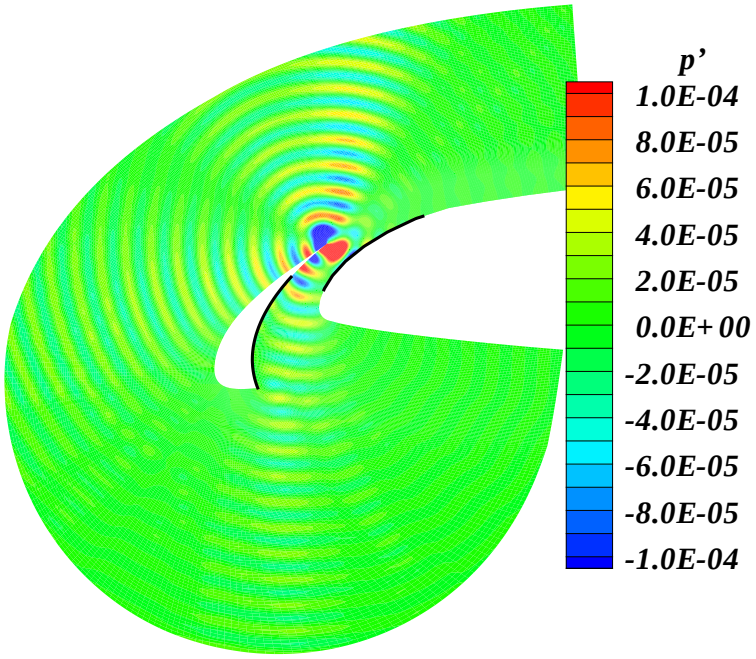

Figure 3.19: Contours of acoustic pressure for both slat and main element lined case.

to 3.24 show the directivity for the acoustically lined cases. In each case there is some effect in reducing noise radiation upwards although the effect in this direction is small for the slat cove liner. The liners produce little effect on the radiated noise in the upstream direction. As might be expected however, the main effect of the liners is a large reduction in noise radiation at angles from 240 degrees to 340 degrees where the sound has propagated through the slat gap. Generally there is good attenuation for radiation through the slat gap in the 240 degrees to 320 degrees range. The slat cove liner is predicted to cause a small increase in noise radiation in the 255 degrees to 275 degrees range. The combined effect of slat liner and main element liner gives the largest reduction. It should be noted that the combined liner arrangement enables a shift in the radiation peaks.

3.4 Aeroacoustic Simulation with Lined Wall Condition

3.4.1 Aeroacoustic Field Results

The linearized study, using an idealized source in a no-flow condition, is clearly an approximation to the true situation. Fully viscous flow simulations for the three-

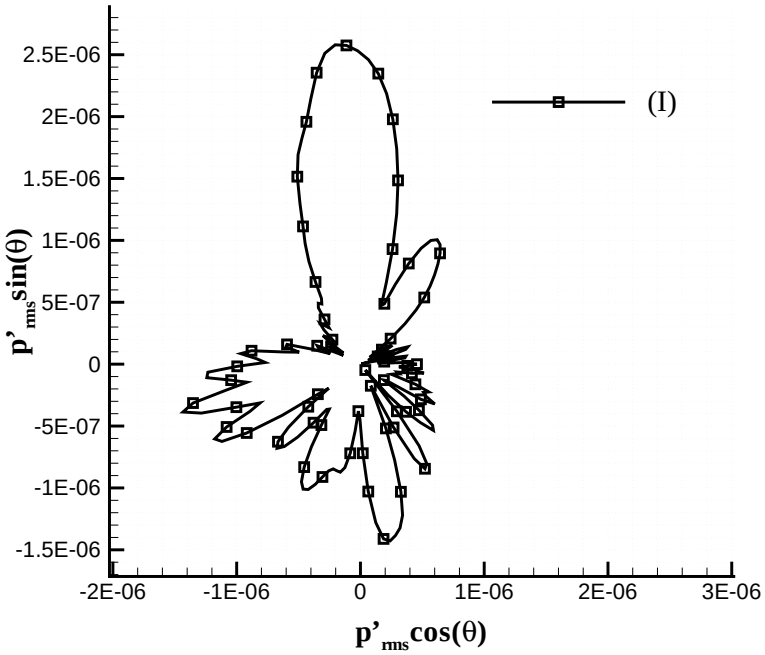

Figure 3.20: Directivity of acoustic signals for different liner arrangement: (I) hard wall.

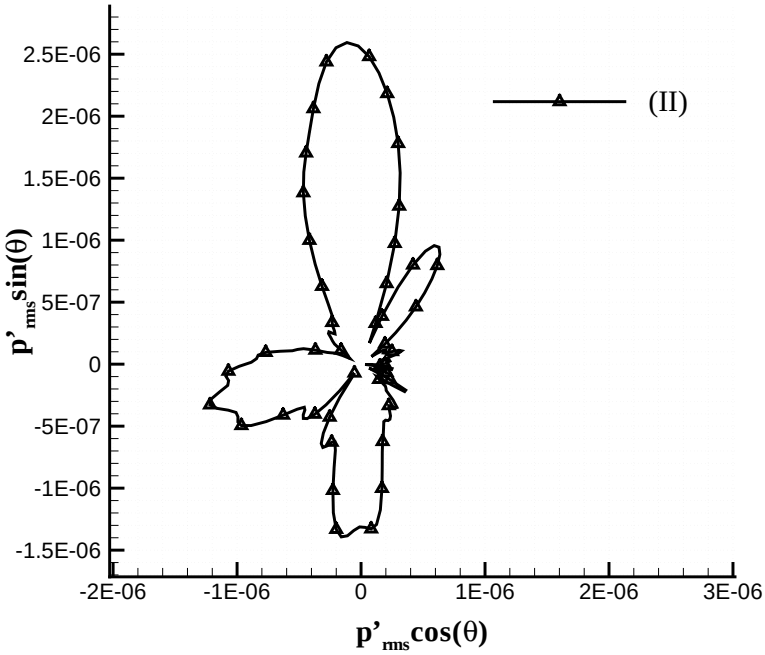

Figure 3.21: Directivity of acoustic signals for different liner arrangement: (II) slat lined.

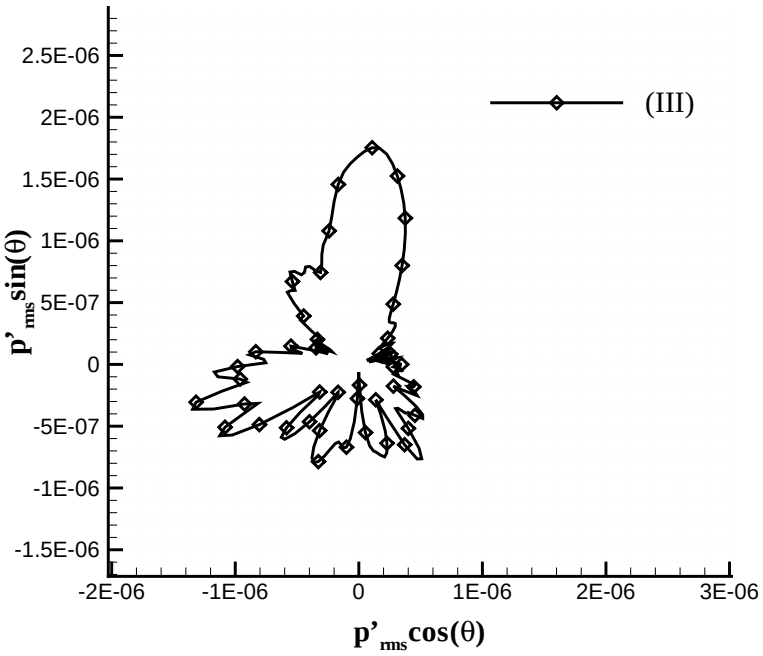

Figure 3.22: Directivity of acoustic signals for different liner arrangement: (III) main element lined.

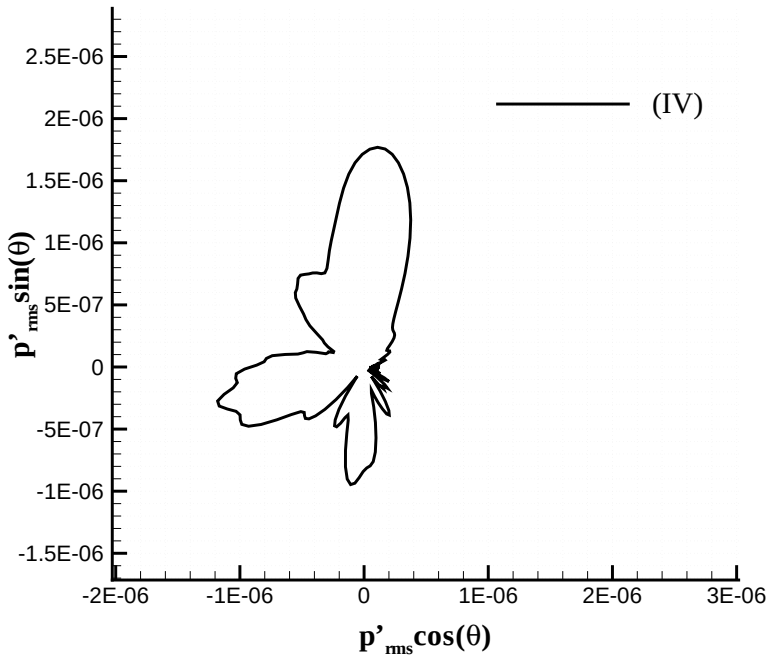

Figure 3.23: Directivity of acoustic signals for different liner arrangement: (IV) both slat and main element lined.

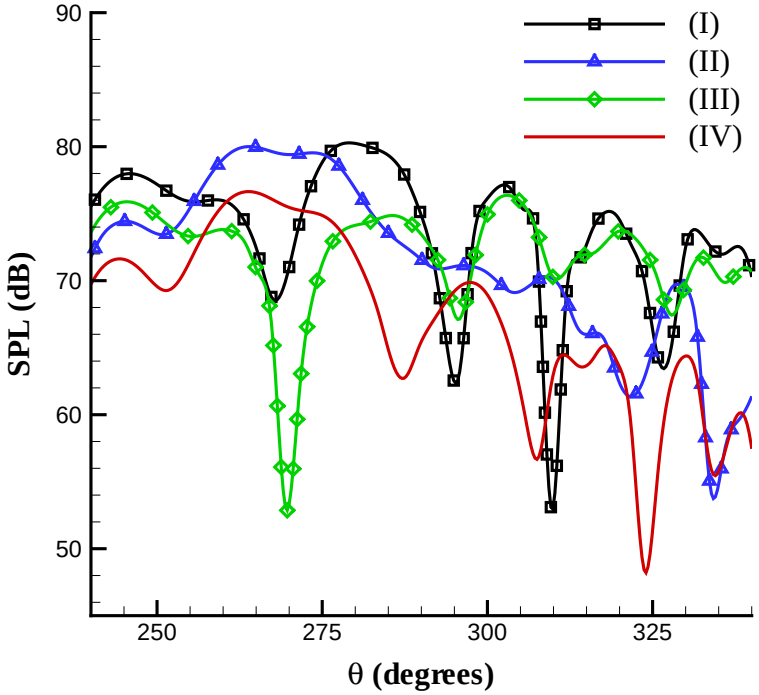

Figure 3.24: Directivity of acoustic signals in range of 240 degrees to 340 degrees for different liner arrangement: (I) hard wall, (II) slat lined, (III) main element lined, and (IV) both slat and main element lined.

element wing with the liner impedance boundary condition are also performed. The simulations employ the same free flow condition and the same high-lift device configuration as are used for the hard wall case computation (see Figure 3.2). The lined cases presented here are for a) the slat cove lined alone and b) for both the slat cove lined and the main element lined. The application of liners has an insignificant effect on the mean flow field. Figure 3.25 and Figure 3.26 show the instantaneous fluctuating pressures around the slat. The solid black lines indicate the positions where the liner acoustic treatment is applied. The optimized impedance value for the no-flow case is used, although it has already been noted that this may no longer be optimal for the with-flow situation. Compared with the result of hard wall case shown in Figure 3.10, both lined cases show significant attenuation of the sound field.

3.4.2 Comparison with Hard Wall Results

FW-H calculations are performed to obtain the far field directivity. Figure 3.27 illustrates the integration surface used for the FW-H calculation and Figure 3.28

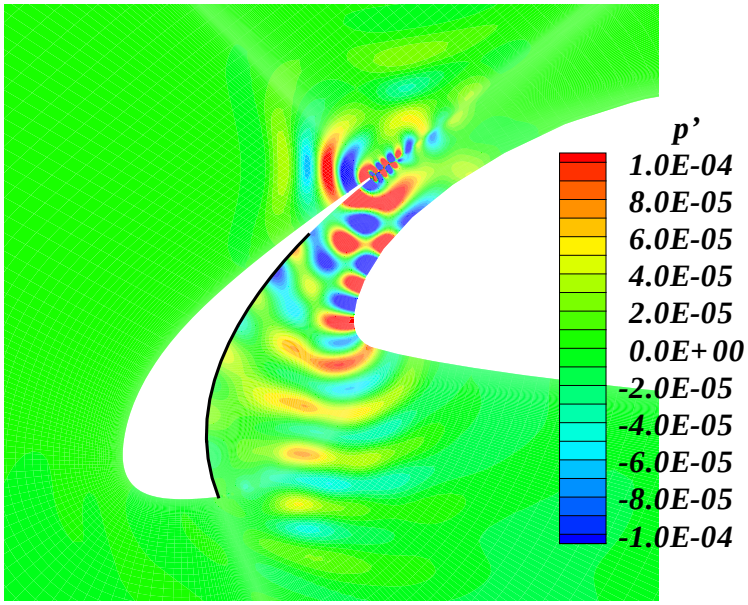

Figure 3.25: Fluctuating pressure field near the leading edge; liner on slat cove surface alone.

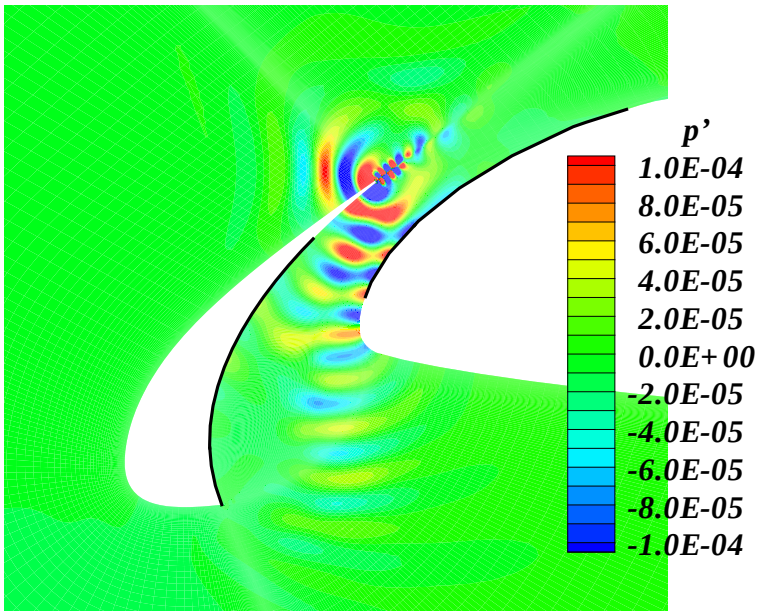

Figure 3.26: Fluctuating pressure field near the leading edge; liner on slat cove surface and main element.

shows the integration surface near the slat; the solid line corresponds to the wing surface and the dashed line corresponds to the integration surface. The position

of the integration surface must be handled with care to include all the major noise sources in the flow and it should be in the region where grid is fine enough to capture the acoustic signal without unacceptable dissipation. Previous research suggests that the contribution of volumetric sources to the total noise is non-negligible in high-lift simulations [93]. Therefore, it is insufficient to predict the far field noise solely by the integration of pressure on the solid surface. In the present calculation, the integration surface used is a permeable surface that includes all boundary layers and vortex shedding region. As the presence of liner has only insignificant effect on the mean flow, the FW-H results obtained using this integration surface can show the effect of liner on noise reduction. The observers are positioned at z=0 on a circle with the radius of 12.5 from the upper point of the trailing edge of the slat.

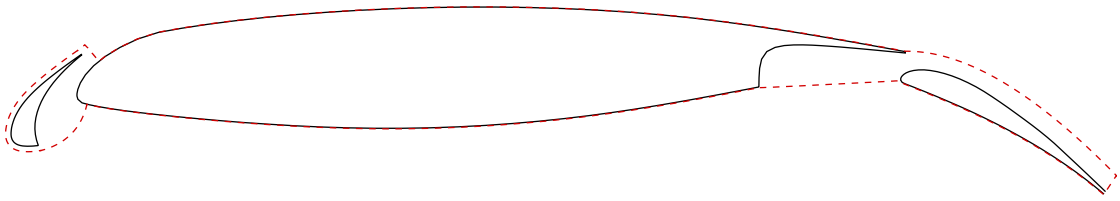

Figure 3.27: The integration surface used for FW-H calculations.

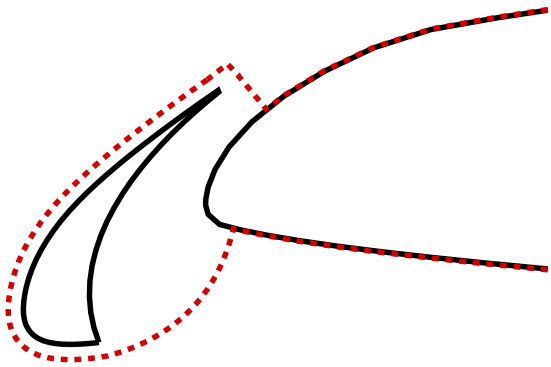

Figure 3.28: Zoomed view of the integration surface used for FW-H calculations.

The farfield directivity patterns are shown in Figures 3.29 and 3.30. In Figure 3.29 complete directivity patterns are shown. For the hard wall case; there are three peaks: upstream, upward and downward. The upward lobe is quite smaller than that of the LEE case. After the application of the acoustic liner the upward peak and downward peak are attenuated significantly while in the upstream direction the directivity pattern shows insignificant changes. The directivity patterns

in the angle range of 240 degrees to 340 degrees are shown in Figure 3.30. In this range the attenuation of the liner only on slat cove surface case is 1.6 dB and the attenuation of the liner on slat cove and main element case is 4.1 dB. This indicates that the liner on main element has made an important contribution to the total attenuation.

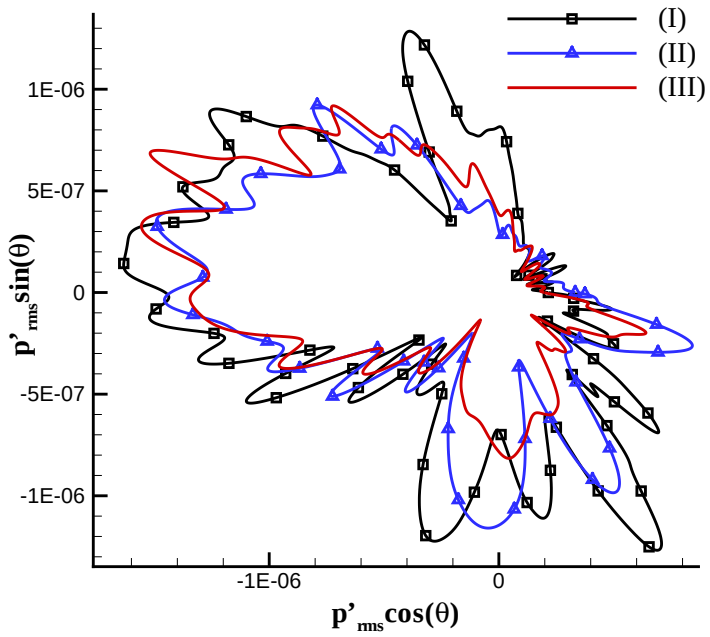

Figure 3.29: Directivity of acoustic signals for different liner arrangement: (I) hard wall, (II) slat lined, and (III) slat and main element lined.

3.5 Summary

In this chapter, the concept of attenuating radiated slat noise using acoustic liners in the slat gap has been explored using a variety of numerical simulation methods. The computation of the fully turbulent flow field of the high-lift wing model, which is simulated using the high-order code SotonCAA, shows the expected vortex shedding from the blunt trailing edge and associated high-frequency tonal noise. An exercise has been conducted on a range of liner impedance values by solving the linearized Euler equations for a modeled acoustic source located at the trailing edge of the slat to find a optimized one. Using the optimized impedance value, URANS computations for the wing with liner treatment are conducted. The results show that liners on the slat and main element provide useful attenuation of the slat trailing edge tonal noise.

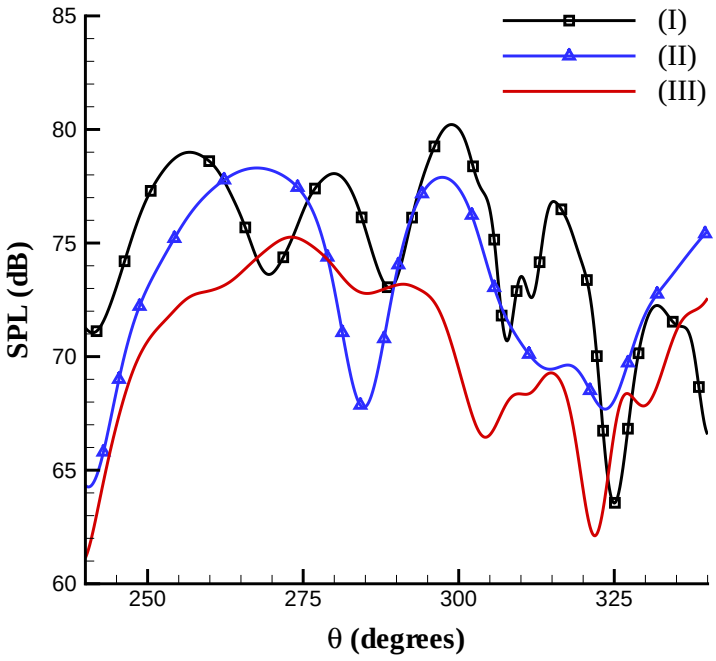

Figure 3.30: Directivity of acoustic signals in 240 degrees to 340 degrees for different liner arrangement: (I) hard wall, (II) slat lined, and (III) slat and main element lined.

Chapter 4

2D Slat Broadband Noise Simulations

4.1 Introduction

As stated in the previous chapter, the spectrum of the slat noise could contain the tonal components and broadband components. The results in the last chapter show that the acoustic liners treatment on the slat/main element gap could effectively attenuate the slat tonal noise. The work in this chapter and the following chapter attempt to find a good method to simulate the broadband slat noise and then to investigate the broadband slat noise attenuation ability of acoustic liner treatment on the slat/main element gap.

An accurate method to simulate the broadband noise is to perform DNS or LES [94, 26, 34]. In a typical approach, either DNS or LES is performed to evaluate the aerodynamic source terms. Then the modified LEE are solved to simulate the radiation of the noise. This type of method contains more physics, However DNS and LES are restricted by computational resources and not feasible for optimization or design process.

Another way to predict the broadband noise is the pseudo-laminar zonal method proposed by Khorrami *et al.* [50]. In this method, based on the knowledge that the flow in the slat cove region is in low velocity and behaves in a quasi-laminar manner, the slat cove region is treated as the laminar zone while other parts of the flow are treated as the fully turbulent region in 2D simulations. The numerical results were compared with the experiment data [95] and 3D numerical results [52] and revealed that the pseudo-laminar zonal method gives good agreement in term of broadband noise spectrum. Due to the perfect correlation assumption of the 2D simulation and

the over predicted vorticity dynamic in the slat cove region the amplitude of noise calculated using this method is larger than the experiment results [50].

Recently a frequency domain method was developed to predict the broadband slat noise [96]. In this method the broadband noise emanating from the slat cove region is predicted using a two-step process. First the noise sources are modeled based on amplitude, length, and time scales obtained from a RANS calculated turbulence field and at least one experimental measurement of the noise spectrum. Then the sound from these sources is propagated by the convected wave equation. A Green's function for convected wave equation is derived to take into account the scattering effects of the high lift wing in the presence of a uniform mean flow. Once the Green's function and noise source terms are known, the final noise prediction is obtained by forming a convolution of Green's function with modeled noise sources.

A low cost broadband noise prediction method is the SNGR approach [97]. The advantage of this method is that only the steady RANS calculation is needed in order to obtain the broadband noise sources. After turbulent kinetic energy and turbulent dissipation rate are calculated by a RANS simulation the turbulent velocity can be realized by the sum of random Fourier modes. Then the broadband noise sources calculated from the turbulent velocity field are used as the source terms in linearized Euler equation to simulate the acoustic field. Although the accuracy of this method is still an open question, the applications of SNGR approach to the jet flow and trailing edge noise predictions [98, 99, 28] show that it's a good tool to perform parameter studies.

In this chapter the acoustic field of the high-lift wing model with deployed slat and flap is investigated. The broadband noise is calculated by both the pseudo-laminar zonal method and the SNGR method. In the pseudo-laminar zonal method, the time accuracy flow and the far field noise signals are solved using the FLUENT. In the SNGR approach broadband sources of noise are modeled using stochastic noise generation method [28] from a numerical solution of the RANS equations with a $\kappa-\omega$ closure and the acoustic field is calculated using the SotonLEE by solving the APE [82]. The broadband noise attenuation effect of the acoustic liner treatment is studied by applying the broadband time domain impedance boundary condition [68] to the SNGR simulated acoustic field. The farfield directivity is obtained through an integral surface solution of FW-H equation [85].

4.2 SNGR Methodology

4.2.1 Stochastic Generation of a Turbulent Velocity Field

In the SNGR approach the space-time stochastic turbulent velocity field is generated using the stochastic method in which the random velocity field is realized by a finite sum of discrete Fourier modes based upon averaged data of the flow field [28]. The isotropic turbulent field is defined as:

$$\mathbf{u}_t(\mathbf{x},t) = 2\sum_{n=1}^{N} \hat{u}_n \cos[\mathbf{k}_n \cdot (\mathbf{x} - t\mathbf{u}_c) + \psi_n + \omega_n t]\sigma_n \tag{4.1}$$

where $\hat{u}_n$,ψ_n and σ_n are the amplitude, phase and direction vectors of the n^{th} Fourier mode, $\mathbf{u}_t$ is the turbulent velocity vector, $\mathbf{u}_c$ is the local convection velocity vector, $\mathbf{x}$ is the spatial vector, t is time and ω_n is the angular frequency of the n^{th} mode. $\hat{u}_n$ is determined by averaged turbulence information; ψ_n and ω_n are randomly selected. Assuming incompressibility, the wave vector $\mathbf{k}_n$ and the spatial direction of the turbulent field σ_n of the n^{th} mode are perpendicular:

$$\mathbf{k}_n \cdot \sigma_n = 0. \tag{4.2}$$

The amplitude $\hat{u}_n$ of each mode is determined from a modified Von Karman spectrum to simulate the complete spectral range:

$$\hat{u}_n = \sqrt{E(k_n)\Delta k_n}, \tag{4.3}$$

$$E(k) = 1.453\frac{2\kappa/3}{k_e}\frac{(k/k_e)^4}{[1+(k/k_e)^2]^{17/6}}\exp[-2(\frac{k}{k_\nu})^2] \tag{4.4}$$

where $k_e = \frac{1.37C_\mu\omega}{\sqrt{\kappa}}$ as suggested in Ref. [100], $k_\nu = (\frac{C_\mu\kappa\omega}{\nu^3})^{1/4}$ is the Kolmogorov wave number, κ is turbulent kinetic energy, ν is kinematic viscosity and C_μ=0.09 is the turbulence model constant.

As a test case the stochastic realization of isotropic turbulence has been considered. Figure 4.1 shows a realization of the spatial distribution of the simulated turbulent field at $t = 0$ with $N = 100$ modes.

The analytical expression of the Karman-Howarth longitudinal correlation function for an isotropic turbulence can be written as:

$$R_{11}(x) = \frac{3}{\kappa}\int_0^\infty (\frac{\sin(kx)}{k^3x^3} - \frac{\cos(kx)}{k^2x^2})E(k)dk \tag{4.5}$$

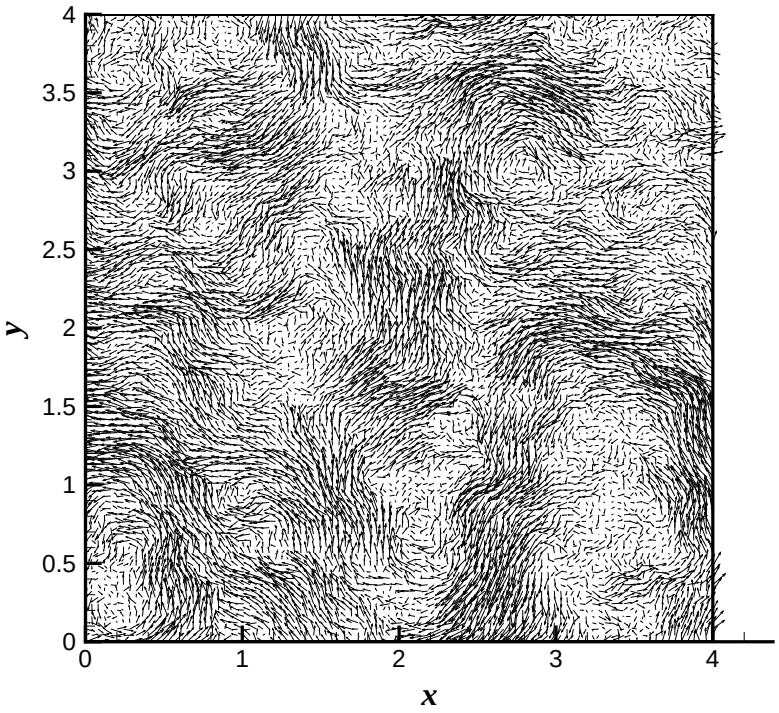

Figure 4.1: Spatial distribution of the simulated turbulent velocity field at t=0 with N=100 modes, κ=900 m^{2}s^{-2} and ω=18518.5 s^{-1}.

and the simulated and exact solutions of the correlation function are displayed in Figure 4.2.

4.2.2 APE Based Acoustic Analogy

After the generation of the velocity field, the next step is to get the noise sources from the velocity field. The acoustic perturbation equations (APE) proposed in Ref. [82] are adopted here:

$$\begin{aligned} &\frac{\partial \rho'}{\partial t} + \nabla \cdot (\rho_0 \mathbf{u}' + \mathbf{u}_0 \rho') = 0 \\ &\frac{\partial \mathbf{u}'}{\partial t} + \nabla(\mathbf{u}_0 \cdot \mathbf{u}') + \nabla(\frac{p'}{\overline{\rho}}) = \mathbf{q_m} \end{aligned} \tag{4.6}$$

where ρ is density, p is pressure and $\mathbf{u}$ is the velocity vector. Subscript $()_0$ denotes time averaged mean value and prime sign denotes the perturbation value. Based on the definition of the APE-4 system of Ref. [82], the $\mathbf{q_m}$ is the source term vector and can be written as:

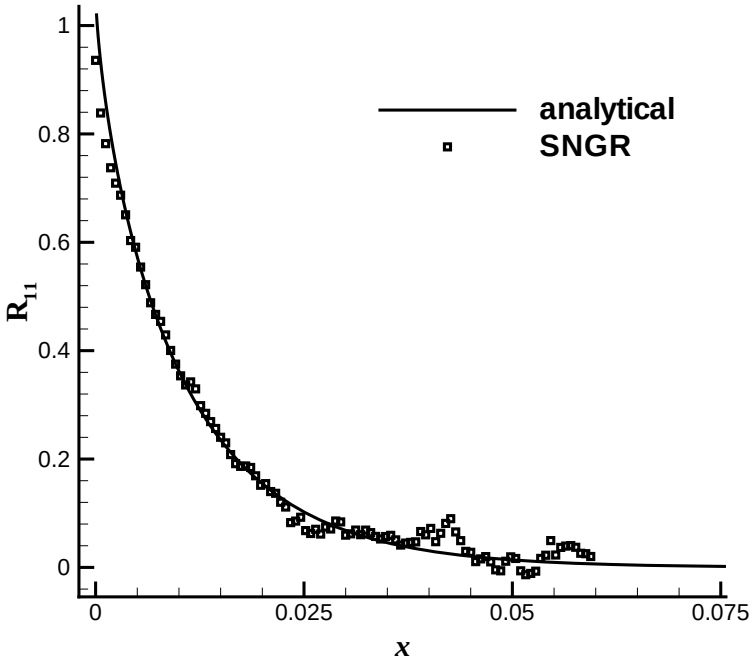

Figure 4.2: Comparison of the simulated and analytical correlation functions at t=0 with N=100 modes, κ=900 m^{2}s^{-2} and ω=18518.5 s^{-1}.

$$\mathbf{q_m} = -(\omega_\mathbf{t} \times \mathbf{u_t})' \tag{4.7}$$

where $\omega_\mathbf{t} = \nabla \times \mathbf{u}_t$ and $\mathbf{u}_t$ is the turbulent velocity modeled using the stochastic method.

The sound field of a spinning vortex pair is considered to validate the capability of the APE formulation for the acoustic prediction based on prescribed sources. The co-rotating vortex pair consists of two point vortices which are separated by a constant distance and the flow field induced by them is assumed inviscid and incompressible. The inherent unsteadiness of the spinning vortices flow field generates sound.

The half distance between the vortex centers is denoted r_0 and the circulation is Γ. The period of the two point vortices rotate around each other is $T_{pd} = 8\pi^2 r_0^2/\Gamma$. Each vortex induces on the other a velocity $v_\theta = \Gamma/4\pi r_0$ and the rotating Mach number is defined as $M_r = v_\theta/c_0 = \Gamma/(4\pi r_0 c_0) = 2\pi r_0/T_{pd}c_0$, where c_0 is the freestream sound speed. Figure 4.3 shows the flow configuration of the spinning vortex pair.

For this spinning vortex problem, the sound field has exact solutions [101, 102]. In Ref. [101] the sound field of the spinning vortex pair was derived using the method of matched asymptotic expansions (MAE) and the acoustic pressure fluctuation was

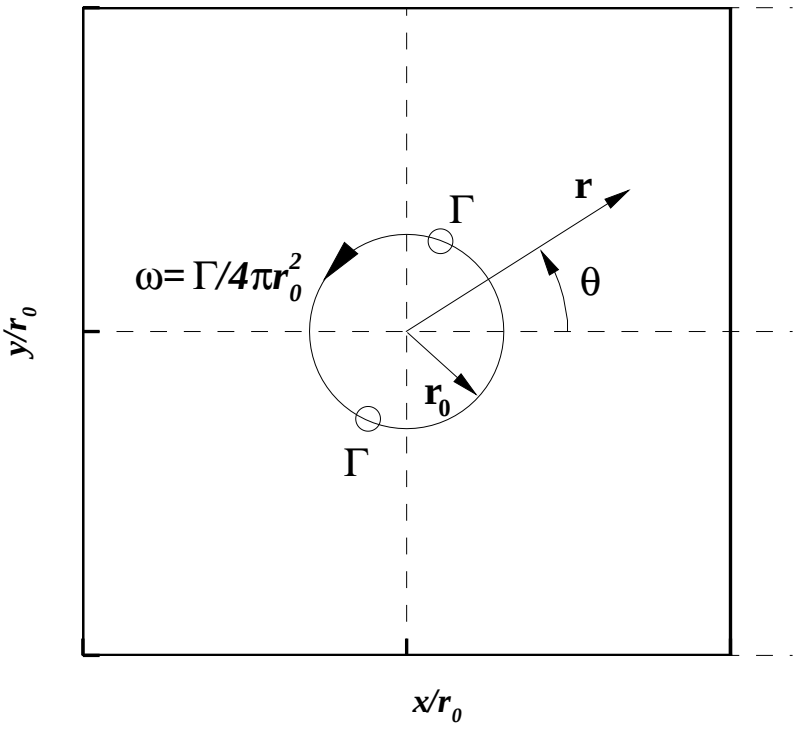

Figure 4.3: A sketch of the spinning vortex pair.

given by:

$$p' = p'_A[J_2(kr)\cos(\psi) - Y_2(kr)\sin(\psi)] \tag{4.8}$$

where $p'_A = \frac{\rho_0 \Gamma^4}{64\pi^3 r_0^4 c_0^2}$, $re^{i\theta} = x + iy$, $\omega = \Gamma/4\pi r_0^2$, $\psi = 2(\omega t - \theta)$, $k = 2\omega/c_0$ and J_2, Y_2 are the second-order Bessel functions of the first and second kind, respectively.

Numerical simulation of the acoustic field generated by the spinning vortex and comparison with the exact solution were given by Lee et al. [103] and Ekaterinaris [104, 105, 106] . It was reported [105] that the convergence can not obtained using the acoustic/viscous splitting technique proposed by Hardin and Pope [107] if the grid points are placed within half separation distance as the acoustic pressure becomes singular at the origin and the hydrodynamic velocities and pressure have large gradients close to the vortex centers.

In this case, APE-4 system of Ref. [82] is used. The point-like vortices are approximated using a vortex core model [82] and a Gaussian vorticity distribution with a standard deviation $\sigma_G \approx r_0$ is used in the model. The source terms in the APE can be written as:

$$\mathbf{q}_m(\mathbf{r},t) = -\frac{\Gamma^2 \mathbf{e}_r(t)}{8\pi^2 \sigma_G^2 r_0} \sum_{i=1}^{2} (-1)^i \exp(-\frac{|\mathbf{r} + (-1)^i \mathbf{r}_0(t)|^2}{2\sigma_G^2}), \sigma_G \approx r_0 \qquad (4.9)$$

where $\mathbf{r} = (x, y)^T$, $\mathbf{r}_0 = r_0 \mathbf{e}_r$, and $\mathbf{e}_r = (\cos \omega t, \sin \omega t)^T$.

The computational domain has an extension of $-200 \leqslant x/r_0 \leqslant 200$ in x-direction and $-200 \leqslant y/r_0 \leqslant 200$ in y-direction. The grid consists of 299×299 points with a surrounding buffer-zone size of 11 points. The grid points are clustered close to the origin to resolve the large gradients near it. The APE-4 system are solved using the SotonLEE with the optimized prefactored compact scheme [20] to evaluate the spatial derivative and the LDDRK optimized scheme [21] for the time integration. No convergency problem is found using the APE's source terms based on the Lamb vector.

In the following results of this case, the pressure is non-dimensionalized by $\rho_0 c_0^2$. Figures 4.4 and 4.5 show a good comparison of the acoustic pressure contours of the MAE solution and the solution of the APE-4 system.

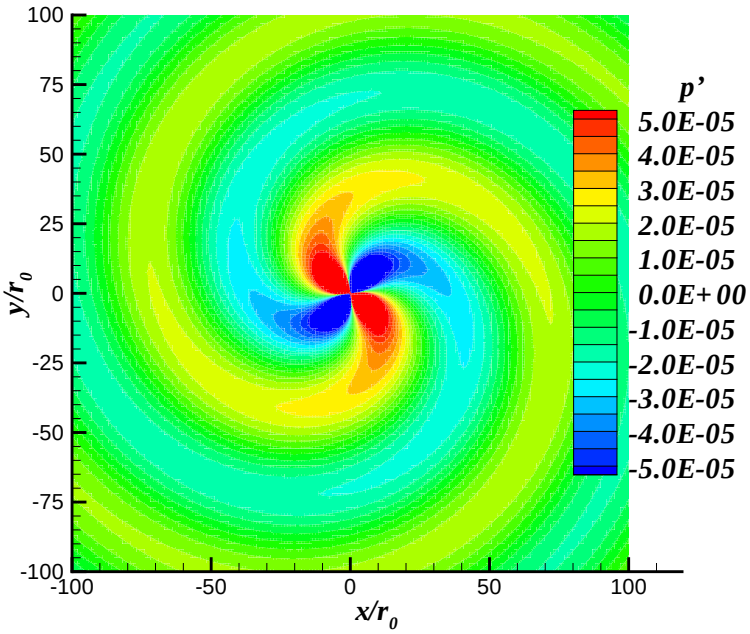

Figure 4.4: Instantaneous acoustic pressure contours for MAE solutions, Γ=$2\pi/10$ $\mathrm{m^2 s^{-1}}$, $M_r = 0.05$.

The time histories of the computed acoustic pressure and the analytical solution at ($50r_0$, 0) are shown in Figure 4.6. After the transient stage the acoustic pressure variation of APE-4 results is in good agreement with that of MAE . In Figure 4.7, the computed acoustic pressure along the x-axis (y=0) is compared with the analytical

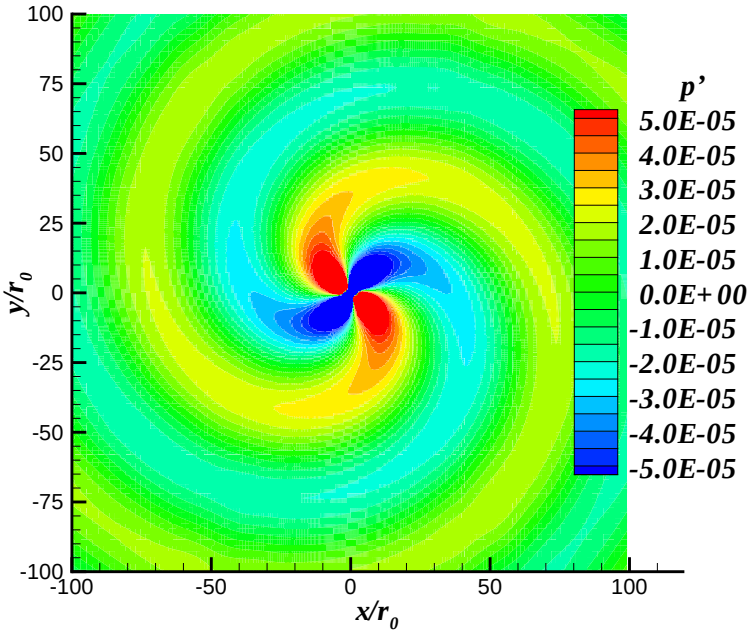

Figure 4.5: Instantaneous acoustic pressure contours of the numerical solution using APE-4, Γ=$2\pi/10$ m^{2}s^{-1} , $M_r = 0.05$.

solution. Near the origin of the computation domain, the acoustic pressure becomes singular and as a result of the acoustic pressure singularity, the APE-4 results show a discrepancy with the MAE results near the origin. However, for the location far away from the origin the results show a good agreement.

As a further test of the APE based acoustic analogy, the sound field of a circular cylinder at Mach number $M = 0.33$ and Reynolds number $Re = 150$ is calculated using the APE-4 system. The compressible flow is firstly calculated using the SotonCAA with the sixth-order compact scheme [19] to approximate the spatial derivatives and the eighth-order filter [73] to prevent the numerical instability. The the explicit LDDRK method [21] is adopted to advance the solution in time. The values in the following results of this case are shown in non-dimensionalized form and all the length scales are non-dimensionalized by D which is the diameter of the cylinder, velocities are non-dimensionalized by c^*_∞, density is non-dimensionalized by ρ^*_∞, pressure is non-dimensionalized by $\rho^*_\infty c^{*2}_\infty$. The grid consists of 297×500 grid points in the circumferential and the radial direction respectively and the calculation domain has a radial extension of 150 cylinder diameters. The calculated instantaneous pressure fluctuation field is shown in Figure 4.8.

The acoustic source terms $\omega \times \mathbf{u}$ are recorded after the calculation reaches the periodic stage. In this calculation, one time period of the vortex shedding, non-

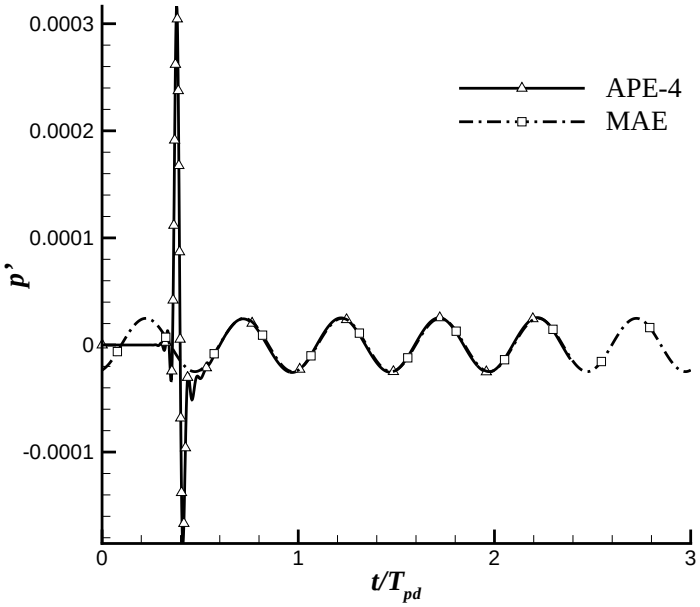

Figure 4.6: Comparison of the time history of the computed acoustic pressure (APE-4) and the analytical solutions (MAE) at ($50r_0$, 0), Γ=$2\pi/10$ $\mathrm{m^2 s^{-1}}$, $M_r = 0.05$.

dimensionalized with the cylinder diameter D and the freestream sound speed c^*_∞ is $T = 16.5$. The time period is split into 100 source time levels on which the source terms are recorded. The vorticity and the Lamb vector are shown in Figures 4.9 to 4.11.

The acoustic sources are then used to drive the APE and the solutions are given in Figure 4.12 which show good agreements with the directly calculated results in term of the far-field directivity and the acoustic signal amplitude. It should be noted that a discrepancy of the pressure fluctuation appears in the wake region of the cylinder due to the large mean flow gradients.

These cases reveal that the SNGR method is a useful tool for the noise field simulation and it is applied to the broadband slat noise study in the following section.

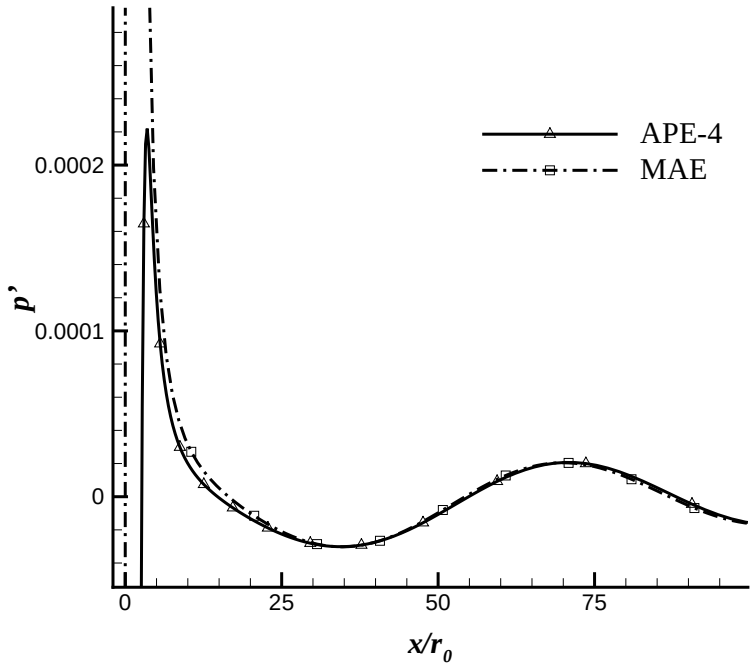

Figure 4.7: Comparison of the computed acoustic pressure (APE-4) and the analytical solutions (MAE) along the x-axis, Γ=$2\pi/10$ m^2s^{-1} , $M_r = 0.05$.

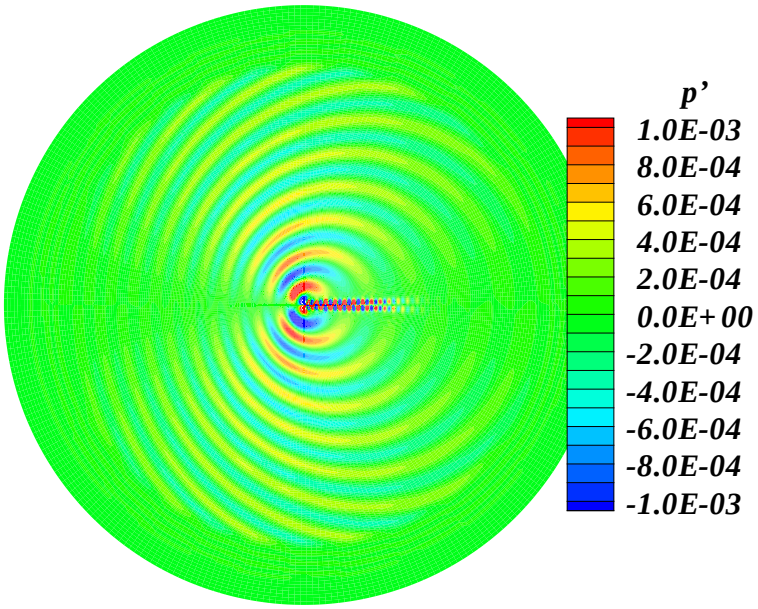

Figure 4.8: Instantaneous acoustic pressure field of a circular cylinder at M=0.33, Re=150 calculated by direct calculation.

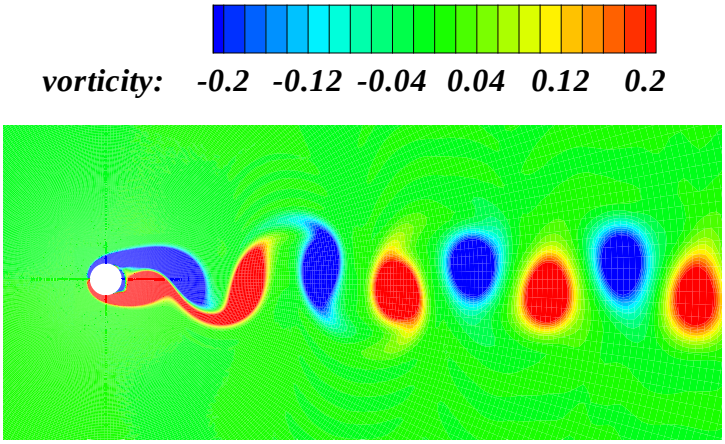

Figure 4.9: Directly calculated instantaneous vorticity field of a circular cylinder at M=0.33, Re=150.

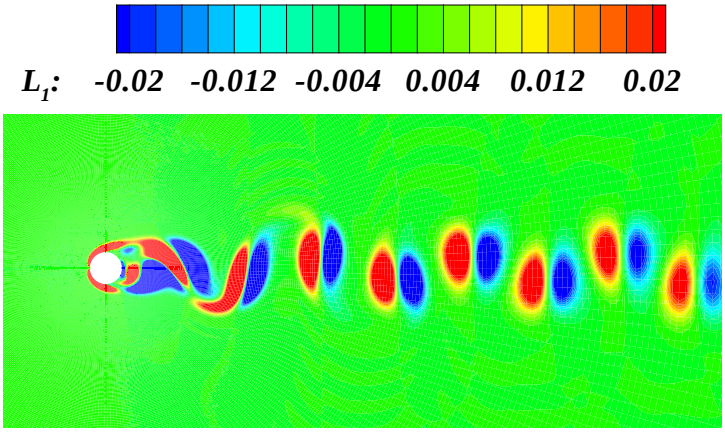

Figure 4.10: Instantaneous x component of the Lamb vector of a circular cylinder at M=0.33, Re=150.

4.3 Computational Results of Broadband Noise Attenuation

4.3.1 Computation Setup

As stated before, both the pseudo-laminar zonal method and the SNGR method are used to calculate the broadband slat noise field. The pseudo-laminar zonal

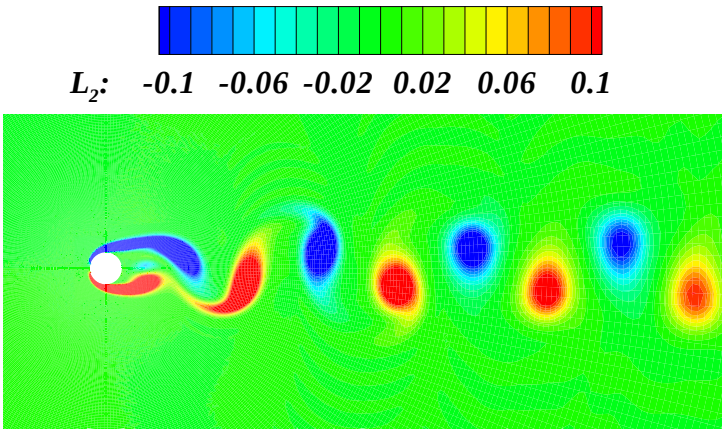

Figure 4.11: Instantaneous y component of the Lamb vector of a circular cylinder at M=0.33, Re=150

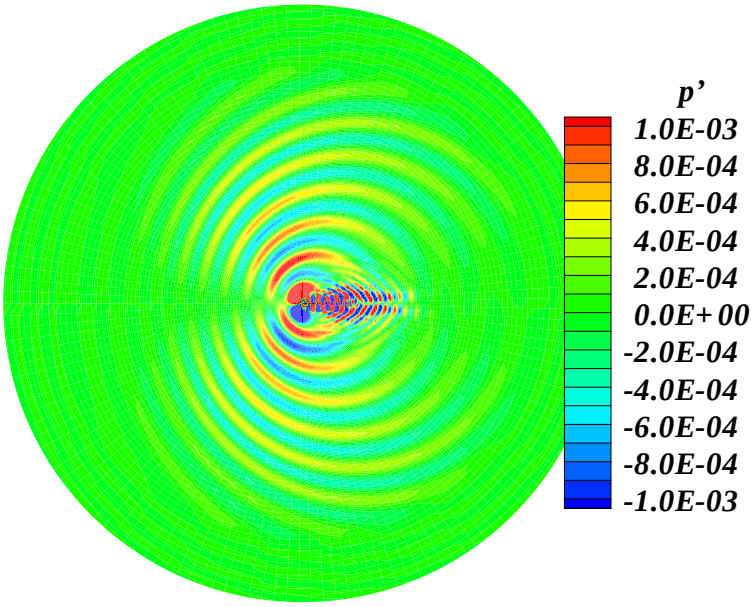

Figure 4.12: Instantaneous vorticity field of a circular cylinder at M=0.33, Re=150 calculated by the source driven APE-4.

calculation is performed using the FLUENT to solve the URANS equations with the two-equation SST $\kappa - \omega$ model to model the effect of turbulence and a region in the slat cove is set as laminar zone. The freestream flow condition, wing model geometry and grids distribution are same as what are used in aeroacoustic simulation

of the previous chapter. The laminar region is shown in Figure 4.13. The time step size used in the simulation is 1.0×10^{-5} s and a total of 20,000 steps are calculated. Based on sixteen 2.2 GHz AMD Opterons CPUs with 32 GB of RAM, 196 second CPU time per time step is needed.

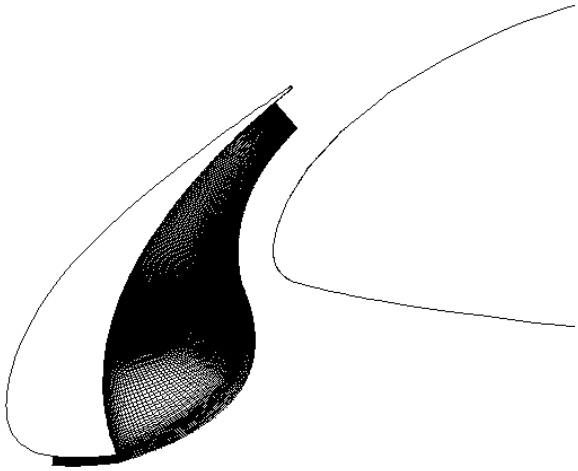

Figure 4.13: Black region shows the laminar zone used in the pseudo-laminar zonal approach.

In SNGR approach, the mean flow is obtained by a steady RANS calculation of FLUENT with two-equation SST $\kappa-\omega$ model on the same freestream flow condition, wing model geometry and grids distribution of the pseudo-laminar zonal method. Then the turbulent kinetic energy and turbulent dissipation rate are interpolated to a grid which is used for the noise propagation calculation. The interpolation is realized using TECPLOT's inverse-distance interpolation function with the options set as minimum distance 0, exponent parameter 3.5 and number of closest points which are selected by coordinate-system octants 13. The interpolated turbulent kinetic energy and turbulent dissipation rate are used to generate a turbulent velocity field using the stochastic method [97]. The broadband noise sources of APE-4 system can be calculated from the turbulent velocity field and the APE-4 are solved using the optimized prefactored compact scheme [20] to evaluate the spatial derivative and the 4-6 low dispersion and dissipation Runge-Kutta (LDDRK) optimized scheme [21] for the time integration. For the steady RANS calculation, a total of 97 hours are used for a total of 100,000 iterations on four 2.2 GHz AMD Opterons CPUs with 8 GB of RAM. For the noise propagation calculation, the time step size used is $1.0 \times 10^{-4} * C^* / c^*_\infty$ where C^* is the chord of the wing model and c^*_∞ is the freestream sound speed. A total of 400,000 steps are calculated for the hard wall case and a total of 100,000 steps are calculated for the lined wall cases. Based on a 3.0 GHz

Intel XEON CPU with 2 GB of RAM, 1.0 second CPU time per time step is required.

The computational grid used for the acoustic calculation is shown in Figure 4.14. For reason of simplicity, the geometry contains the slat and part of the main element only. A total of 81,492 grid points are used and the maximum grid size is 12.5×10^{-3}, which gives an equivalent grid resolution of 7 PPW for a wave frequency up to 12. The liner condition is applied to the slat cove surface and part of main element surface as shown in previous chapter. The slat cove liner starts from the cusp of the slat, but at the slat trailing edge the available depth is too small to apply a practical liner, the liner treatment is thus only extended to a position where at least 12.5×10^{-3} depth is available. The liner covers 56% of the total slat cove surface length. On the basis that the acoustic liner on the main element should avoid the leading edge stagnation point, so as to minimize any possible aerodynamic penalty, the liner is started from a position on the suction surface at a distance of 0.01 from the leading edge and is extended for a distance which will be covered by slat when the slat was retracted.

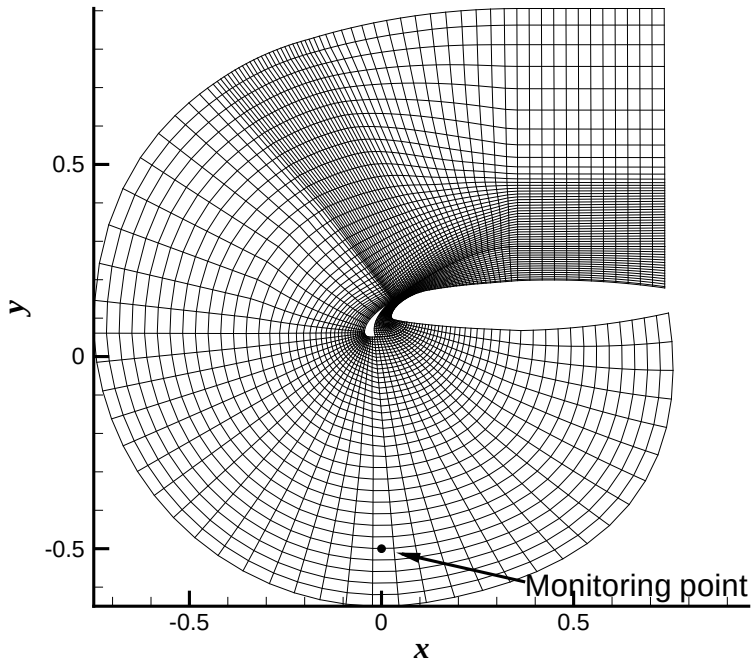

Figure 4.14: Grid distribution for the acoustic calculations solving APE-4 (every 4th grid is shown).

4.3.2 Computational Results and Liner Performance

In this section, the results of the SNGR method and the pseudo-laminar zonal approach are presented. Although it is claimed that the APE-4 system is stable for arbitrary mean flow [82], the noise radiation calculation with the mean flow of the high-lift configuration shows instability due to the strong shear layer near the slat trailing edge. All the APE-4 system results shown in this section are obtained without mean flow effect. The acoustic directivity obtained using the pseudo-laminar zonal approach and the SNGR method are compared and the broadband noise attenuation effect of the acoustic liner treatment is studied by applying the broadband time domain impedance boundary condition to the SNGR generated acoustic field. The farfield directivity is obtained through an integral surface solution of FW-H equations.

Unless indicated otherwise, all values in the followings of this section are shown in non-dimensionalized form and all the length scales are non-dimensionalized by $C^* = 0.8$ m which is the chord length of the wing without the slat and flap deployed, velocities are non-dimensionalized by $c^*_\infty = 340$ m/s, density is non-dimensionalized by $\rho^*_\infty = 1.225$ kg/m^3, pressure is non-dimensionalized by $\rho^*_\infty c^{*2}_\infty$.

4.3.2.1 Computational Results

In the SNGR method, the RANS calculated turbulent kinetic energy and turbulent dissipation rate are interpolated from the RANS grid to the APE grid to generate the turbulent velocity field. Figure 4.15 show the interpolated turbulence kinetic energy distribution. The kinetic energy contours reveal that the unsteadiness is concentrate in the slat cove region and has higher values near the reattachment point.

To generate the stochastic noise source, a zone within which the turbulence kinetic energy is larger than $0.3\kappa_{max}$ is defined as the source region, where κ_{max} is the maximum value of the turbulent kinetic energy. The abrupt termination of vorticity at the source region boundary will induce spurious noise as observed by Mankbadi et al [108]. To avoid the spurious noise, a damping zone of 5 grid points thickness is used and the stochastic generated turbulence x-direction velocity field is shown in Figure 4.16.

From the stochastic generated velocity, the source vector $\mathbf{q_m}$ in acoustic perturbation equations can be calculated and the acoustic field driven by these stochastic noise sources are simulated by solving the acoustic perturbation equations (Figure 4.17).

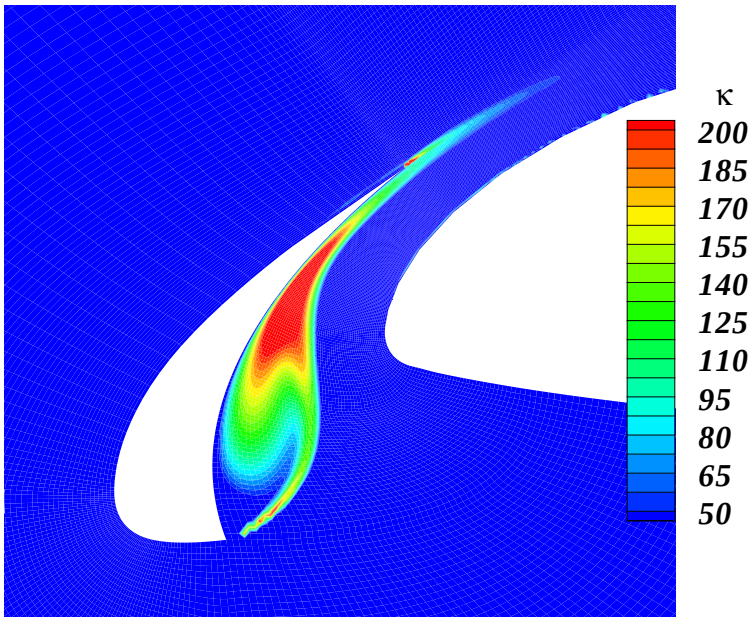

Figure 4.15: Interpolated turbulent kinetic energy distribution in the slat cove region.

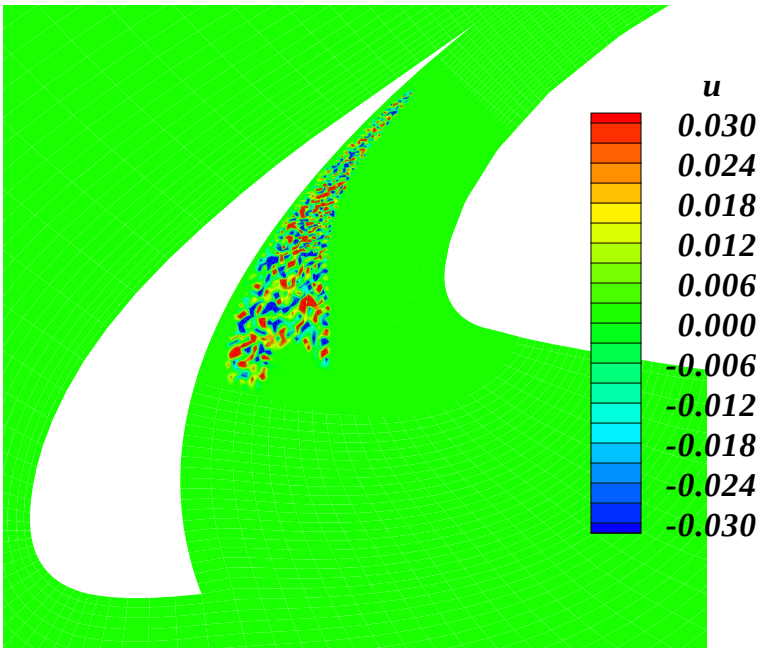

Figure 4.16: Stochastic generated x-direction velocity field near the slat cove region.

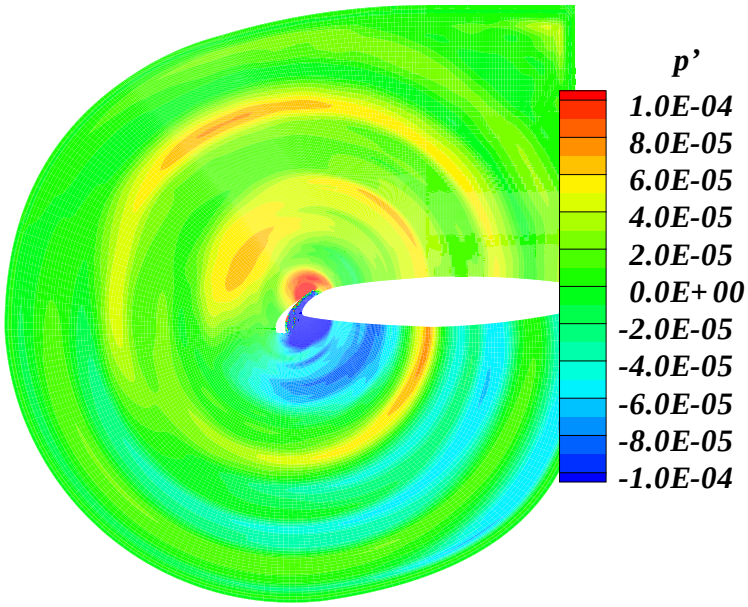

Figure 4.17: Acoustic field of the hard wall case with stochastic sources.

As a comparison the pressure fluctuating field of the wing is calculated using the pseudo-laminar zonal method proposed by Khorrami *et al.* [50]. The calculated pressure fluctuating field is shown in Figure 4.18. It should be noted that the amplitude of the pressure fluctuation of the zonal laminar method is significantly larger than that of the SNGR method. The spectrum of the acoustic pressure at a monitoring point located at $x = 0.2, y = -0.5$ as shown in 4.14 is calculated by Fourier transforming for the pressure history (Figure 4.19). The sampling rate is 1.0×10^3 and a total of 40,000 samples which are split into 10 blocks are used. The resulting frequency resolution is about 0.25. Both methods show broadband characteristics and SNGR results are about 10dB less than that of zonal laminar results at low frequency (less than 3.5). The SNGR result shows similar decay trend of SPL along the frequency to that of the previous experiment and computation [42, 96]. It was observed in Khorammi's work that zonal laminar method could overpredict the SPL of the noise up to 15 dB compared with the test results [50]. So the accuracy of the amplitude of the predicted noise is still an open question.

To compare the directivity predicted by the zonal laminar method and the SNGR method the far-field sound radiation is calculated by solving the FW-H equation. The integration surface for the zonal laminar method and the SNGR method are same as that used in the previous chapter. The integration surfaces are extruded in the spanwise direction with a span from -0.625 to 0.625. A total of 180 farfield

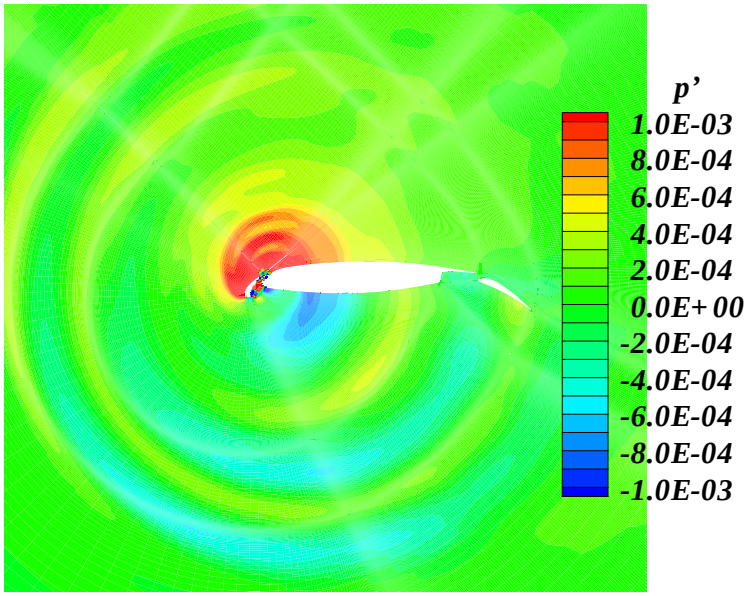

Figure 4.18: Pressure fluctuating field obtained using the pseudo-laminar zonal method.

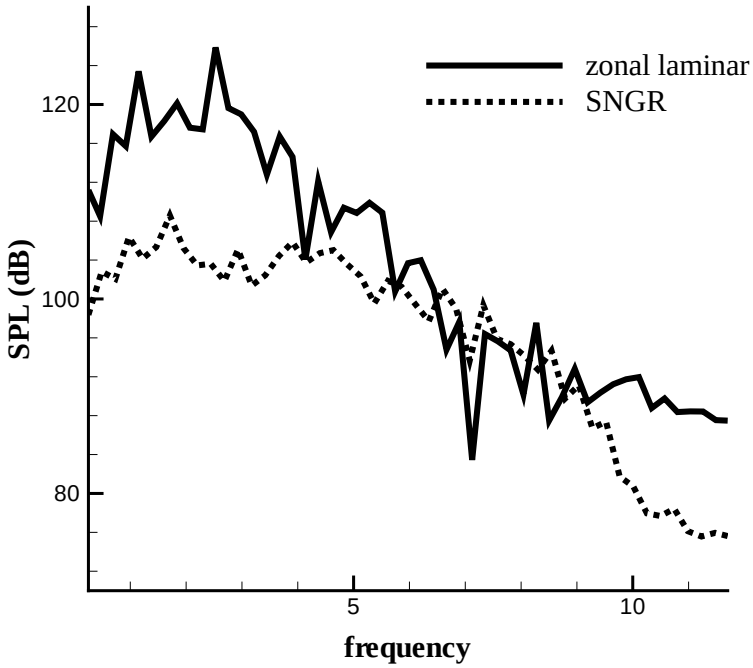

Figure 4.19: Comparison of the spectra of the monitored pressure.

observers are positioned on the z=0 plane on a circle with a radius of 12.5 from the trailing edge of the slat. The root mean square (RMS) pressures at the observer positions are plotted in Figure 4.20. To make the comparison of directivity clearer

the amplitude of SNGR results has been multiplied by a factor of 5. Both the SNGR results and the zonal laminar results show a dipole like directivity. It should be noted that for the SNGR case the downward lobe is larger than the upward one while the zonal laminar result is almost axisymmetric. As there is a broad similarity in spectra and directivities of both cases, it can be argued that the SNGR method can be used to investigate the liner attenuation effect if the difference of the noise level rather than the absolute value is interested.

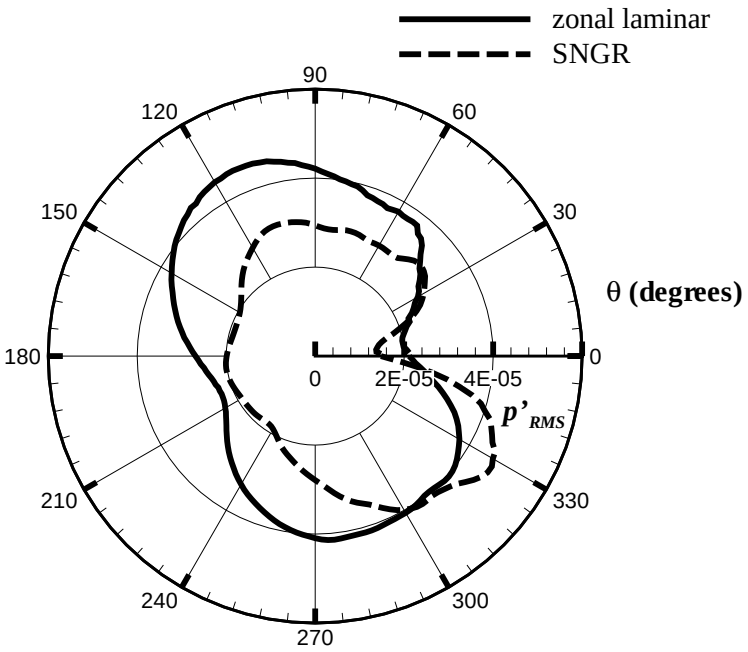

Figure 4.20: Comparison of the RMS value of the farfield pressure fluctuation of the zonal laminar method and that of the SNGR method.

4.3.2.2 Liner Performance

Having established that SNGR is useful for predicting the radiation of broadband noise from the slat, the method is used to examine the potential noise attenuation benefit of acoustic liners to absorb sound propagating within the slat-gap region of the high-lift wing. Two sets of liner arrangement are studied: 1) liner on the slat cove surface only and 2) liner on both the slat cove surface and on part of main element surface. The measured liner reactance value by Motsinger et al. [109] is used in the calculation and in order to achieve attenuation in a boarder frequency range, the liner resistance is chosen as 1.0. To model the liner impedance in the time domain impedance boundary condition, a three-parameter model is used which can

be written as:

$$Z(\omega) = R + iX = R + i(X_{-1}/\omega + X_1\omega) \tag{4.10}$$

where X_1 and X_{-1} are acoustic mass and stiffness used to fit the liner reactance value. Using this model if $X_1 > 0$ and $X_{-1} < 0$, then the impedance boundary would be stable. In the calculation, the X_1 is 0.0511 and X_{-1} is -39.627. The SNGR calculations with time domain impedance boundary condition are performed to assess the attenuation effect of acoustic liners for broadband noise. Figures 4.21 and 4.22 show the acoustic fields with the liner treatment.

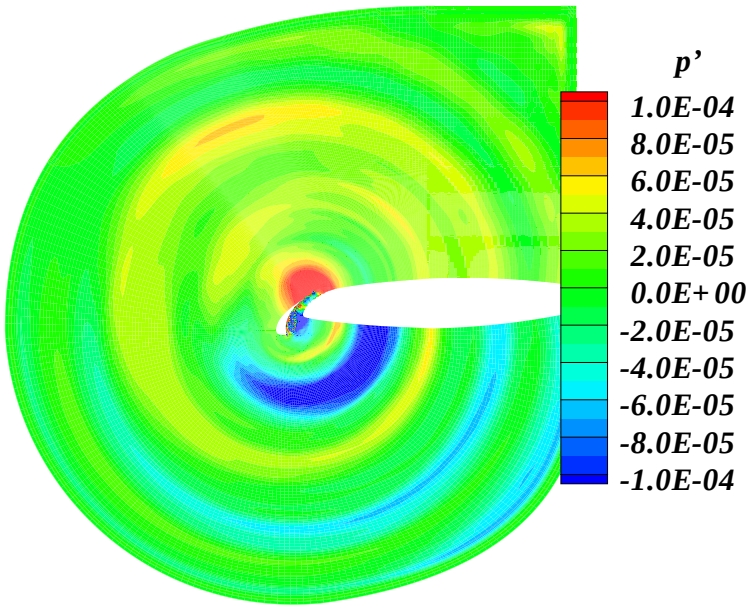

Figure 4.21: Acoustic fields driven by stochastic sources with liner treatment on slat cove only.

The farfield sound radiation is calculated by solving the FW-H equation as described before. In Figure 4.23 the complete directivity plot is shown, where the x-direction in Figure 4.14 is defined as 0 degree of the observer angle with the angle increasing anti-clockwise and the sound pressure lever at every angle is given as decibel level. In Figures 4.23 the solid line represents the directivity of hard wall case, the dashed line represents the directivity of slat lined case and the dashed-dot line represents the slat and main element both lined case. In each lined case there is some effect in reducing the noise. It should be noted that the stochastic generated broadband noise is concentrate near the slat trailing edge where the slat is not lined due to the small thickness of the slat. As a result, for the slat lined case the attenuation is relatively small. For the slat and main element both lined case, there

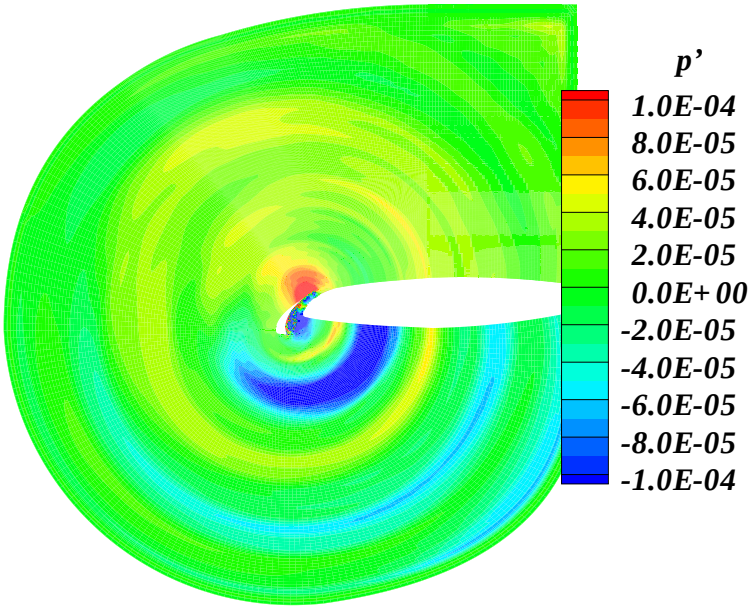

Figure 4.22: Acoustic fields driven by stochastic sources with liner treatment on slat cove and main element.

is a relatively large attenuation in the observer angle range from 40 degrees to 220 degrees because the liner on the main element attenuate the noise near the trailing edge significantly in the upward direction.

The FFT is performed for the acoustic pressure history obtained at each observer point and the sampling rate is 1.0×10^3 and a total of 8,500 samples which are split into 10 blocks are used. The resulting frequency resolution is about 1.2. The Figure 4.24 shows the attenuation of different cases in narrow band spectra calculated by averaging the values at different observers. The maximum attenuation for the slat lined case is 0.55 dB at the frequency of 4.7 and the maximum attenuation for the slat and main element both lined case is 2.3 dB at the frequency of 3.5. The overall attenuation obtained by averaging the attenuations at different frequencies is 0.25 dB for slat lined case and the overall attenuation for slat and main element both lined case is 1.15 dB.

4.4 Summary

The acoustic field generated by broadband noise sources on the slat of the high-lift wing model has been simulated using both the pseudo-laminar zonal method and the SNGR approach. The pseudo-laminar zonal method and the SNGR approach

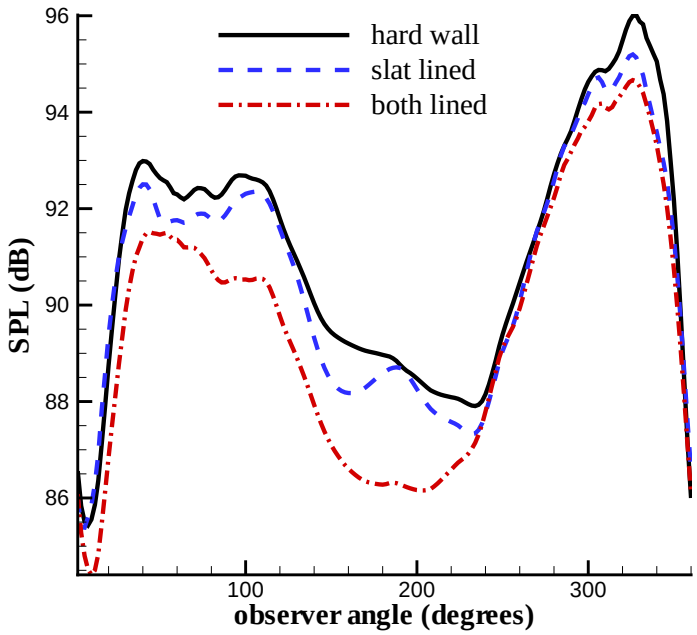

Figure 4.23: Directivity of the broadband acoustic signals for different liners arrangement.

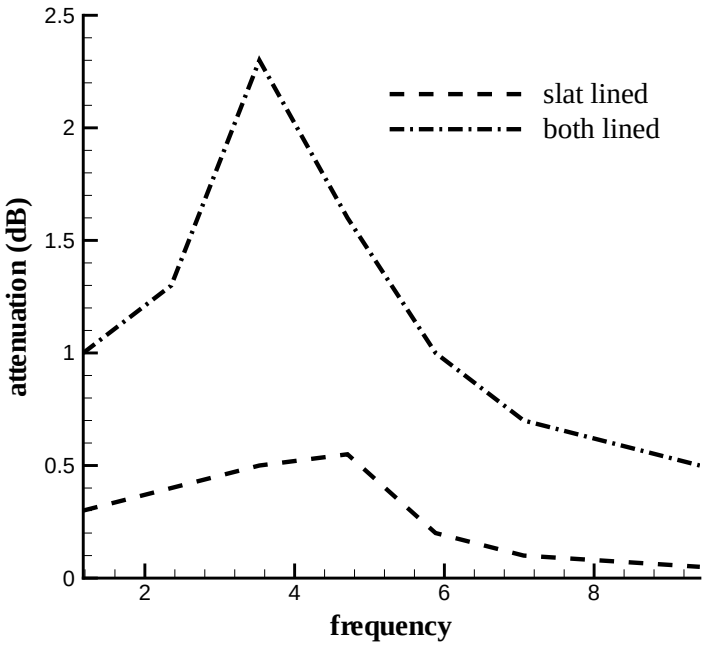

Figure 4.24: Comparison of the attenuation for the stochastic generated broadband slat noise in narrow band spectra.

both give a dipole-like far-field directivity and broadband spectra of the perturbation pressure. The CPU time used for the pseudo-laminar zonal method is about 1,000 hours based on sixteen 2.2 GHz AMD Opterons CPUs while the CPU time needed for the noise attenuation study using the SNGR method is 45 hours based on a 3.0 GHz Intel XEON CPU with 2 GB of RAM. The SNGR method has been shown to be a potentially useful method to model the generation of broadband slat noise and to investigate the noise attenuation potential of the slat gap acoustic liners, for which the interest is in changes of noise level rather than the absolute value. Predictions for a non-optimized acoustic liner show a moderate amount of attenuation.

Chapter 5

3D Slat Broadband Noise Simulations

5.1 Introduction

The generation of the broadband slat noise represent a complex aeroacoustic problem which involves the vortex generation from the slat cusp, vortex break down, merging in the slat cove shear layer and vortex distortion near the reattachment point [52]. To understand the physics and mechanisms behind these phenomena and to find a way to reduce the slat noise, accurate simulations, for example LES or DES, of the complex unsteadiness flow of the high-lift wing are needed.

In Ref. [51] a zonal-detached-eddy simulation of the flow around a high-lift configuration shows good agreement of the computed and measured mean flows. And the calculation captured the important unsteadiness in the slat cove such as rollup and formation of discrete vortices. In Ref. [52] a 3D simulation with the pseudo-laminar approach was performed and the computation was compared with the particle image velocimetry measurements. The results indicate that the broadband noise sources are driven by the significant turbulent fluctuations in the slat cove region.

Further to the 2D calculations of the previous chapters, the computational work of this chapter is to investigate the details of the unsteady flow of the high-lift configuration by 3D LES and to examine the liner performance by solving the APE with the acoustic sources obtained from LES. The work are divided into two parts: (1) a LES using high-order spatial scheme and implicit temporal integration is conducted for wing with slat deployed and the acoustic sources of slat noise are recorded; (2) slat noise reduction potential of the acoustic liners is investigated by solving the acoustic perturbation equations with the recorded acoustic sources in the slat cove

region.

5.2 Computation Setup

As introduced in Chapter 2, the wing model comprises a main element, a slat and a flap geometry. To save the number of grid points, the slat is in a deployed position and the flap is in the retracted position in the LES calculation. The model has a chord length C of 0.8 m without the slat and flap deployed and the slat chord is 12% of the overall chord length. The free stream Mach number is 0.2 and the main element angle of attack is 12 degrees, to match the 5 degrees angle of attack case in 2D simulations in which the flap was in deployed position.

The 3D grid is generated by uniformly extrude a basic 2D grid along the spanwise (z) direction and the periodic boundary condition is used in the spanwise direction. The basic 2D grid consists of 144 blocks with a total of 210,000 nodes and the total computational domain ranges from -10C to 10C in both x and y directions which are shown in Figure 5.1. The grids are designed to ensure $y^+ = O(1)$ along all solid walls and the boundary layers are resolved with a minimum of 30 mesh points. As recommended by Spalart [110], the grid size in z-direction Δ_z is chosen as $0.002C$ to have $\Delta_z \approx \Delta_x$ in the LES region and a total of 26 grid points are used in the spanwise direction yielding a spanwise domain range from 0 to $0.05C$ and a total of 5.46 million points. The grid near the slat cove region is shown in Figure 5.2.

The flow is calculated using the SotonCAA with the sixth-order compact scheme [19] to approximate the spatial derivatives. The implicit temporal integration solver is used and the computation is performed on a Linux cluster using 48 2.2GHz AMD Opterons CPUs. The CPU cost per subiteration is 9.8 s and the time step is fixed to $0.0001C/c_\infty$ with 5 Newton-like subiterations yielding a maximum CFL number based on acoustic velocity $(u_\infty + c_\infty)$ equals to 15. The time step corresponds to a sampling frequency of 4.25 MHz and the flow through time scale based on the slat chord and the free stream velocity corresponds to 6,000 time steps. After the transient stage, the calculation is run over 30 slat flow-through time units to ensure good mean and statistic results.

5.3 Computational Results of LES

In the LES calculation, both the vortex shedding from the slat trailing edge and the unsteady flow in the slat cove region are captured. In this section the results presented are focus on the the instantaneous and the averaged flows in the slat

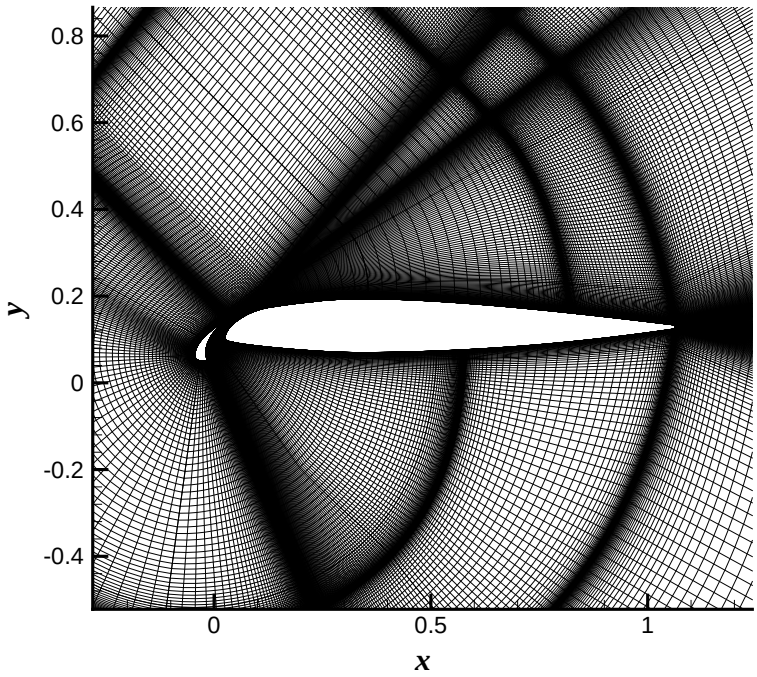

Figure 5.1: A view of the cross section grid for the high lift wing.

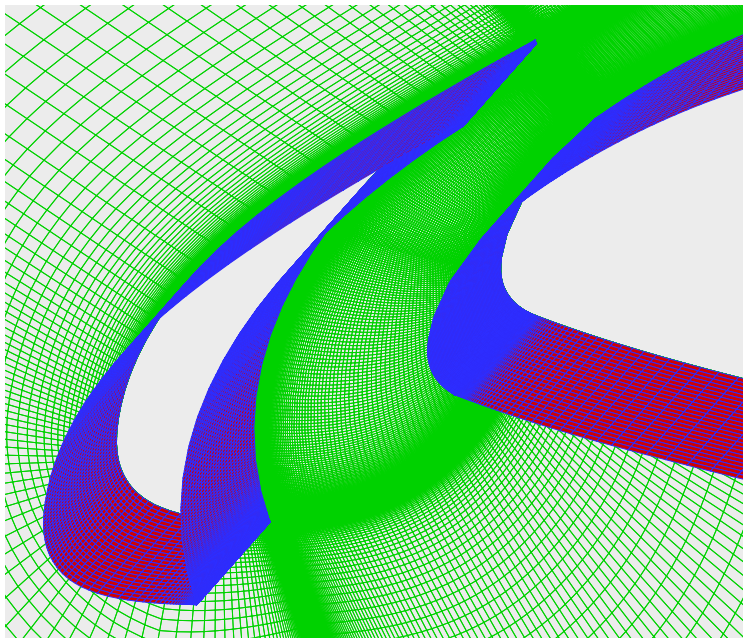

Figure 5.2: A view of the grid in the slat cove region.

cove which reveal the physics mechanism of the broadband noise generation and the characteristic of the noise.

Unless indicated otherwise, all values in the followings of this section are shown in non-dimensionalized form and all the length scales are non-dimensionalized by $C^* = 0.8$ m which is the chord length of the wing without the slat and flap deployed, velocities are non-dimensionalized by $c^*_\infty = 340$ m/s, density is non-dimensionalized by $\rho^*_\infty = 1.225$ kg/m^3, pressure is non-dimensionalized by $\rho^*_\infty c^{*2}_\infty$.

5.3.1 Instantaneous Flow

First the instantaneous vortical structures are shown by the iso-surface of the criterion Q [111] which is defined as:

$$Q = \frac{1}{2}(\Omega_{ij}\Omega_{ij} - S_{ij}S_{ij}) = -\frac{1}{2}\frac{\partial u_i}{\partial x_j}\frac{\partial u_j}{\partial x_i} > 0 \tag{5.1}$$

where S_{ij} and Ω_{ij} are the symmetric and antisymmetric components of $\nabla\mathbf{u}$.

Figure 5.3 shows the vortical structures in the slat cove where the iso-surface of $Q = 200$ colored with the z-direction vorticity (ω_z) in the range of -100 to 100 is plotted. The eddies are generated from the slat cusp and are mainly two-dimensional at the beginning. As they are rolling up towards the reattachment points in the shear layer, they become more and more three-dimensional. Near the reattachment point the vortex structures are distorted by the mean flow strain and some of the vortex structures pass through the gap and some of them are entrapped into the slat cove toward the cusp again. The entrapped vortex structures induce a secondary separation on the slat cove surface and the generated secondary vortex structures are believed to be one of the causes of the rapid three-dimensional break down of the vortex structures in the shear layer [52].

Figure 5.4 shows the strong unsteadiness in the slat cove region which can not be captured by the fully turbulent calculation of Chapter 3 by plotting the z-direction vorticity on 3 different cross section planes where L_z is the spanwise length. The calculated three-dimensional coherent vortical structures are consistent with the PIV measurements [112, 44, 43, 89] and numerical simulations [52, 51]. The vortex shedding from the trailing edge is shown in Figure 5.5 where the similar vortex pattern to what was captured in the 2D calculation of Chapter 3 is displayed and the three-dimensional effect can be seen clearly.

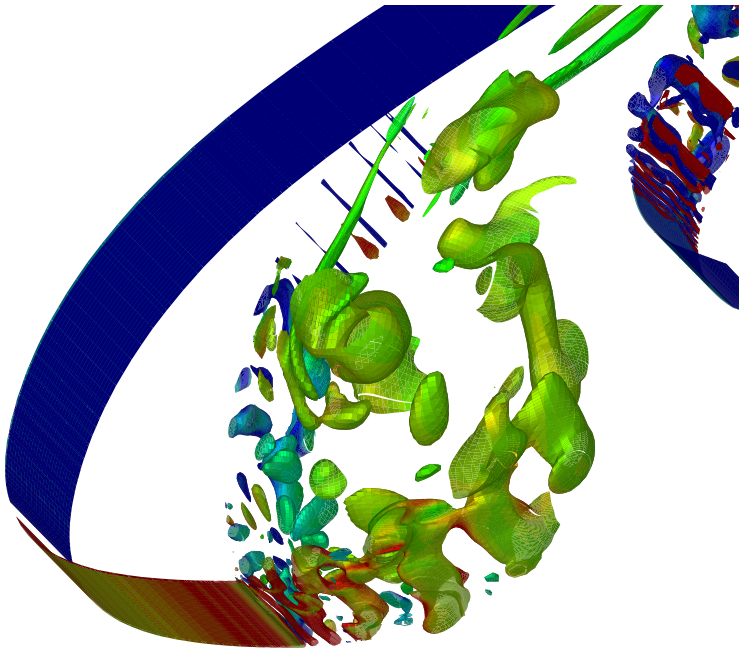

Figure 5.3: Q iso-surface colored with z-direction vorticity (Q=200, $\omega_z = -100$ to 100).

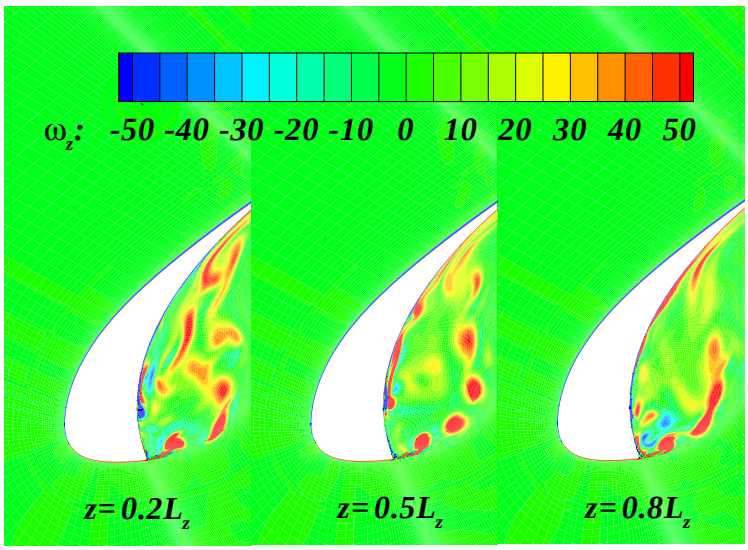

Figure 5.4: z-direction vorticity contours on 3 different z planes.

5.3.2 Time Averaged Flow

The mean variables are averaged over the last 60,000 steps which corresponds to 6 non-dimensional time units or 10 slat flow through time units. Figures 5.6 shows the

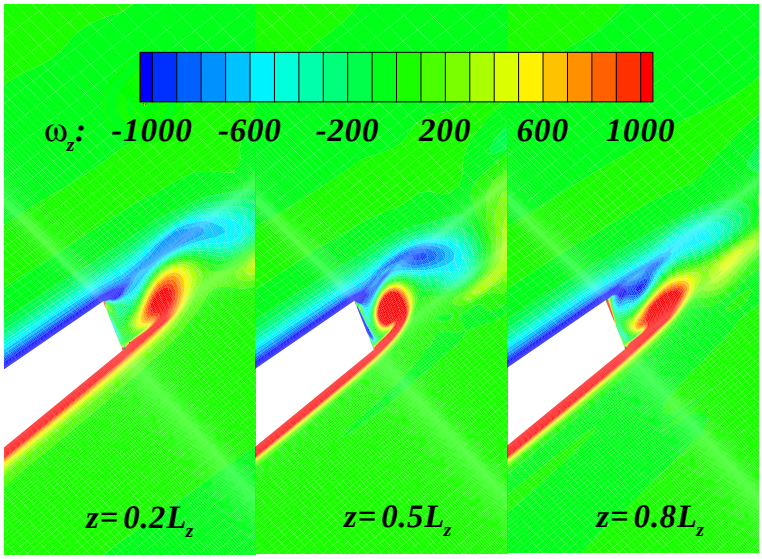

Figure 5.5: z-direction vorticity contours near trailing edge on 3 different z planes.

mean flow streamlines and the mean Mach contours of the high-lift configuration. Same as the results of the 2D fully turbulent calculations in Chapter 3, the acceleration of the flow through the slat/main element gap and the slow speed recirculation zone is separated by a shear layer. The trajectory shape of the shear layer of the 3D and 2D simulations is very similar. The distance from the reattachment point to the cusp of the slat in the 2D case is $63.875 \times 10^{-3}C$ and that of the 3D case is $62.875 \times 10^{-3}C$ which shows that the cove flow of the two-element configuration at 12 degrees of angle of attack has a good match to that of three-element configuration at 5 degrees of angle of attack.

The profiles of the mean velocity magnitude $|\mathbf{u}_0|$ on two lines in the slat cove are plotted in Figure 5.8 and the locations of the monitoring lines are given in Figure 5.7. In Figure 5.8 the distance (d) is calculated from the slat cove surface and is non-dimensionalized by the chord of the high-lift configuration. Along the line A the velocity magnitude firstly increases from zero as it departs from the non-slip wall. Then in the recirculation bubble the velocity magnitude decreases towards zero as it approaches the centre of the bubble and increases again when it passes the centre. In the shear layer, there is a significant velocity gradient and velocity magnitude increases rapidly and out of the shear layer the velocity decreases again. Similar trend appears on line B except that the velocity magnitude keeps increasing out of the shear layer as the local flow is accelerated through the gap.

The time and span averaged z-direction vorticity in the slat cove region of LES is shown in Figure 5.10 which is consistent with the 2D fully turbulent calculation

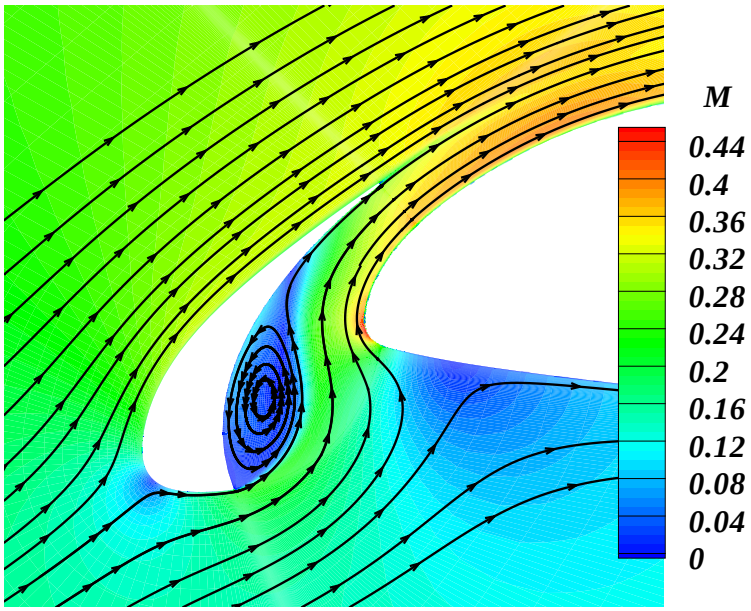

Figure 5.6: A zoomed view of the mean flow stream line near the slat.

results in Figure 5.9 . The PIV measurements and the 3D pseudo-laminar simulation in Ref. [52] showed similar results except the vorticity thickness was thinner in the 3D pseudo-laminar results.

5.3.3 Fluctuation Statistics

The fluctuation statistics of the flow fields indicate the characteristic of the unsteadiness and the noise sources. The 2D turbulent kinetic energy (TKE) calculated in the Chapter 4 with the zonal laminar method is shown in Figure 5.11 and the 2D turbulent kinetic energy (TKE) of LES on the middle cross section is shown in Figure 5.12. Here the 2D turbulent kinetic energy is defined as

$$\mathrm{TKE}_{2\mathrm{D}} = \frac{1}{2}(\overline{u'^2} + \overline{v'^2}) \tag{5.2}$$

where the overbar means the time average. The zonal laminar results show extreme large TKE value within the recirculation zone which is not consistent with the experiment data [89, 44] and 3D simulations [52]. The 3D LES gives high 2D TKE value near the slat cusp, the reattachment point and in the recirculation zone. The velocity fluctuation is monitored on line C on the middle cross section as shown in Figure 5.13. Examination of the RMS values of different velocity components on

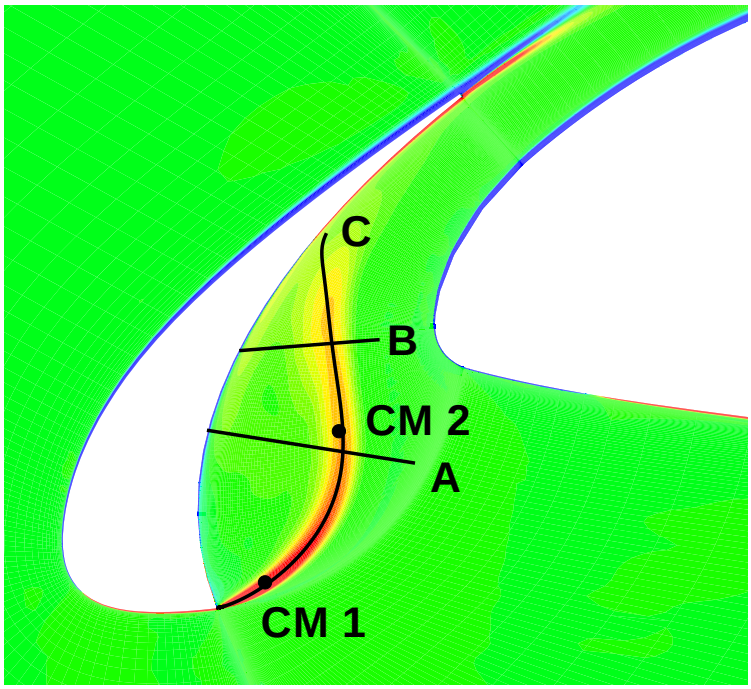

Figure 5.7: Locations of the mixing layer profile monitoring lines.

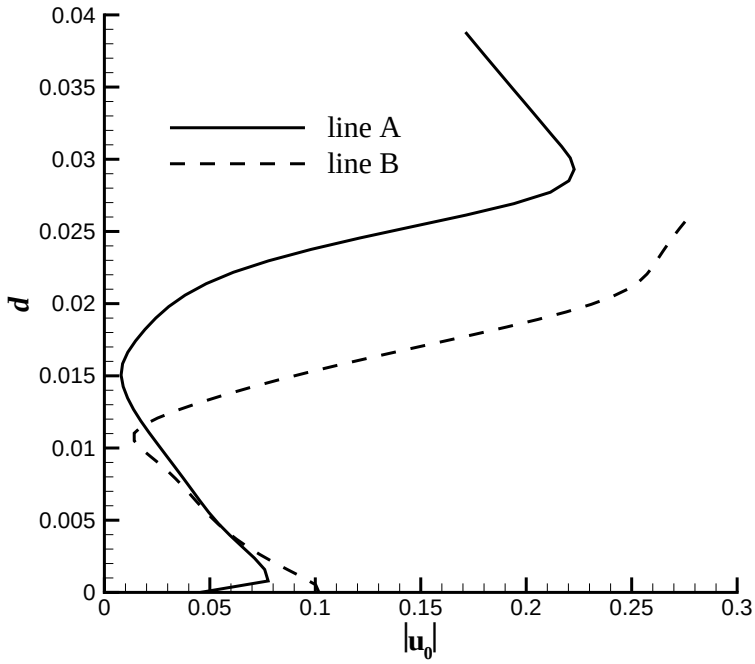

Figure 5.8: Mean velocity profiles on the monitoring lines.

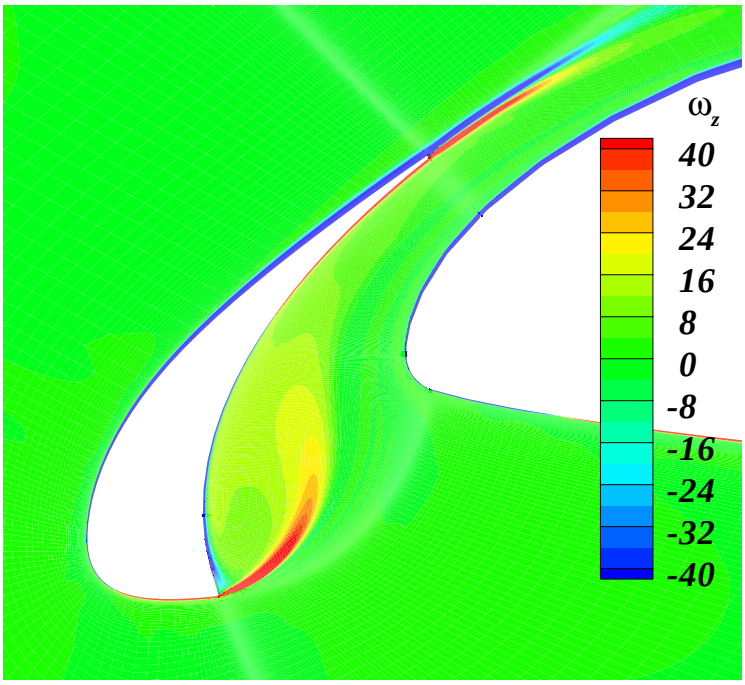

Figure 5.9: Time averaged z-direction vorticity in the slat cove region obtained by the 2D fully turbulent calculation.

line C indicates that u has a nearly constant fluctuation level along the shear layer trajectory. v has two peaks along the shear layer trajectory, of which one is near the slat cusp and the other is near the reattachment point. In most part of the trajectory the w component has similar fluctuation level as that of u component except near the reattachment point. The resulted 3D turbulent kinetic energy ($\text{TKE}_{3\text{D}} = \frac{1}{2}(\overline{u'^2}+\overline{v'^2}+\overline{w'^2})$) increases from the slat cusp to the first peak and then near the reattachment point it has two peaks. One is due to the large v fluctuation and the other one is due to the large w fluctuation.

The velocity components fluctuations inside the recirculation zone are monitored on the line A as shown in Figure 5.14. The monitored results show a fully three-dimensional flow in the recirculation bubble. The u and w components have a peak fluctuation level about 10 percent of the freestream velocity and higher peak value of 21 percent of the freestream velocity is observed for the v component. It should be noted that in the vicinity of the slat suction surface, the w has a relatively large value as the result of the three-dimensional secondary separation flow.

The spanwise correlations are monitored within the shear layer on two lines parallel to the z-axis starting from the points with the Cartesian coordinates of

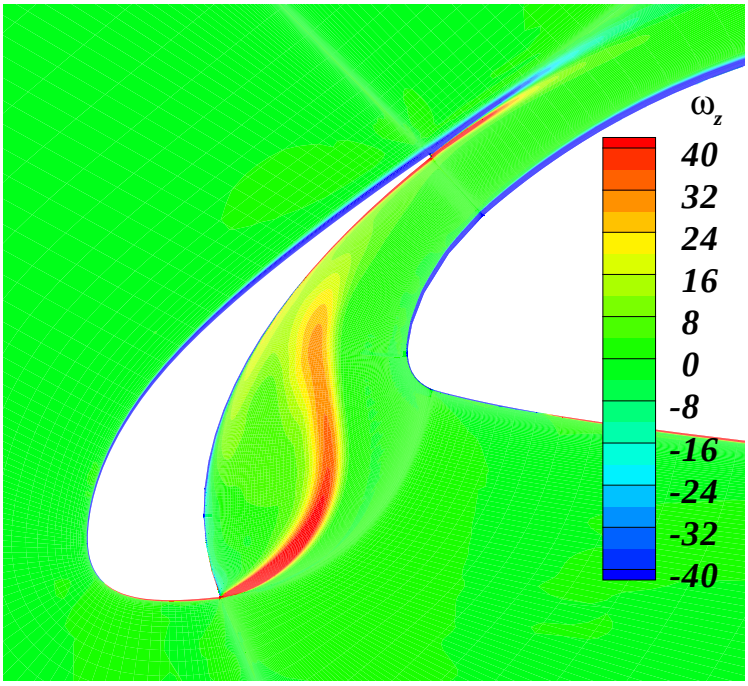

Figure 5.10: Time averaged z-direction vorticity in the slat cove region obtained by the LES.

(-0.0065, 0.05625, 0.024) and (0.007375, 0.085, 0.024) respectively as shown in Figure 5.7 where the projections of the two lines on x-y plane are shown as CM 1 and CM 2. The Figures 5.15 and 5.16 show the correlation coefficient of the velocity components fluctuations along the spanwise direction where R_{uu} is defined as $\overline{u'(x_0, y_0, z_0)u'(x_0, y_0, z)}/\overline{u'(x_0, y_0, z_0)u'(x_0, y_0, z_0)}$ for a given staring point (x_0, y_0, z_0) and similar definition applies to R_{vv} and R_{ww} where the overbar means the time average. The coefficients give exponentially decreases in the spanwise direction indicating that the spanwise grid size and the spanwise length used in the calculation are acceptable and the acoustic sources coherence length is small compared with the chord length. It should be noted that additional computation with smaller spanwise grid size and larger spanwise length can resolve the smaller spanwise structures and describe the spanwise coherence more clearly.

The power spectral densities (PSD) of monitor position 1 at (-0.0065, 0.05625, 0.024) and monitor position 2 at (0.007375, 0.085, 0.024) are shown in Figure 5.17. The PSD is defined as $2|\hat{\phi}_f|^2$ where $\hat{\phi}_f$ is the Fourier transform coefficient at frequency f. In the results shown, the PSD is normalized by $\rho_\infty^{*2} c_\infty^{*4}$. The sampling rate is 1.0×10^3 and a total of 18,000 samples which are split into 4 blocks are used.

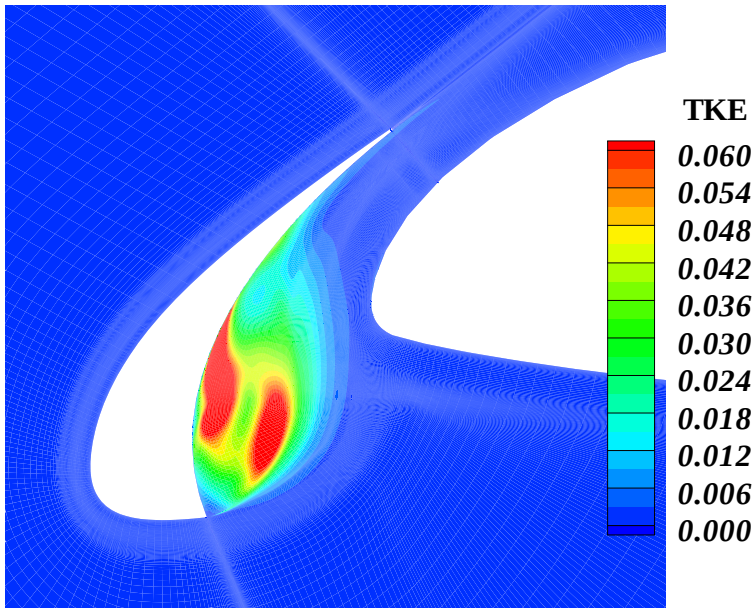

Figure 5.11: Time averaged turbulent kinetic energy in the slat cove region obtained by the zonal-laminar simulation.

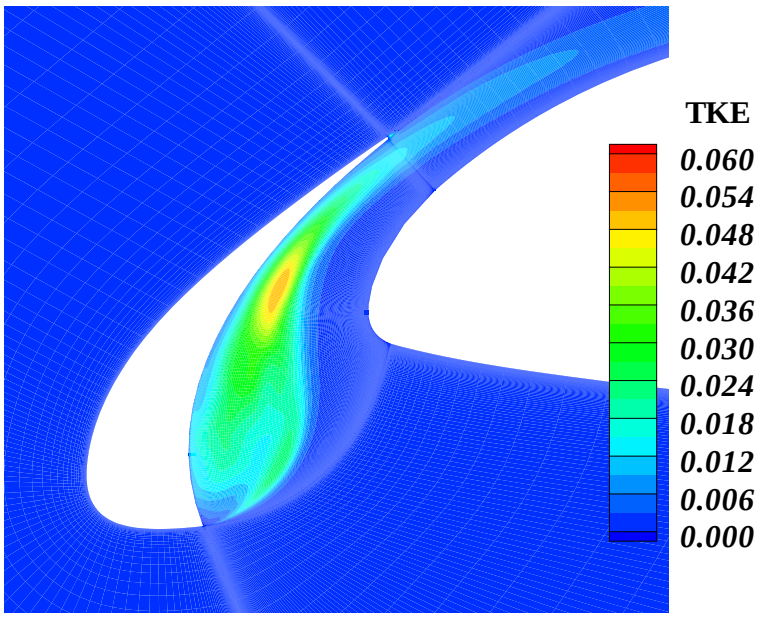

Figure 5.12: Time averaged turbulent kinetic energy in the slat cove region obtained by the LES.

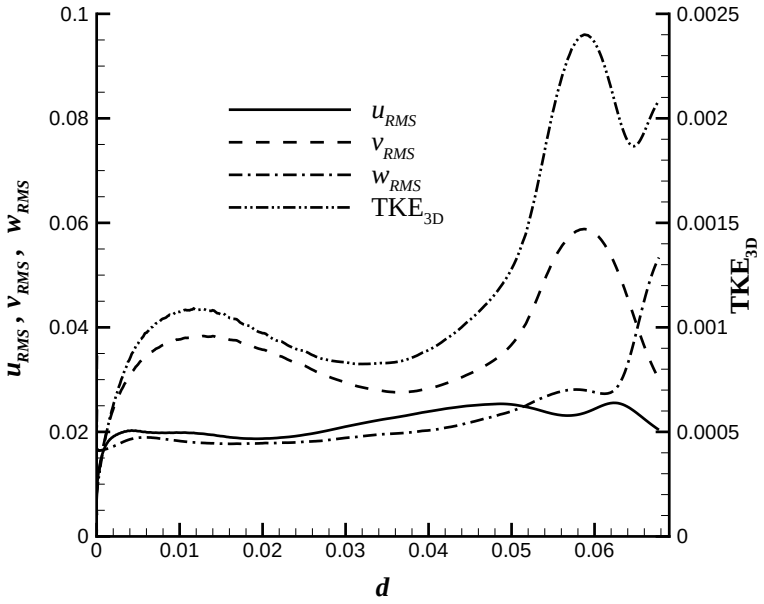

Figure 5.13: 3D TKE and velocity fluctuations along the monitoring line C.

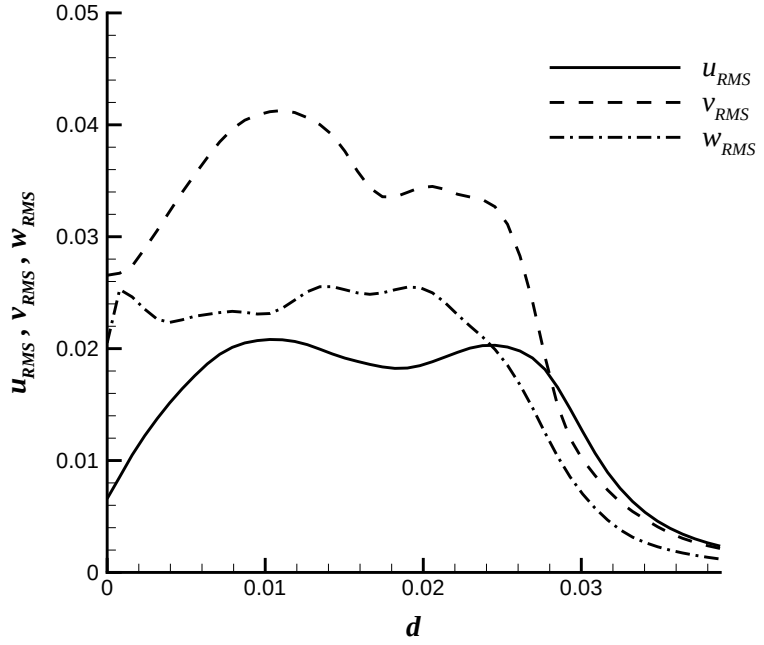

Figure 5.14: Velocity fluctuations along the monitoring line A.

The resulting frequency resolution is about 0.22. The spectra show the broadband characteristic of the slat cove flow and the acoustic power clustered in the frequency range of 2.0 to 8.0 which corresponding to the St=1.2 to 4.8 (where the Strouhal

number $St = fC_s/u_\infty$ is based on the freestream velocity u_∞ and slat chord C_s). This result agrees with the measurements of Ref. [113]. The frequency spectra of the pressure fluctuations near the slat trailing edge is shown in Figure 5.18. The pressure monitoring point is on the middle crosse section and located along the slat chord line and at a distance of 1.475×10^{-3} from the trailing edge of the slat. The spectra is obtained by performing a FFT of the monitored pressure history. The sampling rate is 1.0×10^4 and a total of 40,960 samples which are split into 10 blocks are used. The resulting frequency resolution is about 2.4. The FFT result shows that he vortex shedding from the slat trailing edge has a frequency of 47 which gives an acceptable agreement with the results of the Chapter 3. The discrepancy is at least partly due to the different time integration schemes.

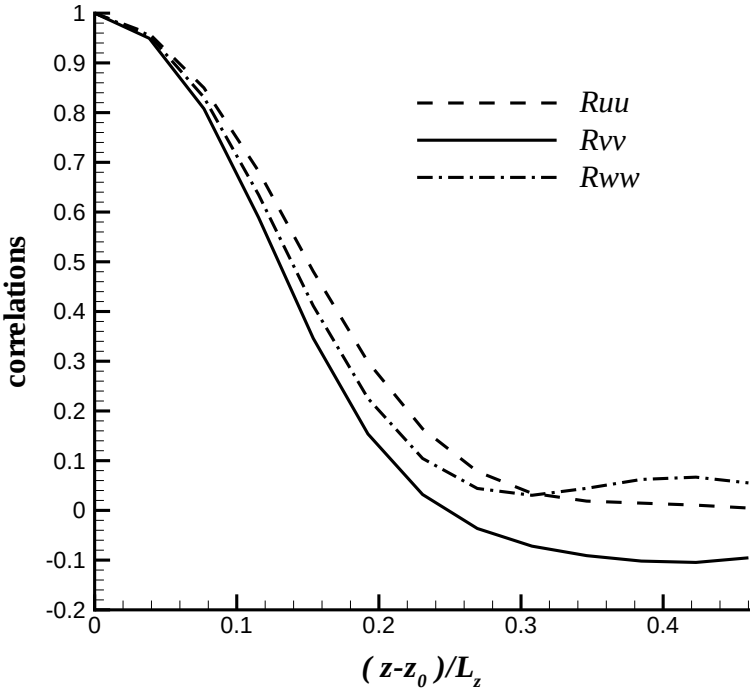

Figure 5.15: Spanwise correlation of velocity components fluctuation on the monitoring line 1.

5.4 Liner Performance

With the noise source $\mathbf{q}_m = -(\omega \times \mathbf{u})'$ calculated from the LES, the APE are solved to examine the broadband slat noise attenuation performance of acoustic liner treatment inside the slat gap. The attenuation is evaluated by comparing the

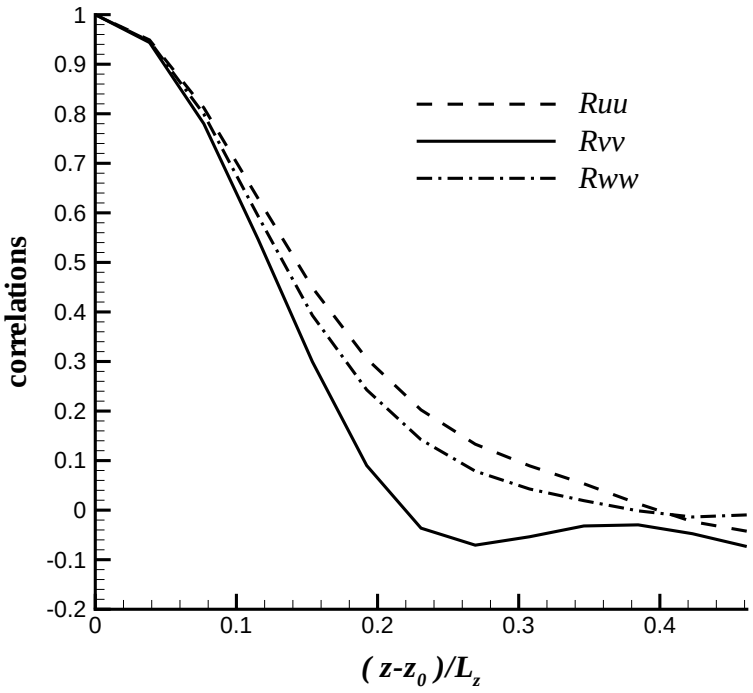

Figure 5.16: Spanwise correlation of velocity components fluctuation on the monitoring line 2.

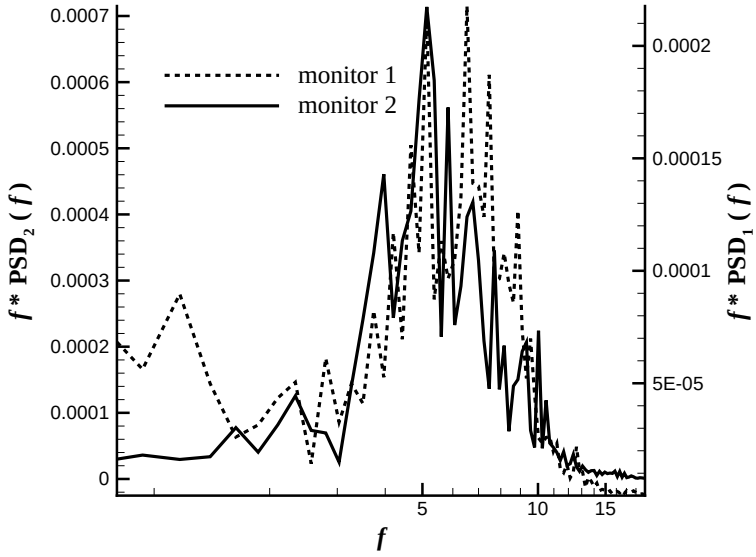

Figure 5.17: Frequency spectra at different monitoring points.

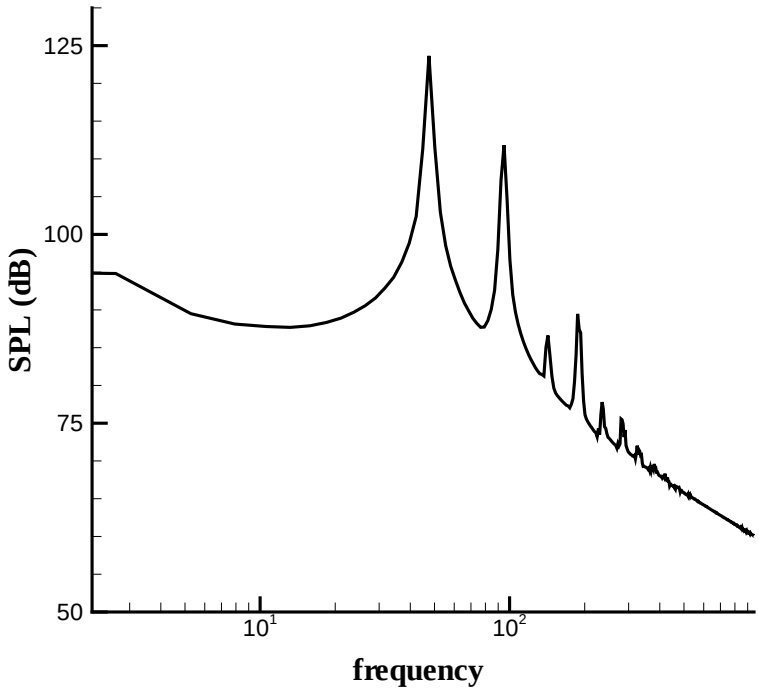

Figure 5.18: Frequency spectra of the pressure fluctuations near the slat trailing edge.

farfield directivity and sound pressure level.

5.4.1 Grid and Computation Setup

The 3D grid for APE calculation is generated by uniformly extrude a basic 2D grid along the spanwise (z) direction. The basic 2D grid consists of 94 blocks with a total of 46,904 nodes and the total computational domain ranges form -1.75C to 1.75C in both x and y direction(Figure 5.19). The grids are designed to ensure an equivalent grid resolution of at least 7 PPW in wave propagation direction for a wave frequency up to 12. Same as the LES grid, a total of 26 grid points are used in spanwise direction yielding a total of 1.2 million points. The grid near the slat cove region is shown in Figure 5.20.

Same as in the previous chapters, the acoustic fields of three cases are calculated: 1) hard wall, 2) slat cove surface lined only, 3) slat cove surface and main element lined. The same impedance value used in the Chapter 4 is used here. The explicit fourth order Runge-Kutta solver is used and the time step size is $0.0004C/c_\infty$ corresponding to a CFL of 0.65. The time step corresponds to a sampling frequency of 1.0625 MHz and the calculations are performed for 10 non-dimensional

time units for each case. The computation is performed on a Linux cluster using 12 2.2 GHz AMD Opterons CPUs and the CPU cost per time step is 1.25 s. A zone including the shear layer and reattachment point is chosen as the source region and the acoustic sources are interpolated from the LES grid to the APE grid using the inverse-distance method described in Chapter 4. A view of the interpolated z-component of the acoustic sources is shown in Figure 5.21.

The FW-H equation is solved to compare the far-field acoustic signals for different cases. Similar to the Chapter 4 an integration surface enclose all the high lift configuration is used and the same observer positions of the Chapter 4 are used here.

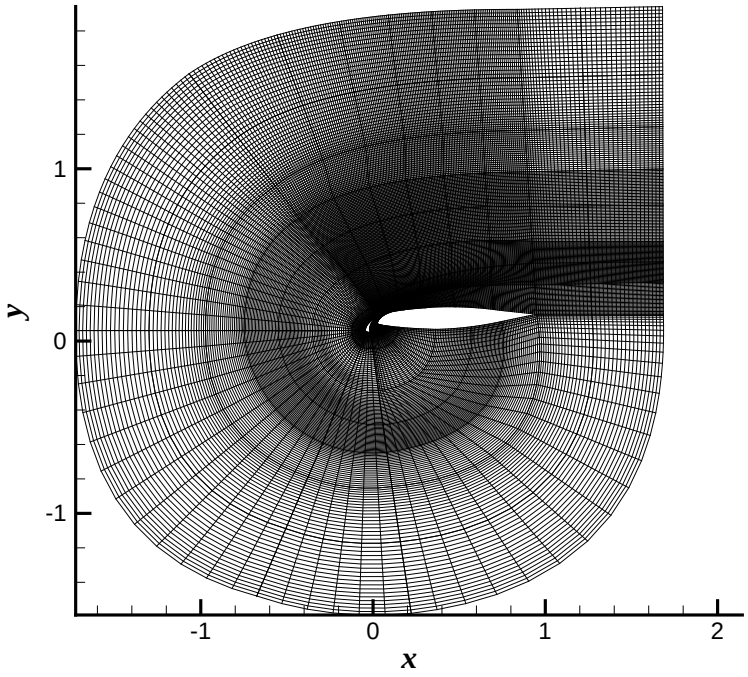

Figure 5.19: The crosse section of the computational grid for 3D APE calculation.

5.4.2 Results and Comparison

The source driven acoustic pressure fields with the hard wall, slat lined and slat and main element both lined conditions are shown in Figures 5.22 to 5.24. The acoustic pressure fields show the broadband characteristics of the slat noise and the noise attenuation effect of acoustic liners. To quantitatively compare the results of LES and source driven APE, the farfield directivity obtained by solving FW-H is given

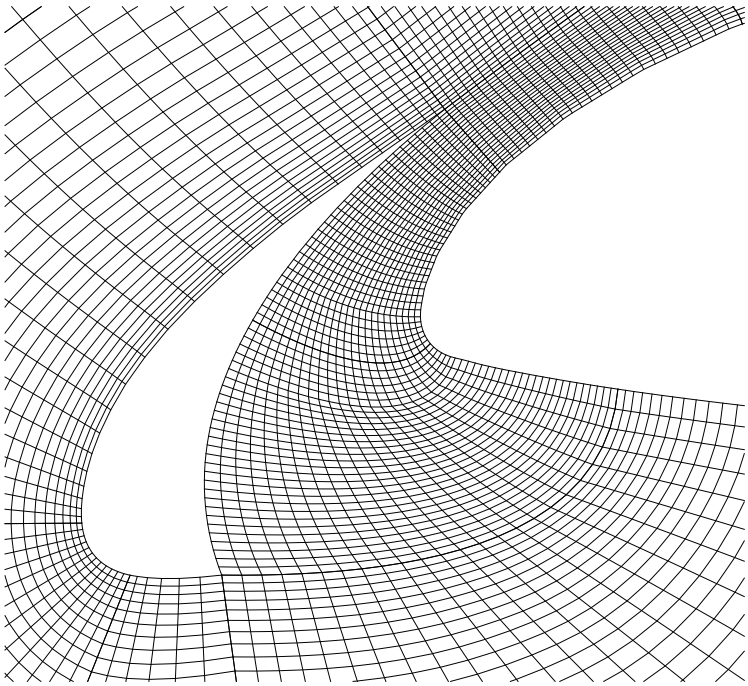

Figure 5.20: A zoomed view of the computational grid for 3D APE calculation.

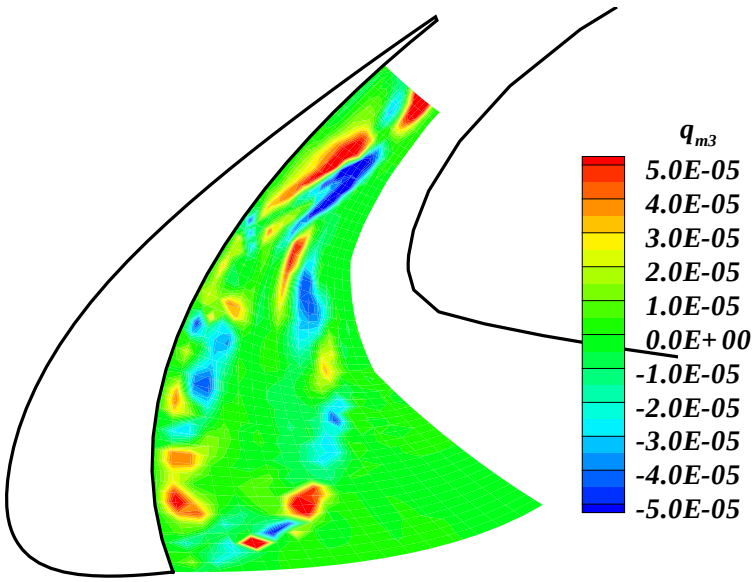

Figure 5.21: A view of the z-direction component of the interpolated acoustic sources.

in Figure 5.25, where the sound pressure level of different observers are given and the observer angle is zero degree in x-direction and increases anti-clockwise. By examining the hard wall results of LES and source driven APE, it can be concluded that they agree well in general and the discrepancy is less than 2 dB for most of angles. It should be noted that there is a shift of the peak for APE results relative to the LES results which is at least partly due to the mean flow effect in the LES calculation. The lined cases show the attenuation in most of the angles and it's not surprise that the both lined case performed better than slat lined case. For the most interested angle range of 220 degrees to 340 degrees within which the noise propagating towards the ground, the liners show encouraging results which gives an attenuation larger than 2 dB for observer angle larger than 260 degrees.

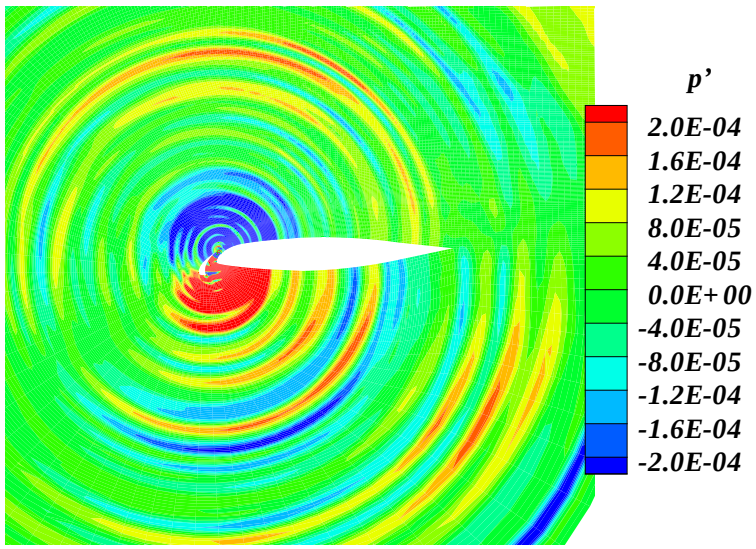

Figure 5.22: The acoustic pressure field of the high lift configuration solved by source driven APE with hard wall condition.

The FFT is performed for the acoustic pressure history obtained at each observer point and the sampling rate is 2.5×10^3 and a total of 21,250 samples which are split into 10 blocks are used. The resulting frequency resolution is about 1.2. Figure 5.26 shows the attenuation in narrow band spectra calculated by averaging the values of different observer positions where the define of attenuation in Chapter 3 is used. The maximum attenuation for slat lined case is 1.9 dB at the frequency of 4.7 and the maximum attenuation for slat and main element both lined case is 2.4 dB at the frequency of 4.7. The overall attenuation obtained by averaging the attenuations at different frequencies is 0.8 dB for slat lined case and the overall attenuation for slat

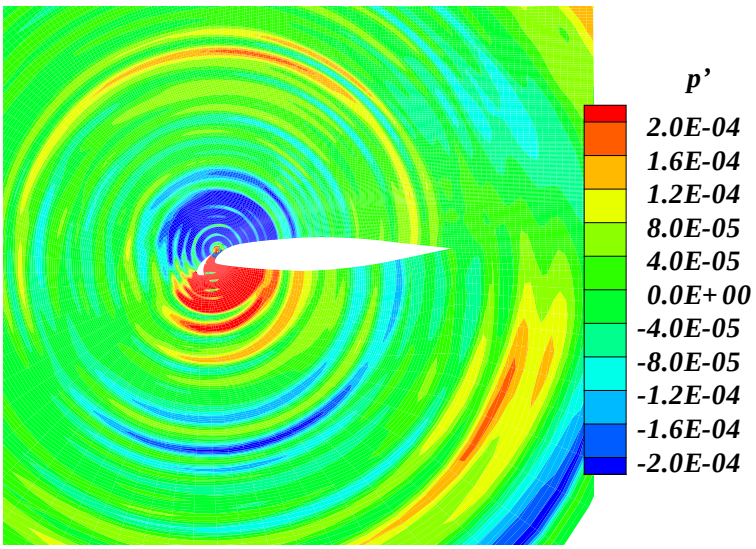

Figure 5.23: The acoustic pressure field of the high lift configuration solved by source driven APE with slat lined condition.

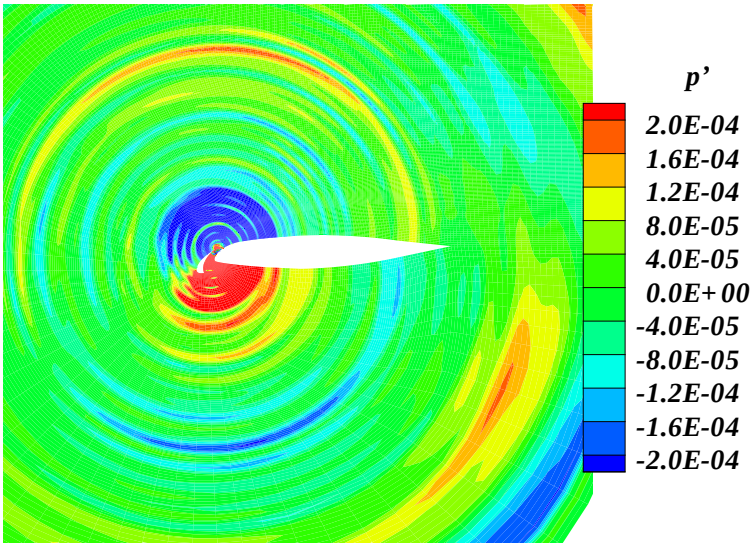

Figure 5.24: The acoustic pressure field of the high lift configuration solved by source driven APE with both lined condition.

and main element both lined case is 1.0 dB.

The spectra of the pressure perturbation at the monitoring point obtained using the different methods are compared in the Figure 5.27. The monitoring point is at (0.2, -0.5) in the 2D calculations and at (0.2, -0.5, 0.024) in the 3D calculations. For

the pseudo-laminar zonal method, SNGR method and LES the frequency resolution is about 0.23 and for the source driven APE method the frequency resolution is 1.2. The results of the source driven APE agree well with that of the LES in term of the sound pressure level and the trend of the decay of the sound pressure level along the frequency. The results of the pseudo-laminar zonal method show larger value in the low frequency range which is believed due to the overpredicted unsteady flow and the larger vortical structures in the slat cove region. The results of the SNGR method show smaller sound pressure level compared with the results of LES and give a rapid decay of the sound pressure level at high frequencies due to the shape of the Von Karman spectrum.

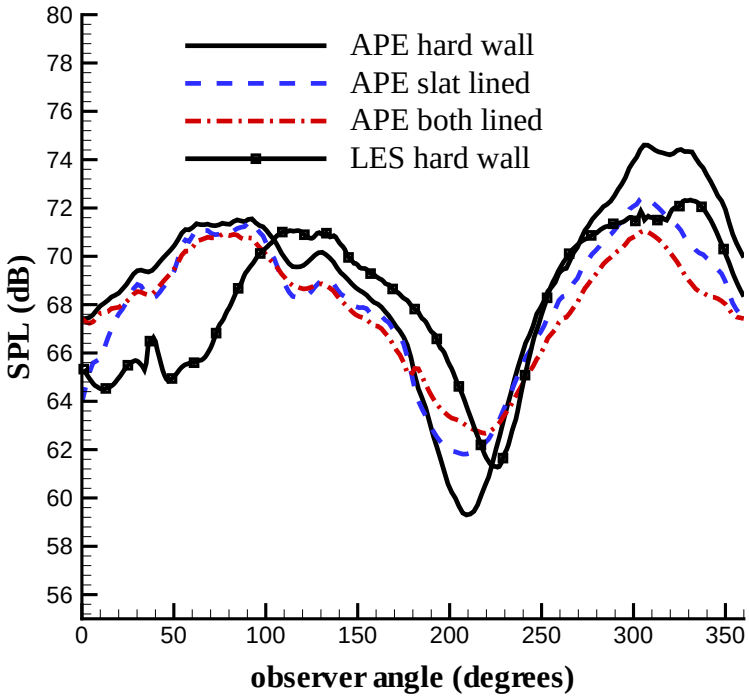

Figure 5.25: Comparison of the farfield directivity results of LES and source driven APE.

5.5 Summary

The broadband slat noise generation of a high-lift configuration has been simulated using LES in this chapter. The calculated results show the characteristics of the unsteady flow and the mechanisms of the broadband noise generation. The LES calculated noises sources were then used to drive the APE. The source driven APE

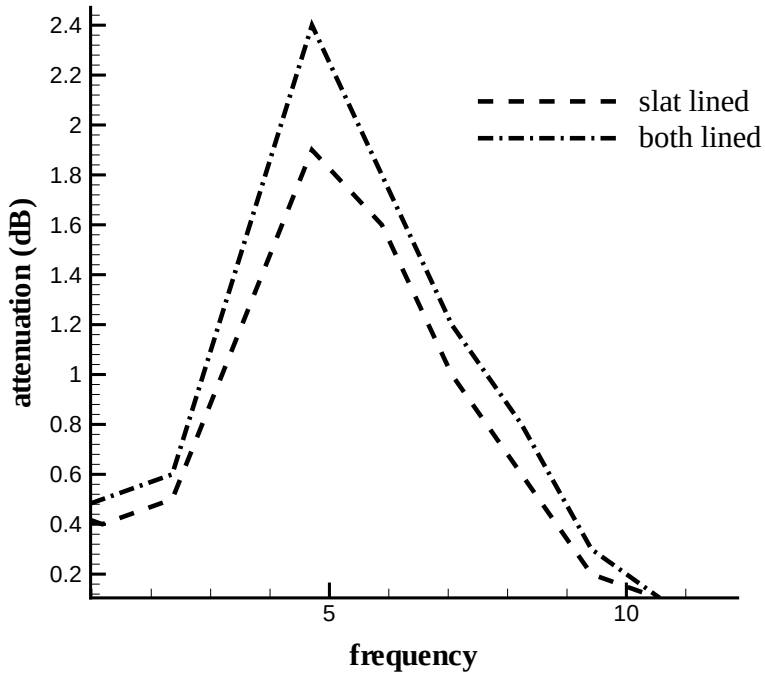

Figure 5.26: The averaged attenuation along the frequency.

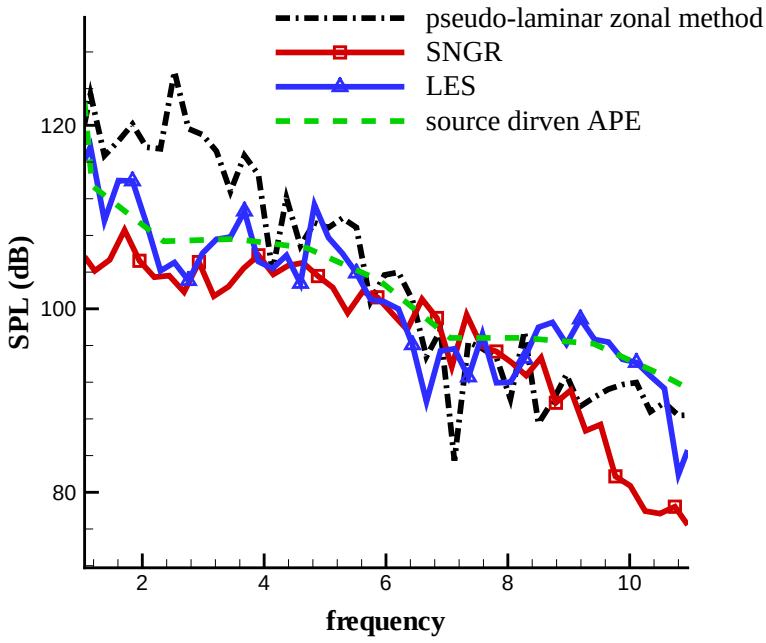

Figure 5.27: Comparison of the spectra of the pressure perturbation at the monitoring point obtained using different methods.

results agree well with that of LES in term of far field directivity and sound pressure level. The broadband noise attenuation effect of the acoustic liner treatment in the slat/main element gap has been investigated by applying the acoustic liners to the APE calculated acoustic field. Results of a non-optimised acoustic liner show that the overall attenuation is 0.8 dB for slat lined case and the overall attenuation for slat and main element both lined case is 1.0 dB.

Chapter 6

Summary and Future Work

In this final chapter the main results obtained are summarized and suggestions for the future studies are given.

6.1 Summary

The aims of this research were to investigate the generation and radiation of noise by slat flow and the passive control the noise using acoustic liners. As there are the high frequency tonal components and low to middle frequency broadband components in the slat noise spectrum and they have different mechanisms of noise generation, different numerical approaches are used. The main achievements so far are summarized below.

- The fully turbulent aeroacoustic simulations of the flow field of the high-lift wing model show the vortex shedding from the blunt trailing edge and associated high-frequency tonal noise. The high frequency noise sources are replaced with an idealized dipole source and the sound field of the high-lift configuration with this source has been simulated using the high-order linearized Euler code SotonLEE with and without the liners applied on the slat gap. A range of liner impedance value has been evaluated to search for a optimized liner. The farfield acoustic signal results show that the presence of liner can significantly attenuate the high frequency noise emanated from the slat trailing edge.

  Using the optimized impedance value, aeroacoustic simulations for the high-lift wing with acoustic liner treatment have been performed. The results show that liners on the slat and main element provide useful attenuation for the high frequency tonal noise. The directivity patterns in the angular range 240 degrees to 340 degrees show that the attenuation for a liner on slat cove surface

is 1.6 dB, whereas the attenuation with liners on both the slat cove and the main element is 4.1 dB.

- The acoustic field generated by broadband noise sources in the slat cove region of the high lift wing model has been simulated using the pseudo-laminar zonal method and the SNGR method. The SNGR method has been shown to be a potentially useful method to model the generation of broadband slat noise and to investigate the attenuation potential of slat gap acoustic liners, for which the interest is in changes of noise level rather than the absolute value. Predictions for a non-optimised acoustic liner show that the maximum attenuation for the slat lined case is 0.55 dB at 2 kHz and the maximum attenuation for the slat and main element both lined case is 2.3 dB at 1.5 kHz. The overall attenuation for slat lined case is 0.25 dB and the overall attenuation for slat and main element both lined case is 1.15 dB.

- Finally the broadband slat noise generation of the modified high-lift configuration (with flap retracted) has been simulated using LES. The calculated results show that the three dimensional unsteady flow in the slat cove region is associated with the broadband noise sources. The flow near the reattachment point has large fluctuation values and contributes to the broadband noise generation. The LES calculated noises sources were then used to drive the acoustic perturbation equations. The source driven APE results agree well with that of LES in term of far field directivity and sound pressure level. The broadband noise attenuation effect of the acoustic liner treatment in the slat/main element gap has been investigated by applying the non-optimised acoustic liner to the APE calculated acoustic field. The maximum attenuation for the slat lined case is 1.9 dB at 2.0 kHz and the maximum attenuation for the slat and main element both lined case is 2.4 dB at 2.0 kHz. The overall attenuation for the slat lined case is 0.8 dB and the overall attenuation for the slat and main element both lined case is 1.0 dB.

These works explored the different numerical methods for the slat noise generation and radiation which covers the fast SNGR to the accurate LES. The slat noise generation mechanism revealed is that the high frequency tonal noise sources are associated with the vortex shedding from the slat blunt trailing edge and the broadband noise source are associated with the three-dimensional unsteady flow in the slat cove region. This result answered an important question of the slat noise research. The liner performance study justified the feasibility of attenuation the slat noise using acoustic liners. For the most interested directivity angle range, the

attenuation could be larger than 2 dB and more attenuation can be expected using optimized liners.

6.2 Future Work

As stated in the literature review, the slat noise acoustic spectrum contains both high frequency tonal components and low to middle frequency broadband components. Generally, for a commercial aircraft in flight, the broadband noise is more important [37].

The tonal noise generation mechanism has been well investigated [39, 30, 41]. Potential attenuation methods for the tonal noise include perforated material [114], serrated tape [36], and acoustic liner [38]. All the treatments give a significant reduction of the tonal noise. So future work should focus on the broadband component of the slat noise.

Further to this thesis, there are several issues need to be addressed to investigate the broadband slat noise attenuation potential of acoustic liners. First the LES calculated in this work is on a grid with a relatively small spanwise length and limited spanwise resolution. A refined grid simulation with larger spanwise length, higher spanwise resolution and finer gird points in the slat cove region would help to capture smaller spanwise scales and spanwise coherence. The accurate simulation of the spanwise coherence length is important as it determine the sources distribution in the spanwise which has a direct impact on the far-field acoustic intensity. Further more the subgrid stress model used in the LES is the standard Smagorinsky model. The dynamic subgrid stress models [115, 116] could be used as it is reported that they provide superior performance. Second only the 2D case of the SNGR method is performed in this work with the homogeneous isotropic turbulence assumption. The future work need to take into account the three-dimensional effect and the anisotropy of turbulence near the wall [99]. In addition, there are several alternatives to the acoustic source definition and the corresponding modified linearized Euler equations used in this work [26, 34]. An evaluation of these methods would be useful to find the most suitable approach to simulate the source driven slat noise radiation. Last the coupling of an optimization algorithm with the noise radiation calculation is needed to optimize the acoustic liners for the broadband noise in order to achieve further attenuation.

Appendix A

Time Domain Impedance Boundary Condition

In this appendix, the derivation of the time domain impedance boundary condition (TDIBC) proposed by Fung [68] is presented. In frequency domain the reflection wave $\hat{u'}^- = \hat{u'} - \hat{p'} = (1 - Z)\hat{u'}$ at right boundary is related to the incident wave $\hat{u'}^+ = \hat{u'} + \hat{p'} = (1 + Z)\hat{u'}$ by

$$\hat{u'}^- = \hat{\Upsilon}(\omega)\hat{u'}^+ \tag{A.1}$$

where

$$\hat{\Upsilon}(\omega) = (1 - Z)/(1 + Z). \tag{A.2}$$

The complex function $\hat{\Upsilon}$ is indeed a direct measure of the magnitude of the reflection and its relative phase with the incident wave.

The Equation A.1 is equivalent to the convolution process of

$$u'^-(t) = \int_{-\infty}^{+\infty} \Upsilon(t - \tau)\hat{u'}^+(\tau)d\tau. \tag{A.3}$$

This convolution can be evaluated efficiently using Fung's method which is described in the following sections in which the derivatives of two broadband formulas are given.

A.1 Broadband Formula 1

Assuming the impedances model is

$$Z(\omega) = R_0 + i(X_{-1}/\omega + X_1\omega), \tag{A.4}$$

then $\hat{\Upsilon}(\omega)$ can be written as

$$\begin{aligned}\hat{\Upsilon}(\omega) &= \frac{1-Z}{1+Z} = \frac{2}{1+Z} - 1 \\ &= \frac{2}{1+R_0+i(X_{-1}/\omega + X_1\omega)} - 1 \\ &= \frac{2\omega}{\omega + R_0\omega + i(X_{-1} + X_1\omega^2)} - 1. \\ &= \frac{2}{iX_1}\frac{\omega}{\omega^2 + \frac{(1+R_0)}{iX_1}\omega + \frac{X_{-1}}{X_1}} - 1\end{aligned} \tag{A.5}$$

If $X_1 > 0$ and $X_{-1} < 0$, $\hat{\Upsilon}(\omega)$ has the simple poles

$$\begin{aligned}&\omega_{1,2} = \pm\omega_R + i\omega_I \\ &\omega_R = \sqrt{(-X_{-1}/X_1) - [(1+R_0)/2X_1]^2}. \\ &\omega_I = (1+R_0)/2X_1\end{aligned} \tag{A.6}$$

This implies that $\Upsilon(t)$ is causal. According Cauchy's residue theorem $\Upsilon(t)$ has the from

$$\Upsilon(t) = \begin{cases} i\sum_{j=1}^{2} \text{residue}\left[\hat{\Upsilon}(\omega), \omega_j\right] e^{i\omega_j t} & t \geq 0 \\ 0, & t \leq 0 \end{cases} \tag{A.7}$$

and $\hat{\Upsilon}(\omega)$ can be written as

$$\hat{\Upsilon} = \frac{1}{iX_1}\frac{2\omega}{(\omega-\omega_1)(\omega-\omega_2)} - 1, \tag{A.8}$$

then

$$\text{residue}\left[\hat{\Upsilon}(\omega), \omega_1\right] e^{i\omega_1 t} = H(t)\frac{1}{iX_1}\frac{2\omega_1}{\omega_1-\omega_2}e^{i\omega_1 t}, \tag{A.9}$$

$$\text{residue}\left[\hat{\Upsilon}(\omega), \omega_2\right] e^{i\omega_2 t} = H(t)\frac{1}{iX_1}\frac{-2\omega_2}{\omega_1-\omega_2}e^{i\omega_2 t}. \tag{A.10}$$

Let

$$\tilde{\Upsilon}(t) = \frac{1}{X_1\omega_R}(\omega_1 e^{i\omega_1 t} - \omega_2 e^{i\omega_2 t}), \tag{A.11}$$

then $\Upsilon(t)$ can be written as

$$\Upsilon(t) = \tilde{\Upsilon}(t)H(t) - \delta(t) \tag{A.12}$$

and $\tilde{\Upsilon}(t)$ has another form

$$\tilde{\Upsilon}(t) = [2/X_1]\left[\cos\omega_R t - (\omega_I/\omega_R)\sin\omega_R\right] e^{-\omega_I t}. \tag{A.13}$$

Then Equation A.3 can be written as

$$u^-(t) = \int_{-\infty}^{t} H(t-\tau)\tilde{\Upsilon}(t-\tau)u^+(\tau)d\tau - u^+(t). \tag{A.14}$$

It equals

$$u^-(t) = \int_{0}^{-\infty} H(\tau)\tilde{\Upsilon}(\tau)u^+(t-\tau)d\tau - u^+(t). \tag{A.15}$$

In a practical computation the integration is from 0 to T_ω. If the value of Z is known, various X_1 can be used to satisfy Equation A.4. Given an accuracy requirement ε for the integration of Equation A.3, we just need the value of $\Upsilon(\tau)$ when $(2/X_1)\sqrt{1+(\omega_I/\omega_R)^2}e^{-\omega_I T_\omega} \leq \varepsilon$ which suggests the possibility of optimum choices of an impedance model by minimizing $T_\omega = (1/\omega_I)\ln[(\frac{2}{X_1\varepsilon})\sqrt{1+(\omega_I/\omega_R)^2}]$ with respect to X_1.

The Equation A.15 can be calculated using trapezoidal integration:

$$u'^-(t) = -u'^+(t) + \frac{1}{2}\Delta t\tilde{\Upsilon}(0)u'^+(t) + \Delta t\sum_{k=1}^{N}\tilde{\Upsilon}(k\Delta t)u'^+(t-k\Delta t) \tag{A.16}$$

with $N\Delta t = T_\omega$.

Another efficient integration method is as following: Equation A.11 can be rewritten as

$$\tilde{\Upsilon}(t) = \frac{1}{X_1\omega_R}(\omega_1 e^{i\omega_1 t} - \omega_2 e^{i\omega_2 t}) = \mu_1 e^{i\omega_1 t} + \mu_2 e^{i\omega_2 t} \tag{A.17}$$

where $\omega_1 = \omega_R + i\omega_I$, $\omega_2 = -\omega_R + i\omega_I$.

Then Equation A.3 becomes:

$$\begin{aligned} u'^-(t) \quad &= -u'^+(t) + \int_{0}^{\infty}\tilde{\Upsilon}(\tau)u'^+(t-\tau)d\tau \\ &= -u'^+(t) + I_1(t) + I_2(t) \end{aligned} \tag{A.18}$$

where:

$$\begin{aligned} I_1(t) \quad &= \mu_1\int_{0}^{\infty} e^{i\omega_1\tau}u'^+(t-\tau)d\tau \\ &= \mu_1\int_{0}^{\Delta t} e^{i\omega_1\tau}u'^+(t-\tau)d\tau + \mu_1\int_{\Delta t}^{\infty} e^{i\omega_1\tau}u'^+(t-\tau)d\tau \end{aligned}$$

$$= \mu_1 \int_0^{\Delta t} e^{i\omega_1 \tau} u'^{+}(t-\tau) d\tau + \mu_1 \int_0^{\infty} e^{i\omega_1(\tau+\Delta t)} u'^{+}\left[(t-\Delta t)-\tau\right] d\tau$$

$$= \mu_1 \frac{1}{2} \Delta t \left[u'^{+}(t) + e^{i\omega_1 \Delta t} u'^{+}(t-\Delta t)\right] + e^{i\omega_1 \Delta t} I_1(t-\Delta t) \tag{A.19}$$

and

$$I_2(t) = \mu_2 \frac{1}{2} \Delta t \left[u'^{+}(t) + e^{i\omega_2 \Delta t} u'^{+}(t-\Delta t)\right] + e^{i\omega_2 \Delta t} I_2(t-\Delta t) \tag{A.20}$$

Using this formula the integration can be realized using recursive formula without having to localize the infinite integral by truncation and store a set of past history. So it is very memory and time efficient. The initial condition is:

$$\begin{aligned} & I_1(\Delta t) = 0 \\ & I_1(2\Delta t) = e^{i\omega_1 \Delta t} \mu_1 \frac{1}{2} [u'^{+}(\Delta t) + e^{i\omega_1 \Delta t} u'^{+}(0)] \\ & u'^{+}(0) = u'(0) + p'(0) \\ & u'^{+}(n^* \Delta t) = u'^{+}((n-1)^* \Delta t) \end{aligned} \tag{A.21}$$

A.2 Braodband Formula 2

The impedance model used in the preceding section is suitable for a liner frequency characteristic as shown in Figure 1.9 and the frequency range is relatively narrow. In order to solve the wider broadband characteristics of a liner, the previous formula is extended [69]. Start from Equation A.2

$$\hat{\Upsilon}(\omega) = \hat{\tilde{\Upsilon}}(\omega) - 1 \tag{A.22}$$

where

$$\hat{\tilde{\Upsilon}} = \frac{2}{1+Z} = \frac{2}{1 + R(\omega^2) + i\omega X(\omega^2)} = \frac{Q(s)}{D(s)} \tag{A.23}$$

R and X is the resistance and reactance respectively and they are real number. Here $s = i\omega$.

Assume $D(s)$ has the form $D(s) = (s-\lambda_1)(s-\lambda_2)(s-\lambda_3)\cdots(s-\lambda_1)$ and thus $\hat{\tilde{\Upsilon}}(\omega) = \sum_{k=1}^{m} \hat{\tilde{\Upsilon}}_k(\omega)$, with $\hat{\tilde{\Upsilon}}_k(\omega) = \frac{C_k}{s-\lambda_k}$. Because $D(s)$ has only real coefficients its zeros λ_k are either real or complex conjugate pairs. When one of the roots λ_k of $D(s)$ is complex, its conjugate λ_{k+1} must exist to form the pair. Thus $\hat{\tilde{\Upsilon}}_k(\omega)$ can be written as

$$\hat{\tilde{\Upsilon}}_k(\omega) = \sum_{k=1}^{l} \left(\hat{\tilde{\Upsilon}}_{2k-1}(\omega) + \hat{\tilde{\Upsilon}}_{2k}(\omega)\right) = \sum_{k=1}^{l} \hat{\tilde{\Upsilon}}_{(2k-1,2k)} \tag{A.24}$$

where

$$\hat{\tilde{\Upsilon}}_{(2k-1,2k)} = \frac{C_{2k-1}}{s-\lambda_{2k-1}} + \frac{C_{2k}}{s-\lambda_{2k}} = \frac{A_{2k-1}s + A_{2k}}{(s+\alpha_k)^2+\beta_k^2} = \frac{iA_{2k-1}\omega + A_{2k}}{(i\omega+\bar{\alpha}\omega_{0k})^2+\omega_{0k}^2(1-\bar{\alpha}^2)} \tag{A.25}$$

The ω_{0k} is frequency used in the experiments and the coefficients A_{2k-1}, A_{2k} and damping $\bar{\alpha}$ are fitted to a set of impedance test. In practice, a set of Z_j (thus $\hat{\tilde{\Upsilon}}_j = \frac{2}{1+Z_j}$) are known at discrete frequencies ω_j. So with specified $\bar{\alpha}$, the A_{2k-1}, A_{2k} can be determined.

The $\hat{\tilde{\Upsilon}}_j$ can be written as

$$\begin{aligned}
\hat{\tilde{\Upsilon}}_j &= \sum_{k=1}^{l} \frac{i\omega_j A_{2k-1} + A_{2k}}{(i\omega_j+\alpha_k)^2+\beta_k^2} \\
&= \sum_{k=1}^{l} \frac{i\omega_j A_{2k-1} + A_{2k}}{\alpha_k^2+\beta_k^2-\omega_j^2+i2\omega_j\alpha_k} \\
&= \sum_{k=1}^{l} \frac{i\omega_j A_{2k-1} + A_{2k}}{\alpha_k^2+\beta_k^2-\omega_j^2+i2\omega_j\alpha_k} \frac{\alpha_k^2+\beta_k^2-\omega_j^2-i2\omega_j\alpha_k}{\alpha_k^2+\beta_k^2-\omega_j^2-i2\omega_j\alpha_k}
\end{aligned} \tag{A.26}$$

thus

$$\begin{bmatrix} \mathrm{Re}(\hat{\tilde{\Upsilon}}_j)) \\ \mathrm{Im}(\hat{\tilde{\Upsilon}}_j) \end{bmatrix} = F \begin{bmatrix} B_{1,1} & B_{1,2} & \cdots & B_{1,2l} \\ B_{2,1} & B_{2,2} & \cdots & B_{2,2l} \end{bmatrix} \begin{bmatrix} A_1 \\ \vdots \\ A_{2l} \end{bmatrix} \tag{A.27}$$

where

$$\begin{aligned}
F &= \frac{1}{(\alpha_k^2+\beta_k^2-\omega_j^2)^2+4\omega_j^2\alpha_k^2} \\
B_{1,2k-1} &= 2\omega_j^2\alpha_k \\
B_{1,2k} &= \alpha_k^2+\beta_k^2-\omega_j^2 \\
B_{2,2k-1} &= (\alpha_k^2+\beta_k^2-\omega_j^2)\omega_j \\
B_{2,2k} &= -2\omega_j^2\alpha_k
\end{aligned} \tag{A.28}$$

One discrete $\hat{\tilde{\Upsilon}}_j$ corresponds to two equations. So a total of l discrete $\hat{\tilde{\Upsilon}}_j$ is needed. In practical calculation the number of $\hat{\tilde{\Upsilon}}_j$ (l) is usually given and we need to calculate $2l$ coefficient from A_1 to A_{2l}.

After the determination of the value of A_{2k-1}, A_{2k}, we can get the time domain

formula

$$\Upsilon(t) = \begin{cases} i \sum_{k=1}^{l} \text{residue}\left[\hat{\Upsilon}(\omega), \omega_{2k-1}\right] e^{i\omega_{2k-1}t} + \text{residue}\left[\hat{\Upsilon}(\omega), \omega_{2k}\right] e^{i\omega_{2k}t} & t \geq 0 \\ 0 & t < 0 \end{cases} . \tag{A.29}$$

From Equation A.24, the poles of $\hat{\Upsilon}(\omega)$ are the sum of poles of $\frac{A_{2k-1}s+A_{2k}}{(s+\alpha_k)^2+\beta_k^2}$. That is

$$\begin{aligned} & \frac{i\omega A_{2k-1} + A_{2k}}{(i\omega + \alpha_k)^2 + \beta_k^2} \\ &= \frac{1}{i} \frac{\omega A_{2k-1} - iA_{2k}}{(\omega - i\alpha_k)^2 - \beta_k^2} \\ &= \frac{1}{i} \frac{\omega A_{2k-1} - iA_{2k}}{(\omega - \omega_{2k-1})(\omega - \omega_{2k})} \end{aligned} \tag{A.30}$$

where

$$\begin{aligned} \omega_{2k-1} &= i\alpha_k + \beta_k \\ \omega_{2k} &= i\alpha_k - \beta_k \\ \omega_{2k-1} - \omega_{2k} &= 2\beta_k \end{aligned} \tag{A.31}$$

thus

$$\begin{aligned} & i^* \text{residue}\left[\hat{\Upsilon}(\omega), \omega_{2k-1}\right] e^{i\omega_{2k-1}t} \\ &= H(t) \frac{\omega_1 A_{2k-1} - iA_{2k}}{\omega_1 - \omega_2} e^{i\omega_{2k-1}t} \\ &= H(t) \frac{1}{2\beta_k} \left[(\alpha_k i + \beta_k) A_{2k-1} - iA_{2k}\right] e^{(-\alpha_k + i\beta_k)t} \\ &= H(t) \frac{1}{2\beta_k} e^{-\alpha_k t} (i\alpha_k A_{2k-1} + \beta_k A_{2k-1} - iA_{2k})(\cos\beta_k t + i \sin\beta_k t) \end{aligned} \tag{A.32}$$

thus

$$\begin{aligned} & \text{residue}\left[\hat{\Upsilon}(\omega), \omega_{2k-1}\right] e^{i\omega_{2k-1}t} + \text{residue}\left[\hat{\Upsilon}(\omega), \omega_{2k}\right] e^{i\omega_{2k}t} \\ &= H(t) e^{-\alpha_k t} \left[A_{2k-1} \cos(\beta_k t) + \frac{A_{2k} - \alpha_k A_{2k-1}}{\beta_k} \sin(\beta_k t)\right] . \end{aligned} \tag{A.33}$$

Using the recursive formula

$$\tilde{\Upsilon}_{(2k-1,2k)}(t) = H(t) \frac{\omega_{2k-1} A_{2k-1} - iA_{2k}}{\omega_{2k-1} - \omega_{2k}} e^{i\omega_{2k-1}t} + H(t) \frac{\omega_{2k} A_{2k-1} - iA_{2k}}{\omega_{2k} - \omega_{2k-1}} e^{i\omega_{2k}t} \tag{A.34}$$

thus

$$\mu_{2k-1} = \frac{\omega_{2k-1}A_{2k-1} - iA_{2k}}{2\beta_k} = \frac{\beta_k A_{2k-1} + i(\alpha_k A_{2k-1} - A_{2k})}{2\beta_k}$$
$$\mu_{2k} = -\frac{\omega_{2k}A_{2k-1} - iA_{2k}}{2\beta_k} = -\frac{\beta_k A_{2k-1} + i(\alpha_k A_{2k-1} - A_{2k})}{2\beta_k}, \tag{A.35}$$

$$\begin{aligned} u'^{-}(t) \quad &= u'^{+}(t) + \int_0^\infty \tilde{\Upsilon}(\tau)u'^{+}(t-\tau)d\tau \\ &= -u'^{+}(t) + \sum_{k=1}^{L} I_{2k-1}(t) + I_{2k}(t) \end{aligned} \tag{A.36}$$

where

$$I_{2k-1} = \mu_{2k-1}\frac{1}{2}\Delta t[u'^{+}(t) + e^{i\omega_{2k-1}\Delta t}u'^{+}(t-\Delta t)] + e^{i\omega_{2k-1}\Delta t}I_{2k-1}(t-\Delta t)$$
$$I_{2k} = \mu_{2k}\frac{1}{2}\Delta t[u'^{+}(t) + e^{i\omega_{2k}\Delta t}u'^{+}(t-\Delta t)] + e^{i\omega_{2k}\Delta t}I_{2k}(t-\Delta t) \tag{A.37}$$

Using this formula combined with the CAA method, the simulation of broadband noise impinged on the acoustic liner can be performed efficiently as compared to the frequency domain method which can only solve one frequency in one calculation.

Appendix B

Validation of TDIBC

In this appendix the validation of the time domain impedance boundary condition is presented. Three specific problems are considered: the Gaussian pulse reflected in a normal-incident tube, the Gaussian pulse reflected on an impedance plane and the plane wave propagating along a partially acoustic treated duct. In all the cases, sound propagation obey the LEE which is solved using the sixth-order prefactored compact scheme [19] and LDDRK [21].

B.1 Wave in Normal-Incident Tube

First we will consider an initial value problem associated with the normal-incidence impedance tube [61]. For this case, the sound field is considered as one dimensional. An initial pulse is first introduced in the tube, then the wave will propagate obeying the one dimensional LEE without mean flow

$$\frac{\partial}{\partial t}\begin{bmatrix} u' \\ p' \end{bmatrix} + \frac{\partial}{\partial x}\begin{bmatrix} p' \\ u' \end{bmatrix} = 0. \tag{B.1}$$

The initial condition is

$$u' = 0, \qquad p' = \exp[-0.0044(x - 83.333)^2]\cos[0.444(x - 83.333)] \tag{B.2}$$

where the reference length is 0.012 m and the reference speed is the 340 m/s. This choice of initial conditions ensures that the centre of the acoustic spectrum of the incident wave has a frequency of 2 kHz and a spectrum half-width of 0.5 kHz. A uniformly spaced 151 grids is used which has at least seven points per wavelength for frequencies up to 4.0 kHz and the impedance boundary condition was applied at the left end of the computation zone. Figure B.1 shows the computed pressure distribution at time $t = 60.1$. at this time the right half of the initial pulse is

about to exit the computation domain, whereas the left half of the pulse is about to impinge on the surface of the treatment panel. Figure B.2 shows the reflected pulse propagating away from the impedance boundary of the tube at $t = 140.1$. The amplitude of the reflected pulse is considerably smaller than that of the incident pulse. Part of the acoustic energy is dissipated during the reflection process off the impedance surface. The exact frequency domain solution is represented by the square symbols. There is an excellent agreement between the numerical results and the exact solution. This is true in both the wave amplitude and phase.

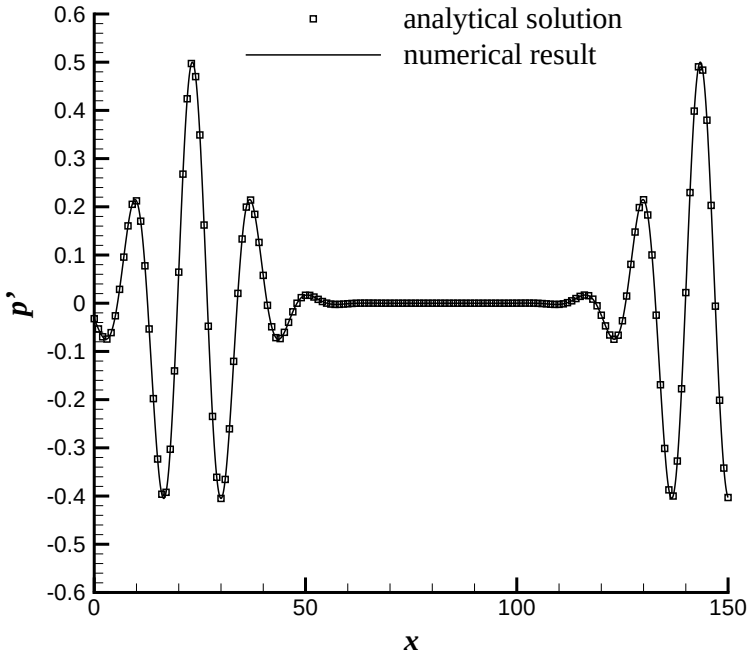

Figure B.1: Pressure wave form of the incident acoustic pulse inside the normal-incidence impedance tube at t=60.1.

B.2 Gaussian Pulse Over Impedance Plane

In this problem, a three dimensional case of a Gaussian pulse over impedance plane without mean flow effect is considered [63]. In the calculation, all the length scales are non-dimensionalized by a reference length of 1 m, velocities are non-dimensionalized by $c^* = 340$ m/s, density is non-dimensionalized by $\rho^* = 1.225$ kg/m^3, pressure is non-dimensionalized by $\rho^* c^{*2}$ and impedance is non-dimensionalized by $\rho^* c^*$. As shown in Figure B.3, the impedance plane lies on $z = 0$, while an initial

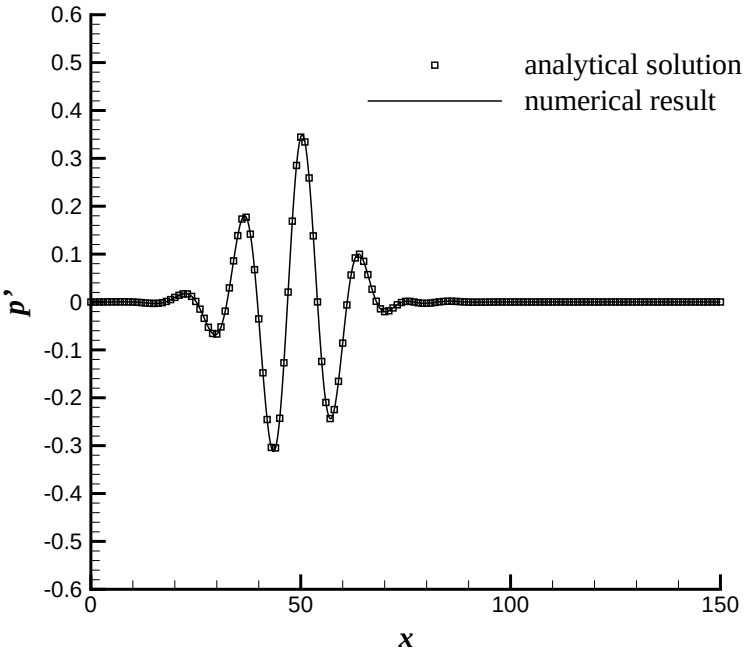

Figure B.2: Pressure wave form of the incident acoustic pulse inside the normal-incidence impedance tube at t=140.1.

spherical Gaussian pulse is centered at $(0, 0, 30)$ which can be written as

$$\begin{cases} u' = 0 \\ p'(r) = e^{-Br^2} \end{cases} \tag{B.3}$$

where $r = \sqrt{x^2 + y^2}$ is the distance to the pulse center and B is a constant ($B = \frac{\ln 2}{25}$). The three parameters for the impedance model are chosen as $R_0 = 0.2$, $X_{-1} = -0.4758$ and $X_1 = 2.0938$.

Exact solution is obtained following the approach proposed by Zheng and Zhuang [63]. Their idea is straightforward. Since the impedance properties are given in frequency domain and in terms of planar waves, a broadband incident wave need to be decomposed into harmonic waves and a non-planar incident wave need to be decomposed in to planar waves. Then the refection of each of the harmonic planar incident wave can be determined. The total reflected wave is in a form of an integral of the reflected harmonic planar waves.

Figure B.4 shows the acoustic pressure along the z axis at $t = 30$. The asymmetry about $z = 30$, where the center of the initial spherical pulse lies, shows the effect of the impedance boundary. As shown in Figure B.4, the numerical result agree very well with the analytical solution, and thus the time-domain impedance boundary

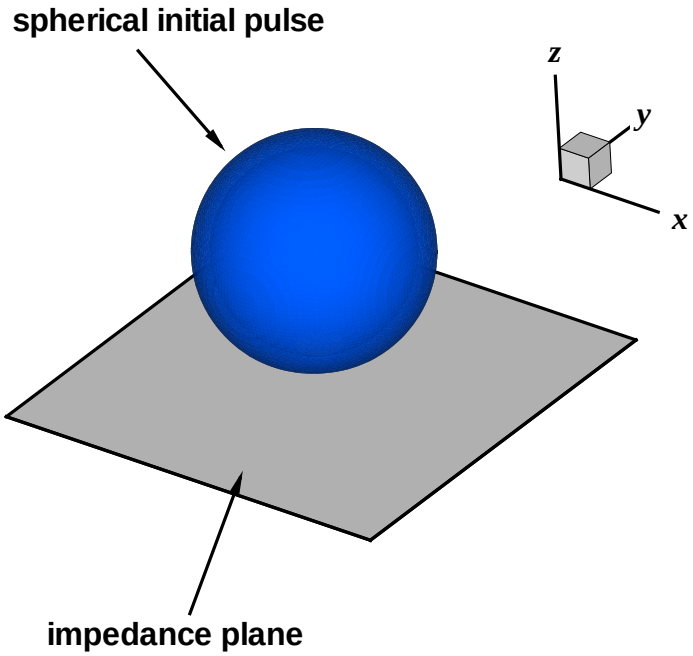

Figure B.3: Schematic of the 3D Gaussian pulse over an impedance plane

condition is verified.

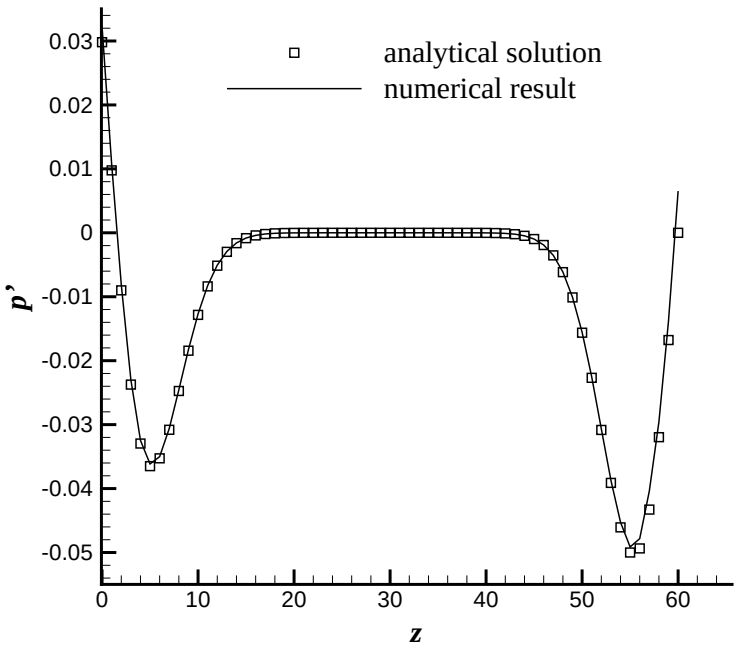

Figure B.4: Comparison of the acoustic pressure along the z axis at t=30.

B.3 Plane Wave in Lined Duct

The experimental data from the flow-impedance test laboratory of NASA Langley research centre [117] are used to validate our numerical method. The duct configuration for the experiment is shown in Figure B.5, where acoustic treatment is only applied in the middle section of the lower wall. The first cut off frequency based on the tube height without flow is 3.287 kHz. The sound fields in the range of exciting frequency f from 0.5 to 3 kHz are expected to be mainly one-dimensional, and incident waves at 90 degrees grazing the impedance wall are assumed.

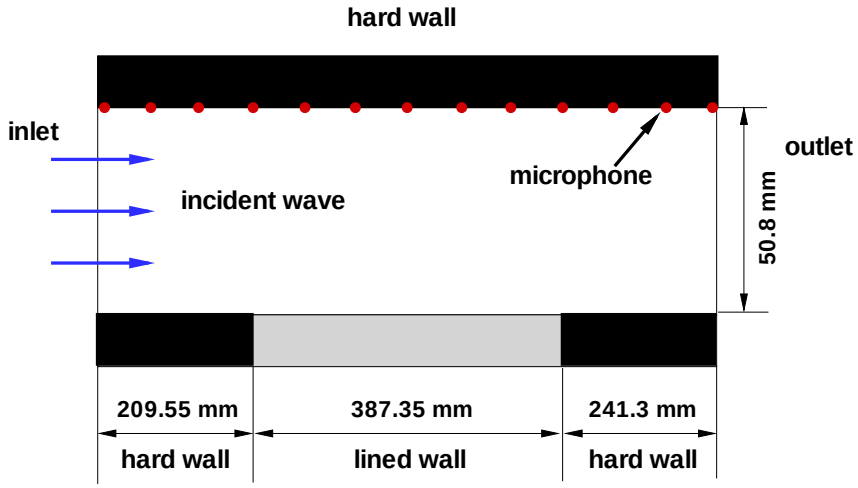

Figure B.5: Configuration of the NASA Langley flow-impedance tube.

The measured specific impedance values are listed in Table B.1. Both the narrowband and broadband formula were used in the validation [69]. An incoming acoustic wave $p_0 \sin[\omega(x - c_0 t)]$ is supplied at the inlet, where the amplitude p_0 is set such that the sound pressure level at the inlet is the same as that from the experiment. A buffer zone condition is applied at the exit of the duct. For the case with mean flow, the effective plane-wave impedance $Z_{eff} = Z(1 + M_0 \sin\theta)$ was used to replace the impedance Z, where M_0 is mean flow Mach number, $\theta = \sin^{-1}[k_x/(\omega - k_x M_0)]$ is effective incident wave angle and k_x is the wavenumber in mean flow direction. For sake of brevity, the results of 1000Hz, 2000Hz and 3000Hz are shown. In the legend, B1 means the results obtained using broadband formula 1 of the TDIBC; B2 means the results obtained using broadband formula 2 of the TDIBC. M.0 means the results of $M = 0$; M.1 means the results of M=0.1; M.3 means the results of M=0.3. 1000 means the results of 1000 Hz; 2000 means the results of 2000 Hz; 3000 means the results of 3000 Hz. The solid and dashed lines represent the numerical

results and the square symbol indicates the experimental data.

Frequency, kHz	**Impedance**
0.5	0.41-1.56i
1.0	0.46+0.03i
1.5	1.08+1.38i
2.0	4.99+0.25i
2.5	1.26-1.53i
3.0	0.69-0.24i

Table B.1: Impedance data of a constant depth ceramic tubular liner [66].

No-Flow Case

Figures B.6 to B.8 show the comparison of the upper wall sound pressure level (SPL) results of the current calculations of no-flow case with the measured data.

M=0.1 Case

Figures B.9 to B.11 show and compare the numerical results of M=0.1 case with experimental data.

M=0.3 Case

Figure B.12 to B.14 show and compare the numerical results of M=0.3 case with experimental data.

In general, the agreements between the numerical results and the experimental measurements are good. The discrepancy near the exit is partly due to the fact that radiation boundary condition is applied while there is a small exit impedance value.

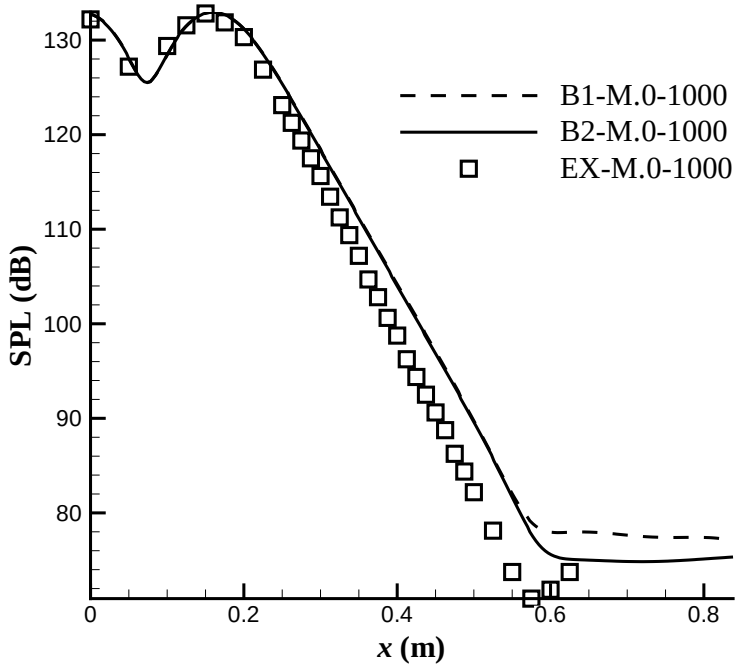

Figure B.6: Comparison of experimental data and numerical results: f=1000Hz, M=0.

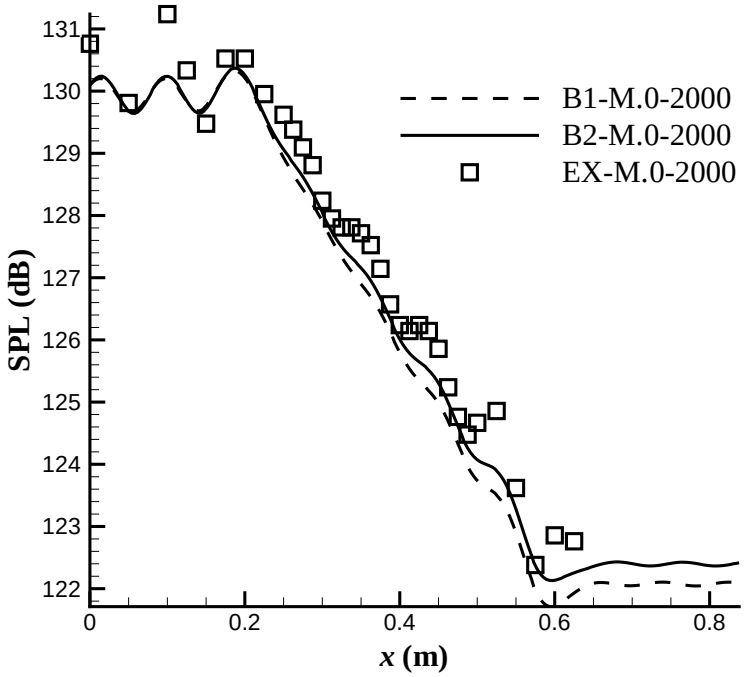

Figure B.7: Comparison of experimental data and numerical results: f=2000Hz, M=0.

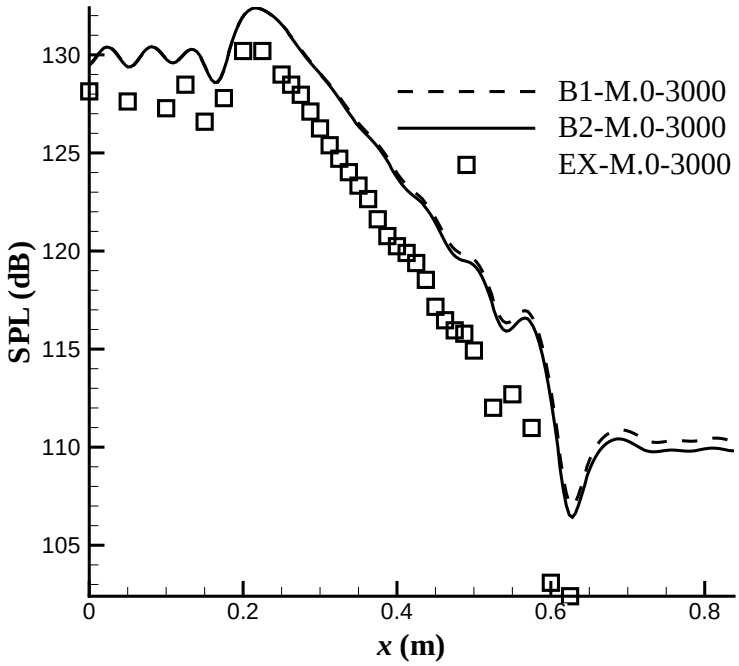

Figure B.8: Comparison of experimental data and numerical results: f=3000Hz, M=0.

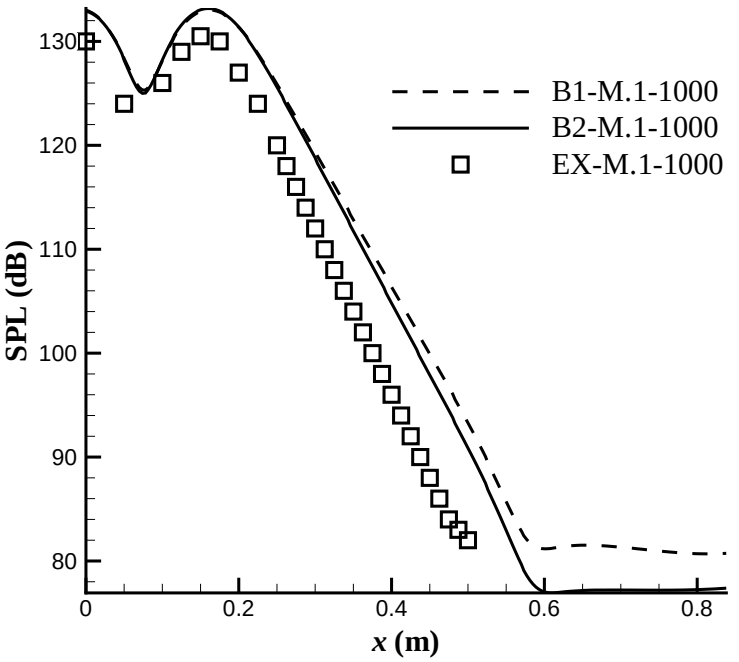

Figure B.9: Comparison of experimental data and numerical results: f=1000Hz, M=0.1.

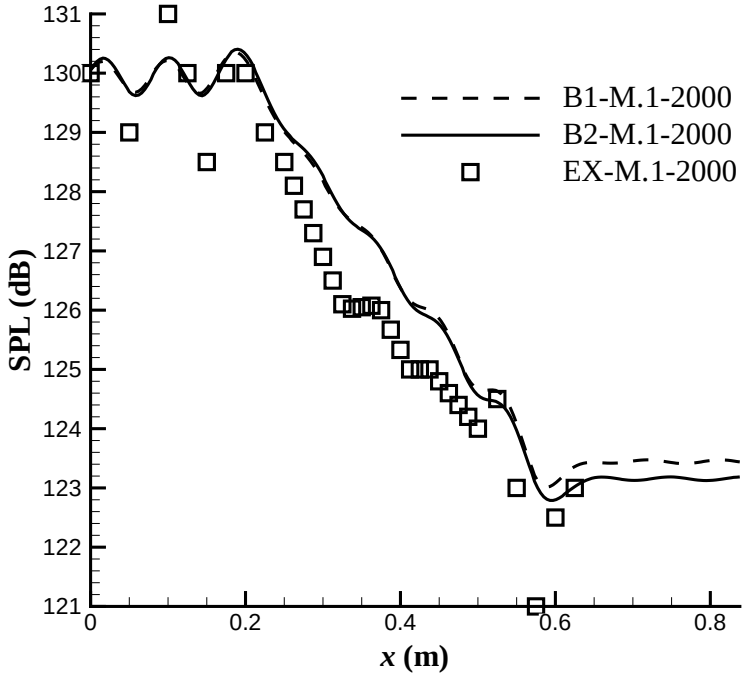

Figure B.10: Comparison of experimental data and numerical results: f=2000Hz, M=0.1.

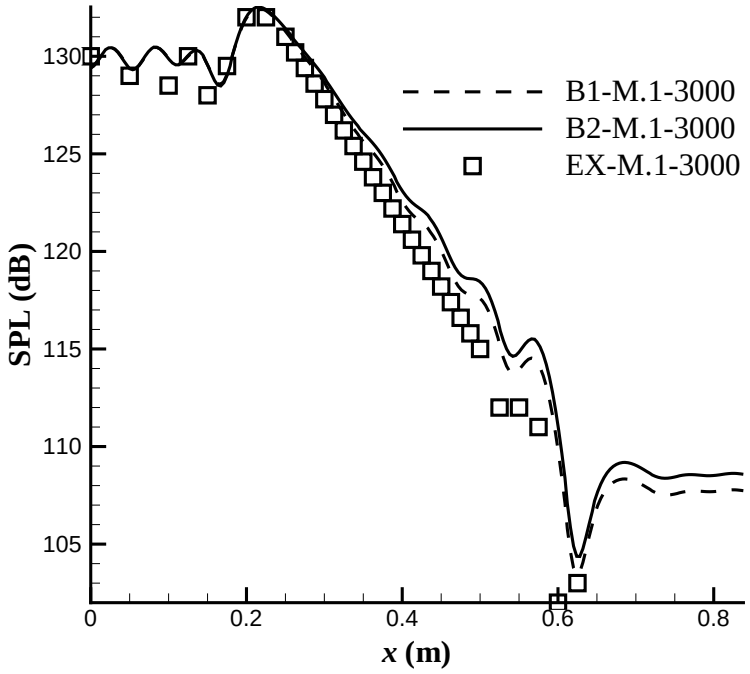

Figure B.11: Comparison of experimental data and numerical results: f=3000Hz, M=0.1.

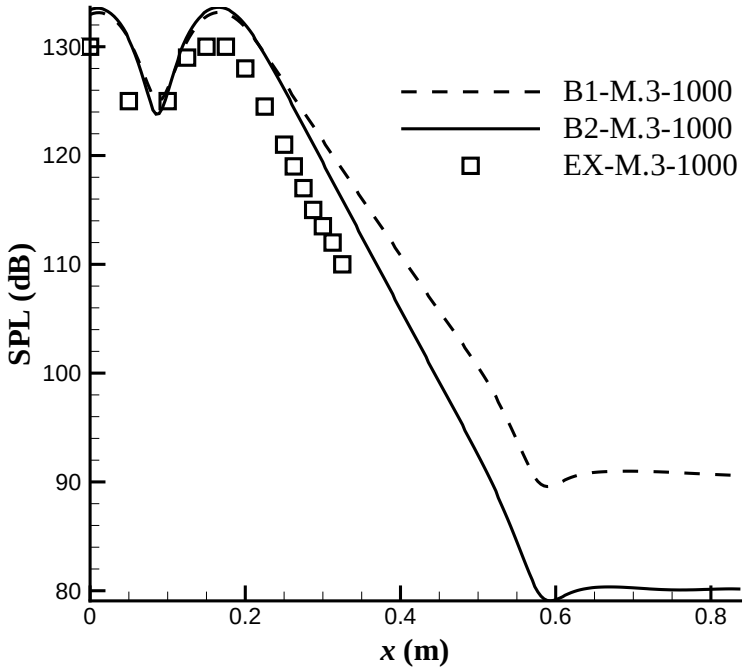

Figure B.12: Comparison of experimental data and numerical results: f=1000Hz, M=0.3.

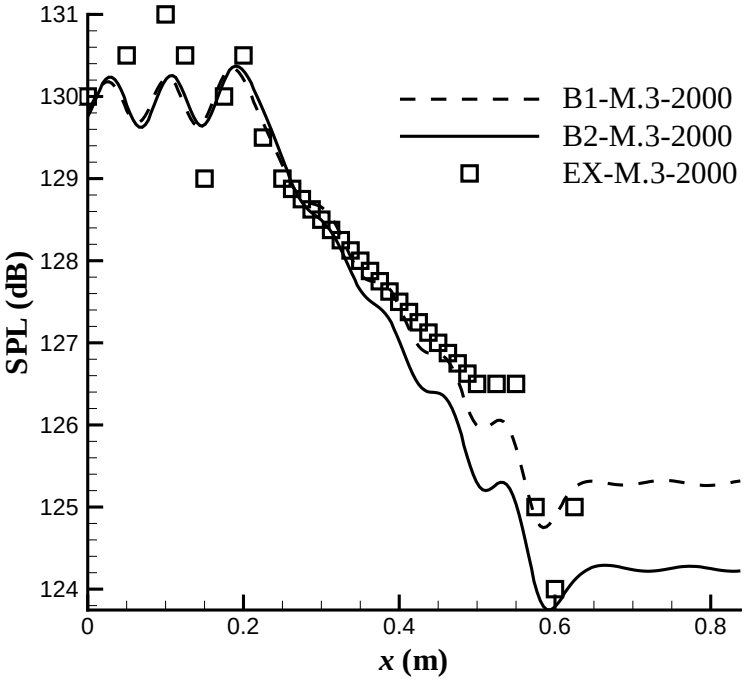

Figure B.13: Comparison of experimental data and numerical results: f=2000Hz, M=0.3.

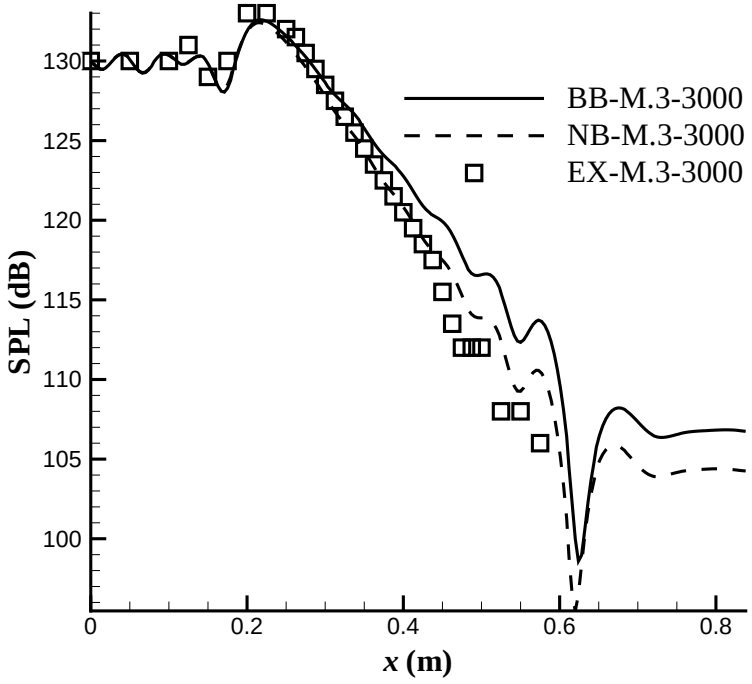

Figure B.14: Comparison of experimental data and numerical results: f=3000Hz, M=0.3.

Appendix C

Validation of FW-H Acoustic Code

In this appendix the validation the Ffowcs Williams and Hawkings acoustic code is presented. The problems chosen to demonstrate the accuracy and robustness of the acoustic code are: the noise radiated by a monopole, and the noise generated by viscous flow past a circular cylinder.

C.1 Monopole

The acoustic field from a monopole source is computed in the far field using the FW-H acoustic code. The complex potential for the monopole flow is given in [118] as

$$\phi(x, y, z, t) = A\frac{1}{4\pi r}\exp^{i(\omega t - kr)} \tag{C.1}$$

where $r = \sqrt{x^2 + y^2 + z^2}$ is the distance between the source and observer. The real parts of $p' = -\rho_0 \partial\phi/\partial t$, $u' = \partial\phi/\partial x$, $v' = \partial\phi/\partial y$, $w' = \partial\phi/\partial z$, and $\rho' = p'/c_0^2$ are used as the variables in the FW-H equation. The flow variables evaluated over four periods on the surface are used as the source terms in the FW-H equation. For this case, $\omega = 4\pi/46$, $A = 0.1$ and the integration surface is a cube that extends from -5 to 5 in all three coordinate directions. Uniformly spaced cells with 50×50 grids are used on each face of the cube. A comparison of the computed pressure time-history at (50,0,0) was given in Figure C.1. The agreement is very well and identical results are obtained for all other observer positions.

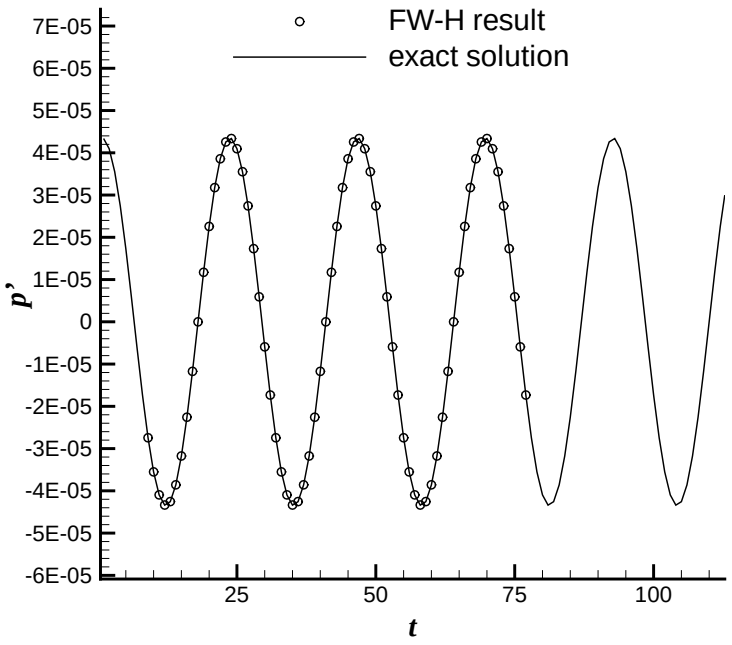

Figure C.1: Time history comparison for a stationary monopole.

C.2 Circular Cylinder in Viscous Flow

In this validation case, the CAA code using the 6th-order compact scheme and the 4th-order Runge-Kutta method is used to obtain the highly nonlinear near field of a circular cylinder in viscous flow. An explicit form of buffer zone boundary conditions was used as the non-reflecting boundary condition and the far field noise generated by the shedding of vorticity off the circular cylinder are calculated using FW-H solver and CAA solver respectively. The free stream Mach number is 0.2, the Reynolds number based on the diameter (D) of the cylinder is 90,000. Angle of attack is 0 degree. The grids extend to $30D$ in all direction and 357 grid points are used in the azimuthal direction and 275 grid points are used in the radial direction. The grid density is carefully chosen so that there are at least 12 PPW at $20D$ from the cylinder. Buffer zones of 10 grid points in radial direction are used. In the calculation, all the length scales are non-dimensionalized by the diameter of the cylinder, velocities are non-dimensionalized by $c^* = 340$ m/s, density is non-dimensionalized by $\rho^* = 1.225$ kg/m^3 and pressure is non-dimensionalized by $\rho^* c^{*2}$. The first grid size off the wall is 3.0×10^{-4} and the time step size is 1.0×10^{-4}. The vortex shedding period is about 19.4 corresponding to 1.94×10^5 time steps. Eight 2.2 GHz AMD Opterons CPUs on the iridis2 cluster of University of Southampton are

used to perform the calculation. On this cluster, every one period calculation of this case needs 20 hours CPU time. The predicted Strouhal number 0.25 is overpredicted compared with the experiment results [119]. In ref [119], similar overprediction is found and the author proposes that it is due to the onset of three-dimensional effects.

The farfield directivity is calculated using the FW-H solver. The observers are on a circle with a radius of $20D$ at z=0 plane and the origin is located at (0, 0, 0). Different integration surfaces are used to test the integration surface sensitivity as shown in Figure C.2 where the solid line denotes the cylinder wall, the dashed line denotes a circle with a radius of 1 diameter, the dashed-dot line is a circle with a radius of 1.5 diameters. The integration surfaces are generated by extruding these circles from $-5D$ to $5D$ in spanwise direction.

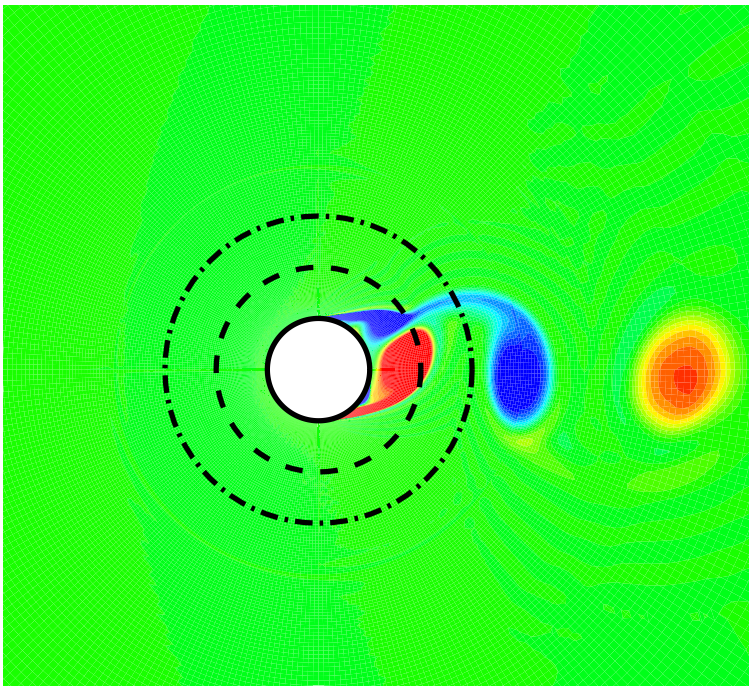

Figure C.2: Different integration surfaces.

The calculated results are shown in Figure C.3, where the SPL of observer points are plotted in polar coordinates. The angle (θ) is defined as 0 degree along freestream direction and increase anti-clockwise. The SPL is given in dB and the discrepancy of the results is less than 1 dB for most of the angles. The good agreement of the results for the three different integration surfaces indicate that for the case studied the quadrupole term is negligible and the FW-H results are not sensitive to the position of integration surface [119].

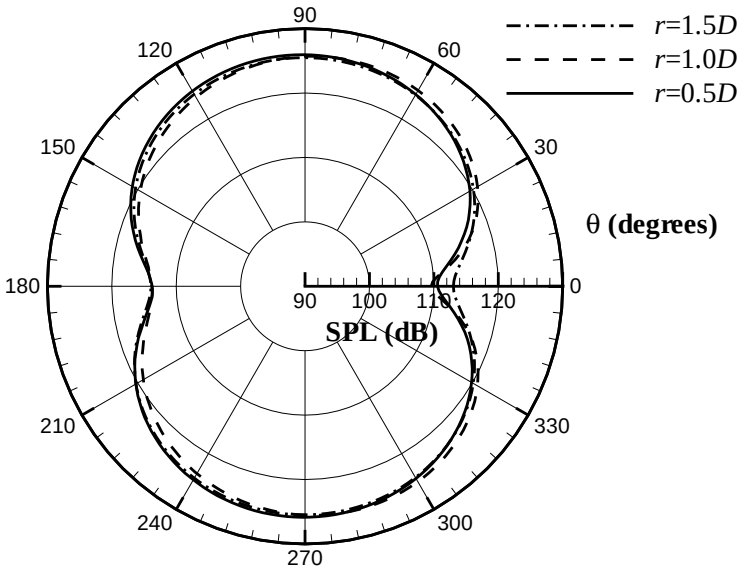

Figure C.3: Comparison of the FW-H results obtained using different integration surfaces for circular cylinder calculation.

The effect of spanwise length of the integration surface on the predicted results is investigated. The Figure C.4 shows the calculated SPL at the point $20D$ above the center of the cylinder. Results show that the predicted value has a strong dependence on the correlation length up to a spanwise length scale of $20D$, at which point the peak noise level begins to converge.

The FW-H result obtained using the integration surface with a radius of $0.5D$ and a spanwise length of $70D$ is compared with the directly calculated CAA result in Figure C.5. FW-H result and CAA result agree well far away from the wake. In the down stream direction, the CAA result show the influence of the aerodynamic unsteadiness and the prediction gives higher SPL values.

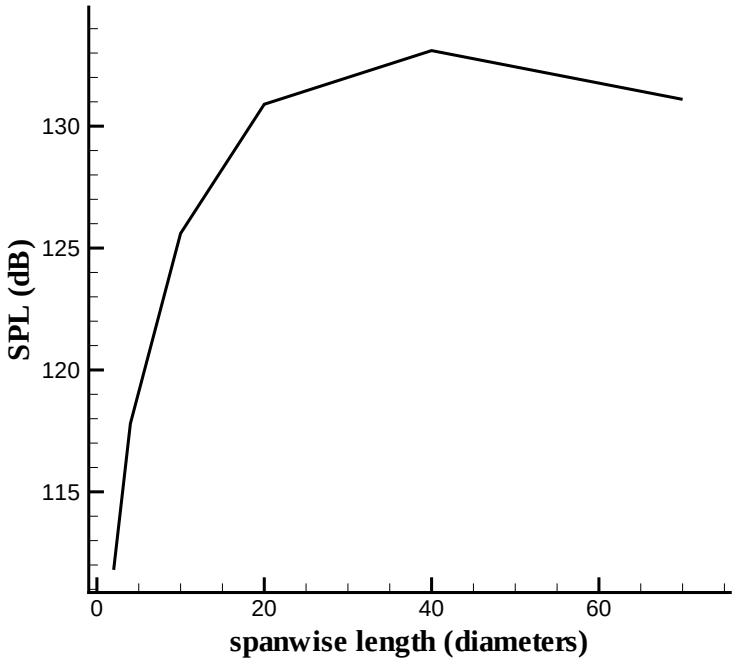

Figure C.4: Spanwise length effects on FW-H results of the circular cylinder.

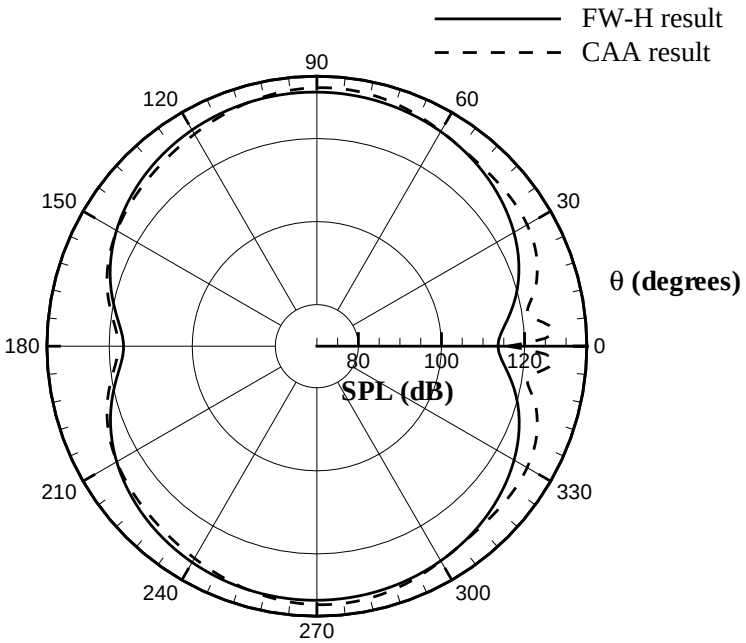

Figure C.5: Comparison between the FW-H result and CAA result

Appendix D

Validation of Implicit Temporal Integration Scheme

In this appendix the accuracy and efficiency of the time-implicit high-order compact difference approach is validated using the inviscid and viscous cases on Cartesian and curvilinear meshes. To show the benefits of the time-implicit sixth order compact difference (scheme A), two other approaches are considered and the results obtained using different approaches are compared. The two other approaches are: time-implicit third order MUSCL based scheme (scheme B) and time-explicit sixth order compact difference scheme (scheme C). The implicit temporal scheme used is the second order LU-SGS method with the Newton-like subiteration and the explicit temporal scheme used is the forth order Runge-Kutta method.

D.1 Advection of Vortical Disturbance

The first case considered is the advection of a vortex in an inviscid flow. This is a good case to test the capabilities of the different schemes to accurately simulate the advection of vortical structures as needed in direct and large-eddy simulations. In the calculation a vortex located at (x_c, y_c) is imposed to the uniform flow by giving the following initial condition [22]:

$$\begin{aligned} u &= u_\infty - \frac{S(y-y_c)}{r_0^2}\exp\frac{-r^2}{2} \\ v &= \frac{S(x-x_c)}{r_0^2}\exp\frac{-r^2}{2} \\ p_\infty - p &= \frac{\rho S^2}{2r_0^2}\exp(-r^2) \\ r^2 &= \frac{(x-x_c)^2+(y-y_c)^2}{r_0^2} \end{aligned} \tag{D.1}$$

where u, v, p, and r_0 denote the Cartesian velocity components, static pressure and vortex core radius, respectively. The freestream Mach number was chosen to be 0.1 and the vortex strength parameter S was chosen to be 0.2. The density was assumed constant in the calculation.

To examine the spatial accuracy of the proposed scheme A, the Euler equations were solved on a Cartesian mesh with three different levels of spatial resolution ($\Delta x/r_0 = \Delta y/r_0 = 0.4, 0.2$ and 0.1). In this first test cast, only the spatial accuracy will be examined so a small time step size of $\Delta t c_\infty/r_0 = 0.002$ was used which corresponds to a CFL number of 0.005, 0.01 and 0.02 on the three meshes respectively. The number of subiteration used in scheme A is 3.

Figure D.1 shows the vorticity magnitude contours calculated using different schemes and derived from exact solution after the vortex convected a period of $tc_\infty/r_0 = 10$. The results shown are on the second grid ($\Delta x/r_0 = \Delta y/r_0 = 0.2$). Both the results of scheme A and that of scheme C show that the vortical structures are accurately advected compared to the exact solution. The vertex calculated using scheme B keeps the symmetrical shape however it dissipates. A further comparison was made on the vorticity magnitude on the horizontal line passing through the vortex center line. Figure D.2 shows that the results of scheme A and scheme C are almost identical and agree very well with the exact solution while Scheme B shows significant dissipation.

The order of accuracy of the different schemes was obtained by linear least square fitting the maximum error (E_{rr}) of the calculated swirl velocity along the horizontal line through the vortex center on different grid. The order of accuracy is 5.33, 2.73 and 5.67 for scheme A, B and C. They are close to the expected formal accuracy of the discretization schemes and the small disparity of the accuracy between scheme A and scheme C is due to the different time integration. This case shows that for the given level of accuracy, the necessary gird resolution will be significantly reduced by using the higher order scheme which could result in a saving of calculation time especially for 3D case.

D.2 Unsteady Flow past a Circular Cylinder

The first test case show that the scheme C has the best performance in term of the accuracy. However the explicit scheme C has to satisfy the CFL criteria which confined its application in the wall bounded case in which a small grid space need to be used near the wall. The scheme A uses the implicit time integration method which makes the use of larger CFL number possible and results in a significant

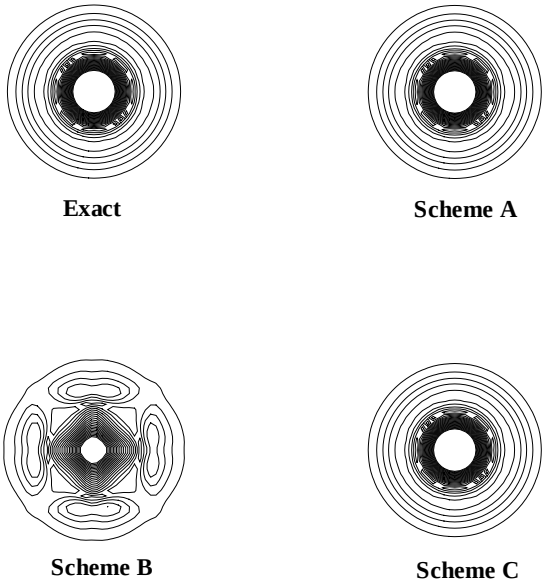

Figure D.1: Vorticity magnitude contours obtained using the different schemes.

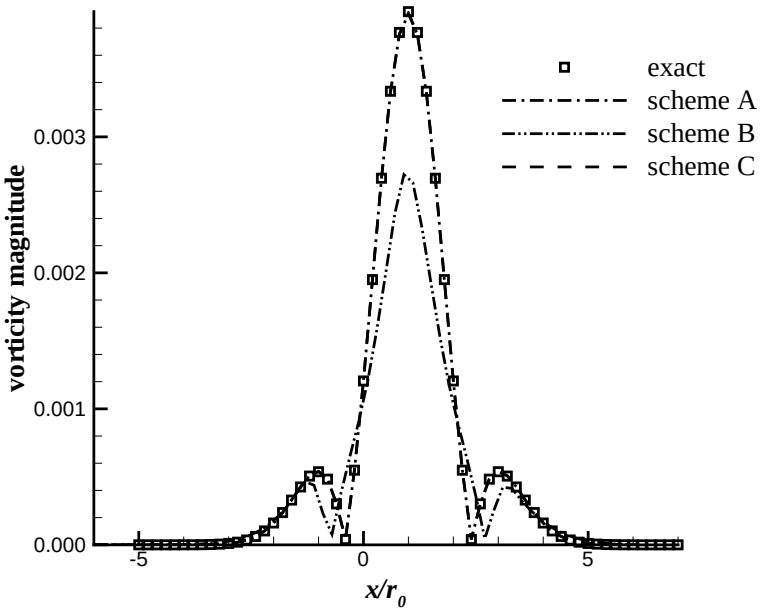

Figure D.2: Comparison of the vorticity magnitude along the center line obtained using the different schemes.

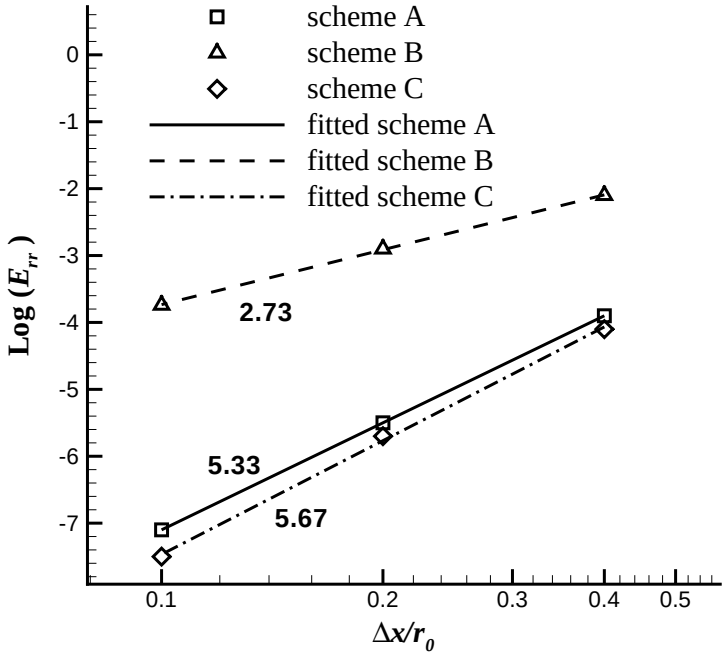

Figure D.3: Comparison of the accuracies of the different schemes.

improvement on the calculation efficiency of wall bounded case.

In this case the accuracy and efficiency of the scheme A are tested using the viscous flow pasting a circular cylinder. The Reynolds number based on the cylinder's diameter and upstream velocity is chosen as 150 to avoid the three dimensional behavior in the wake.The upstream Mach number is 0.33 and the cylinder diameter (D) is 2×10^{-5} m. A O-grid of size 500×299 is employed with the first grid step away from the wall of 0.01D and the computational domain has a radius of 150D from the center of the cylinder. Both scheme A and scheme C are used to calculate the vortex shedding phenomenon. For scheme A, a $\Delta t c_\infty / D = 0.1$ corresponding to a CFL of 10 is used with 4 subiterations and the using of more subiterations has insignificant improvement of the results. For scheme C, a $\Delta t c_\infty / D = 0.005$ corresponding to a CFL of 0.5 is used.

Figure D.4 shows the computed vortex street behind the cylinder where the vorticity is non-dimensionalized by the diameter of the cylinder and the freestream speed of sound. The two schemes give similar results although the CFL of the scheme A are 20 times larger than the scheme C. The Strouhal number obtained using scheme A is 0.178 and the Strouhal number calculated using scheme C is 0.184. Both of the schemes show a good agreement with the experimental data [120, 121] and numerical studies [122, 123, 124], and the results obtained by scheme C is better

as it has higher accuracy which was shown in section D.1. In the case studied for 1 subiteration of the scheme A it takes 0.667 of the CPU time needed for scheme C to run 1 step therefore for a given physical time, the scheme A is 7.5 times faster than the scheme C which makes the scheme A a superior tool to investigate the wall bounded complex flows.

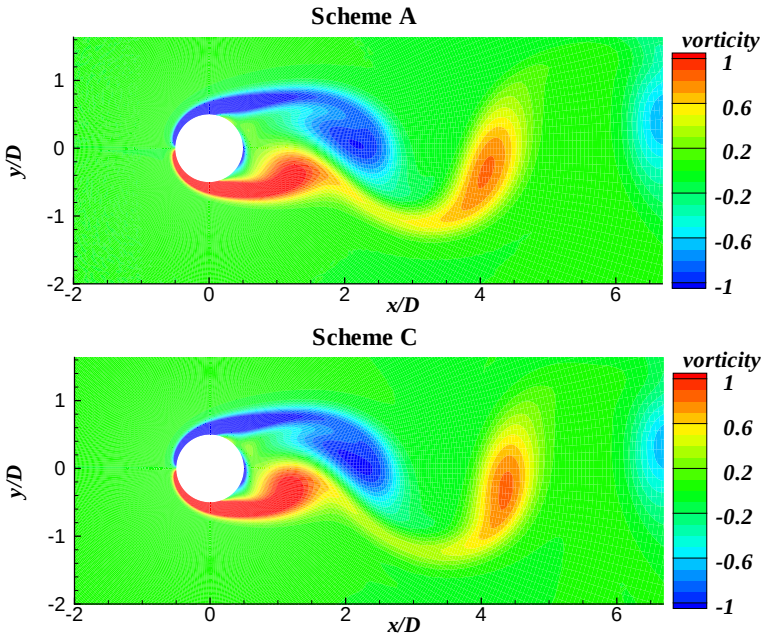

Figure D.4: Computed vortex shedding behind cylinder at $Re_D = 150$.

Bibliography

[1] Pacull, M., "Transport Aircraft Noise Reduction Technologies", presented at an International Symposium organized by the AAAF: "Which Technologies For Future Aircraft Noise Reduction?", Arcachon, France, October 2002.

[2] Khorrami, M.R., Choudhari, M. M., Singer, B.A., Lockard, D.P., and Streett, C.L., "In Search of the Physics: The Interplay of Experiment and Computation in Slat Aeroacoustics", AIAA Paper 2003–0980, 41^{st} *Aerospace Sciences Meeting*, Reno, NV, U.S.A., January 2003.

[3] Davy, R., and Remy, H., "Airframe Noise Characteristics of a 1/11 Scale Airbus Model", AIAA Paper 98–2335, 4^{th} *AIAA/CEAS Aeroacoustics Conference*, Toulouse, France, June 1998.

[4] Dobrzynski, W., Nagakura, K., Gehlhar, B., and Buschbaum, A., "Airframe Noise Studies on Wings with Deployed High-Lift Devices", AIAA Paper 98–2337, 4^{th} *AIAA/CEAS Aeroacoustics Conference*, Toulouse, France, June 1998.

[5] Guo, Y.P., and Joshi, M.C., "Noise Characteristics of Aircraft High Lift Systems", *AIAA Journal*, Vol. 41, No. 7, July 2003, pp. 1247–1256.

[6] Tam, C.K.W., "Jet Noise: Since 1952", *Theoret. Comput. Fluid Dynamics*, , No. 10, 1998, pp. 393–405.

[7] Brentner, K.S., and Farassat, F., "Modeling Aerodynamically Generated Sound of Helicopter Rotors", *Progress in Aerospace Sciences*, Vol. 39, 2003.

[8] Lighthill, M.J., "On Sound Generated Aerodynamically, I: General Theory", *Proceedings of the Royal Society of London*, Vol. A211, 1952, pp. 564–587.

[9] Lighthill, M.J., "On Sound Generated Aerodynamically, II: Turbulence as a Source of Sound", *Proceedings of the Royal Society of London*, Vol. A222, 1954, pp. 1–32.

[10] Curle, N., "The Influence of Solid Boundaries upon Aerodynamic Sound", *Proceedings of the Royal Society of London*, Vol. A231, No. 1187, 1955, pp. 505–514.

[11] Ffowcs Williams, J.E., and Hawkings, D.L., "Sound Generated by Turbulence and Surfaces in Arbitrary Motion", *Philosophical Transactions of the Royal Society of London*, Vol. A264, No. 1151, 1969, pp. 321–342.

[12] Farassat, F., "Introduction to Generalized Functions with Applications in Aerodynamics and Aeroacoustics", NASA TP 3428, 1996.

[13] Tam, C.K.W., "Computatonal Aeroacoustics: Issues and Methods", *AIAA Journal*, Vol. 33, No. 10, October 1995, pp. 1788–1796.

[14] Tam, C.K.W., "Computational Aeroacoustics: An Overview of Computational Challenges and Applications", *International Journal of Computational Fluid Dynamics*, Vol. 18, No. 6, August 2004, pp. 547–567.

[15] Zingg, D.W., "A Review of High-Order and Optimized Finite-Difference Methods for Simulating Linear Wave Phenomena", AIAA Paper 97-2088, 1997.

[16] Tam, C.K.W., and Webb, J.C., "Dispersion-Relation-Preserving Finite Difference Schemes for Computational Acoustics", *Journal of Computational Physics*, Vol. 107, 1993, pp. 262–281.

[17] Wilson, R.V., Demuren, A.O., and Carpenter, M., "High-Order Compact Schemes for Numerical Simulation of Incompressible Flows", NASA CR 1998-206922, 1998.

[18] Hixon, R., "A New Class of Compact Schemes", AIAA Paper 1998–0367, 1998.

[19] Hixon, R., "Prefactored Small-Stencil Compact Schemes", *Journal of Computational Physics*, Vol. 165, 2000, pp. 522–541.

[20] Ashcroft, G., and Zhang, X., "Optimized Prefactored Compact Schemes", *Journal of Computational Physics*, Vol. 190, 2003, pp. 459–477.

[21] Hu, F.Q., Hussaini, M.Y., and Manthey, J.L., "Low-dissipation and low-dispersion Runge-Kutta Schemes for Computational Acoustics", *Journal of Computational Physics*, Vol. 124, 1996, pp. 177–191.

[22] Visbal, M.R. and Gaitonde, D. V., "High-Order-Accurate Methods for Complex Unsteady Subsonic Flows", *AIAA Journal*, Vol. 37, No. 10, 1999, pp. 1231–1239.

[23] Visbal, M.R. and Gaitonde, D. V., "On the Use of Higher-Order Finite-Difference Schemes on Curvilinear and Deforming Meshes", *Journal Computational Physics*, Vol. 181, 2002, pp. 155–185.

[24] Freund, J.B., "Acoustic Sources in a Turbulent Jet: A Direct Numerical Simulation Study", AIAA Paper 99–1858, 1999.

[25] Bogey, C., Bailly, C., and Juve', D., "Large Eddy Simulation of a Subsonic Jet: Direct Calculation of Its Radiated Sound Field", AIAA paper 2000–2009, Breckenridge, CO, U.S.A., June 2000.

[26] Bogey, C., Bailly, C., and Juve', D., "Computation of Flow Noise Using Source Terms in Linearized Euler's Equations", *AIAA Journal*, Vol. 40, No. 2, February 2002, pp. 235–243.

[27] Karweit, M., Blanc B.P., Juvé, D., Comte, B.G., "Simulation of the Propagation of an Acoustic Wave through a Turbulent Velocity Field: A Study of Phase Variance", *Journal of the Acoustical Society of America*, Vol. 89, No. 1, 1991, pp. 52–62.

[28] Ewert, R. and Bauer, M., "Towards the Prediction of Broadband Trailing Edge Noise via Stochastic Surface Sources", AIAA Paper 2004–2861, 10^{th} *AIAA/CEAS Aeroacoustics Conference*, 2004.

[29] Ewert, R. and Emunds, R., "CAA Slat Noise Studies Applying Stochastic Sound Sources Based on Solenoidal Digital Filters", AIAA Paper 2005–2862, 11^{th} *AIAA/CEAS Aeroacoustics Conference*, 2005.

[30] Khorrami, M.R., Berkman, M.E., and Choudhari, M., "Unsteady Flow Computations of a Slat with a Blunt Trailing Edge", *AIAA Journal*, Vol. 38, No. 11, November 2000, pp. 2050–2058.

[31] Singer, B.A., Lockard, D.P., and Brentner, K.S, "Computational Aeroacoustic Analysis of Slat Trailing-Edge Flow", *AIAA Journal*, Vol. 38, No. 9, 2000, pp. 1558–1564.

[32] Storms, B.L., Ross, J.C., Horne, W.C., Hayes, J.A., Dougherty, R.P., Underbrink, J.R., Scharpf, D.F., and Moriarty, P.J., "An Aeroacoustic Study

of an Unswept Wing With a Three-Dimensional High-Lift System", NASA TM-1998–112222, February 1998.

[33] Spalart, P.R., Jou, W.H., Strelets, M., and Allmaras, S.R., "Comments on the Feasibility of LES for Wings, and on a Hybrid RANS/LES Approach", *Advances in DNS/LES: First AFOSR International Conference on DNS/LES*, 1997.

[34] Billson, M., Eriksson, L., and Davidson, L., "Acoustic Source Terms for the Linearized Euler Equations in Conservative Form", *AIAA Journal*, Vol. 43, No. 4, April 2005, pp. 752–759.

[35] Lilley, G.M., "The Prediction of Airframe Noise and Comparison with Experiment", *Journal of Sound and Vibration*, Vol. 239, No. 4, January 2001, pp. 849–859.

[36] Choudhari, M.M., Lockard, D.P., Macaraeg, M.G., Singer, B.A., Streett, C.L., Neubert, G.R., Stoker, R.W., Underbrink, J.R., Berkman, M.E., Khorrami, M.R., and Sadowski, S.S., "Aeroacoustic Experiments in the Langley Low-Turbulence Pressure Tunnel", NASA TM-2002–211432, February 2002.

[37] Smith, M.G. and Chow, L.C., "Aerodynamic Noise Source on High Lift Slats and Flaps", AIAA Paper 2003–3226, 2003.

[38] Ma, Z., Smith, M., Richards, S.K. and Zhang, X., "Slat Noise Attenuation Using Acoustic Liners", AIAA Paper 2005–3009, 2005.

[39] Agarwal, A., and Morris, P.J., "Investigation of the Physical Mechanisms of Tonal Sound Generation by Slats", AIAA Paper 2002–2575, 8^{th} *AIAA/CEAS Aeroacoustics Conference*, Breckenridge, CO, U.S.A., June 2002.

[40] Olson, S., Thomas, F.O., and Nelson, R.C., "A Preliminary Investigation into Slat Noise Production Mechanisms in a High-Lift Configuration", AIAA Paper 2000–4508, 18^{th} *AIAA Applied Aerodynamics Conference*, Denver, CO, U.S.A., August 2000.

[41] Olson, S., Thomas, F.O., and Nelson, R.C., "Mechanisms of Slat Noise Production in a 2D Multi-Element Airfoil Configuration", AIAA Paper 2001–2156, 7^{th} *AIAA/CEAS Aeroacoustics Conference*, Maastricht, The Netherlands, May 2001.

[42] Khorrami, M.R., Singer, B.A., and Berkman, M.E., "Time-Accurate Simulatioins and Acoustic Analysis of Slat Free-Shear Layer", *AIAA Journal*, Vol. 40, No. 7, 2002, pp. 1281–1291.

[43] Paschal, K.B., Jenkins, L., and Yao, C-S., "Unsteady Slat Wake Characteristics of a 2-D High-Lift Configuration", AIAA Paper 2000–0139, 38^{th} *Aerospace Sciences Meeting*, Reno, NV, U.S.A., January 2000.

[44] Takeda, K., Ashcroft, G.B., Zhang, X., and Nelson, P.A., "Unsteady Aerodynamics of Slat Cove Flow in a High-Lift Device Configuration", AIAA Paper 2001–0706, 39^{th} *Aerospace Sciences Meeting*, Reno, NV, U.S.A., January 2001.

[45] Dobrzynski, W., and Herr, M., "Experimental Investigations in Low Noise Trailing Edge Design", AIAA Paper 2004–2804, 2004.

[46] Savory, E., Toy, N., Tahouri, B., and Dalley, S., "Flow Regimes in the Cove Regions Between a Slat and Wing and Between a Wing and Flap of a Multielement Airfoil", *Experimental Thermal and Fluid Science*, Vol. 5, No. 3, May 1992, pp. 307–316.

[47] Alemdaroglu, N., "Experimental Investigation of Flow around a Multielement Airfoil", *AGARD CP 515, High-Lift System Aerodynamics*, September 1993, pp. 2/1–19.

[48] Khorrami, M.R., Singer, B.A., and Berkman, M.E., "Time-Accurate Simulations and Acoustic Analysis of Slat Free-Shear Layer", AIAA Paper 2001–2155, 7^{th} *AIAA/CEAS Aeroacoustics Conference*, Maastricht, The Netherlands, May 2001.

[49] Menter, F.R., "Zonal Two-Equations $k-\omega$ Models for Aerodynamics Flows", AIAA Paper 93–2906, July 1993.

[50] Khorrami, M.R., Singer, B.A., and Lockard, D.P., "Time-Accurate Simulations and Acoustic Analysis of Slat Free-Shear Layer: Part 2", AIAA Paper 2002–2579, 8^{th} *AIAA/CEAS Aeroacoustics Conference*, Breckenridge, CO, U.S.A., June 2002.

[51] Deck, S., "Zonal-Detached-Eddy Simulation of the Flow Around a High-Lift Configuration", *AIAA Journal*, Vol. 43, No. 11, 2005, pp. 2372–2384.

[52] Choudhari, M. M., and Khorrami, M. R., "Slat Cove Unsteadiness: Effect of 3D Flow Structures", AIAA Paper 2006-0211, 44^{th} *AIAA Aerospace Sciences Meeting and Exhibit*, Reno, Nevada, U.S.A., January 2006.

[53] Dowling, A.P., and Ffowcs Williams, J.E., *"Sound and Sources of Sound"*, pp. 130–131, Ellis Horwood, 1983.

[54] Dupère, I.D.J., and Dowling, A.P., "The Absorption of Sound by Helmholtz Resonators with and without Flow", AIAA Paper 2002–2590, 8^{th} *AIAA/CEAS Aeroacoustics Conference*, Breckenridge, CO, U.S.A., June 2002.

[55] Tam, C.K.W., and Kurbatskii, K.A., "Microfluid Dynamics and Acoustics of Resonant Liners", *AIAA Journal*, Vol. 38, No. 8, August 2000, pp. 1331–1339.

[56] Jones, M.G., Tracy, M.B., Watson, W.R., and Parrott, T.L., "Effects of Liner Geometry on Acoustic Impedance", AIAA Paper 2002–2446, 8^{th} *AIAA/CEAS Aeroacoustics Conference*, Breckenridge, CO, U.S.A., June 2002.

[57] Thomas, R.H., Choudhari, M.M., and Joslin, R.D., "Flow and Noise Control: Review and Assessment of Future Directions", NASA TM-2002-211631, April 2002.

[58] Ahuja, K.K., and Gaeta, R.J., "Active Control of Liner Impedance by Varying Perforate Orifice Geometry", NASA CR-2000–210633, December 2000.

[59] Bielak, G.W., Premo, J.W., and Hersh A.S., "Advanced Turbofan Duct Liner Concepts", NASA CR-1999–209002, February 1999.

[60] Ahuja, K.K., Cataldi, P., and Gaeta, R.J., "Sound Absorption of a 2DOF Resonant Liner With Negative Bias Flow", NASA CR-2000-210637, December 2000.

[61] Tam, C.K.W., and Auriault, L., "Time-Domain Impedance Boundary Conditions for Computational Aeroacoustics", *AIAA Journal*, Vol. 34, No. 5, May 1996, pp. 917–923.

[62] Zheng, S., and Zhuang, M., "Application and Verification of Time Domain Impedance Boundary Conditions in Multi-Dimensional Acoustic Problems", AIAA Paper 2002–2593, 2002.

[63] Zheng, S., and Zhuang, M., "Three-Dimensional Benchark Problem for Broadband Time-Domain Impedance Boundary Conditions", *AIAA Journal*, Vol. 42, No. 2, 2004, pp. 405–407.

[64] Özyörük, Y., "A Time-Domain Implementation on Surface Acoustic Impedance Condition with and without Flow", Tech. Rep. 96-1663, 1996.

[65] Özyörük, Y., "Time Domain Simulations of Radiation from Ducted Fans with Liners", Tech. Rep. 2001-2171, 2001.

[66] Özyörük, Y., Long, L.N., and Jones, M.G., "Time-Domain Numerical Simulation of a Flow-Impedance Tube", *Journal of Computational Physics*, Vol. 146, No. 5, 1998, pp. 29–57.

[67] Özyörük, Y., and Long, L.N., "Time-Domain Calculation of Sound Propagation in Lined Ducts with Sheared Flows", *AIAA Journal*, Vol. 38, No. 5, May 2000, pp. 768–773.

[68] Fung, K.-Y., Ju, H., and Tallapragada, B., "Impedance and Its Time-Domain Extensions", *AIAA Journal*, Vol. 38, No. 1, January 2000, pp. 30–38.

[69] Fung, K.-Y., Ju, H., "Broadband Time-Domain Impedance Models", *AIAA Journal*, Vol. 39, No. 8, January 2001, pp. 1449–1454.

[70] Ju, H., and Fung, K.-Y., "A Time-Domain Method for Duct Acoustics", *Journal of Sound and Vibration*, Vol. 237, No. 4, 2000, pp. 667–681.

[71] Ju, H., and Fung, K.-Y., "Time-Domain Impedance Boundary Conditions with Mean Flow Effects", *AIAA Journal*, Vol. 39, No. 9, September 2001, pp. 1683–1690.

[72] Ju, H., and Fung, K.-Y., "Time-Domain Simulation of Acoustics Sources over an Impedance Plane", *Journal of Computational Acoustics*, Vol. 10, No. 3, 2002, pp. 311–329.

[73] Visbal, M. R. and Gaitonde, D. V., "High-Order Accurate Methods for Unsteady Vortical Flows on Curvilinear Meshes", AIAA Paper 98-0131, 1998.

[74] Yoon, S. and Jameson, A., "Lower-Upper Symmetric Gauss-Seidel Method for the Euler and Navier-Stokes Equations", AIAA Paper 1987–0600, 1987.

[75] Jameson, A., "Time Dependent Calculations using Multigrid with Applications to Unsteady Flows past Airfoils and Wings", AIAA Paper 1991-1956, 1991.

[76] Li, J., Li, F. and E, Q., "A Fully Implicit Method for Steady and Unsteady Viscous Flow Simulations", *International Journal for Numerical Methods in Fluids*, Vol. 43, 2003, pp. 147–163.

[77] Visbal, M.R. and Rizzetta, D.P., "Large-Eddy Simulation on Curvilinear Grids using Compact Differencing and Filtering Schemes", *Journal of Fluids Engineering*, Vol. 124, No. 4, 2003, pp. 836–847.

[78] Rizzetta, D.P., Visbal, M.R. and Blaisdell, G.A., "A Time-Implicit High-Order Compact Differencing and Filtering Scheme for Large-Eddy Simulation", *International Journal of Numerical Methods in Fluids*, Vol. 42, 2003, pp. 665–693.

[79] Spalart, P.R., and Allmaras, S.R., "A One-Equation Turbulence Model for Aerodynamic Flows", AIAA Paper 92–0439, January 1992.

[80] Smagorinsky, J.S., "General Circulation Experiments with the Primitive Equations", *Monthly Weather Review*, Vol. 91, No. 3, 1963, pp. 99–165.

[81] Wasistho, B., Guerts, B. J. and Kuerten, J. G. M., "Simulation Techniques for Spatially evolving Instabilities in Compressible Flow over a Flat Plate", *Computers and Fluids*, Vol. 7, 1997, pp. 713–739.

[82] Ewert, R., and Schröder, W., "Acoustic Perturbation Equations Based on Flow Decomposition via Source Filtering", *Journal of Computational Physics*, Vol. 188, No. 2, 2003, pp. 365–398.

[83] Brentner, K.S., and Farassat, F., "Analytical Comparison of the Acoustic Analogy and Kirchhoff Formulation for Moving Surfaces", *AIAA Journal*, Vol. 36, No. 8, August 1998, pp. 1379–1386.

[84] Farassat, F., "Theory of Noise Generation from Moving Bodies with an Application to Helicopter Roters", NASA TR R451, 1975.

[85] Brentner, K. S., "Prediction of Helicopter Discrete Frequency Rotor Noise - A Computer Program Incorporation Realistic Blade Motions and Advanced Acoustic Formulation", NASA TM-87721, 1986.

[86] Ffowcs Williams, J.E., and Hall, L.H., "Aerodynamic Sound Generation by Turbulent Flow in the Vicinity of a Scattering Half Plane", *Journal of Fluid Mechanics*, Vol. 40, No. 4, 1970, pp. 657–670.

[87] Molin, N., and Roger, M., "Use of Amiet's Methods in Predicting the Noise from 2D High Lift Devices", AIAA Paper 2000–2064, 2000.

[88] Amiet, R.K., "Noise Due to Turbulent Flow Past a Trailing Edge", *Journal of Sound and Vibration*, Vol. 47, 1976, pp. 387–393.

[89] Jenkins, L. N., Khorrami, M. R., and Choudhari, M., "Characterization of Unsteady Flow Structures Near Leading-Edge Slat: Part I. PIV Measurements", AIAA Paper 2004-2801, 2004.

[90] Hammond, D. A. and Redekopp, L. G., "Global Dynamics of Symmetric and Asymmetric Wakes", *Journal of Fluid Mechanics*, Vol. 331, 1997, pp. 231–260.

[91] Woodley, B. M. and Peake, N., "Global Linear Stability Analysis of Thin Aerofoil Wakes", *Journal of Fluid Mechanics*, Vol. 339, 1997, pp. 239–260.

[92] Kurze, U. J. and Allen, C. H., "Influence of Flow and High Sound Level on the Attenuation in a Lined Duct", *The Journal of the Acoustic Society of America*, Vol. 49, No. 5, 1971, pp. 1643–1654.

[93] Casper, J.H., Lockard D.P., Khorrami M.R., and Streett C.L., "Investigation of Volumetric Sources in Airframe Noise Simulations", AIAA Paper 2004–2805, 10^{th} *AIAA/CEAS Aeroacoustics Conference*, 2004.

[94] Ewert, R., and Schröder, W., "On the Simulation of Trailing Edge Noise with a Hybrid LES/APE Method", *Journal of Sound and Vibration*, Vol. 270, No. 3, 2004, pp. 509–524.

[95] Khorrami, M.R., Choudhari, M. M., and Jenkins, L. N., "Characterization of Unsteady Flow Structures Near Leading Edge Slat: Part II. 2D Computaions", AIAA Paper 2004-2802, 10^{th} *AIAA/CEAS Aeroacoustics Conference*, Manchester U.K., May 2004.

[96] Agarwal, A., and Morris, P. J., "Prediction Method for Broadband Noise from Unsteady Flow in a Slat Cove", *AIAA Journal*, Vol. 44, No. 2, 2006, pp. 301–310.

[97] Bailly, C., Lafon, P., and Candel, S., "A Stochastic Approach to Compute Noise Generation and Radiation of Free Turbulent Flows", AIAA Paper 1995-092, June 1995.

[98] Bailly, C ., Lafon, P., and Candel, S., "Computation of Noise Generation and Propagation for Free and Confined Turbulent Flows", AIAA Paper 1996-1732, May 1996.

[99] Bailly, C., and Juvé, D., "A Stochastic Approach to Compute Subsonic Noise using Linearized Euler's Equations", AIAA Paper 1999-1872, May 1999.

[100] Billson M., Eriksson L., and Davidson L., "Jet Noise Prediction using Stochastic Turbulence Modeling", AIAA paper 2003–3282, May 2003.

[101] Möhring, W., "On Vortex Sound at Low Mach Number", *Journal of Fluid Mechanics*, Vol. 85, 1978, pp. 685–691.

[102] Müller, E. A. and Obermeierm F., "The Spinning Vortices as a Source of Sound", *AGARD CP-22*, 1967, pp. 22.1–22.8.

[103] Lee, D. and Koo, S., "Numerical Study of Sound Generation due to a Spinning Vortex Pair", *AIAA Journal*, Vol. 33, No. 1, 1995, pp. 20–26.

[104] Ekaterinaris, J., "An Upwind Scheme for the Computation of Acoustic Field Generated by Incompressible Flow", AIAA Paper 1997–0022, 35^{th} *Aerospace Science Meeting and Exhibition*, 1997.

[105] Ekaterinaris, J., "A New Formulation of the Equations Governing Acoustic Disturbances Generated by Unsteady Low Speed Flows", AIAA Paper 1997–1627, 3^{rd} *AIAA/CEAS Aeroacoustic Conference*, 1997.

[106] Ekaterinaris, J., "New Formulation of Hardin-Pope Equations for Aeroacoustics", *AIAA Journal*, Vol. 37, No. 9, 1999, pp. 1033–1039.

[107] Hardin, J. C. and Pope, S. D., "An Acoustic/Viscous Splitting Technique for Computational Aeroacoustics", *Theor. and Computational Fluid Dynamics*, Vol. 6, 1994, pp. 334–340.

[108] Mankbadi, R., Hayder, M., and Povinelli, L., "Structure of Supersonic Jet Flow and Its Radiated Sound", *AIAA Journal*, Vol. 32, No. 5, 1994, pp. 897–906.

[109] Motsinger, R. E., and Kraft. R. E., *"Aeroacoustics of Flight Vehicles: Theory and Practice"*, chapter Design and Performance of Duct Acoustic Treatment, p. 184, NASA RP-1258, 1991.

[110] Spalart, P.R., "Young-Person's Guide to Detached Eddy Simulation Grids", NASA Technical Report CR-2001-211032, July 2001.

[111] Delcayre, F., and Dubief, Y., "On Coherent-Vortex Identification in Turbulence", *Journal of Turbulence*, Vol. 1, No. 11, 2000, pp. 1–22.

[112] Woodward, D.S., and Lean, D.E., "Where is High-Lift Today - A Review of past UK Research Programmes", *AGARD CP 515, High-Lift System Aerodynamics*, September 1993, pp. 1/1–37.

[113] Dobrzynski, W., and Pott-Pollenske, M., "Slat Noise Source Studies for Farfield Noise Prediction", AIAA Paper 2001–2158, 7^{th} *AIAA/CEAS Aeroacoustics Conference*, Maastricht, The Netherlands, May 2001.

[114] Khorrami, M. R., and Choudhari, M. M, "Application of Passive Porous Treatment to Slat Trailing Edge Noise", Nasa/tm -2003-212416, 2003.

[115] Germano M., Piomelli U., Moin P., and Cabot W., "A Dynamic Subgrid-scale Eddy Viscosity Model", *Physics of Fluids A*, Vol. 3, No. 7, 1991, pp. 1760–1765.

[116] Moin P., Squires W., Cabot W., and Lee S. , "A Dynamic Subgrid-scale Model for Compressible Turbulence and Scalar Transport", *Physics of Fluids A*, Vol. 3, No. 11, 1991, pp. 2746–2757.

[117] Parrott, T.L., Watson, W.R., and Jones, M.G., "Experimental Validation of a Two-Dimensional Shear Flow Model For Determining Acoustic Impedance", NASA TP-1987–2679, 1987.

[118] Dowling, A.P., and Ffowcs Williams, J.E., *"Sound and Sources of Sound"*, pp. 207–208, Ellis Horwood, 1983.

[119] Cox, J.S., Brentner, K.S. and Rumsey, C.L., "Computation of Vortex Shedding and Radiated Sound for a Circular Cylinder: Subcritical to Transcritical Reynolds Numbers", *Theoretical and Computational Fluid Dynamics*, Vol. 12, 1998, pp. 233–253.

[120] Zhang, H., Fey, U., Noack, B.R., Knig, M. and Eckelmann, H., "On the Transition of the Cylinder Wake", *Physics of Fluids*, Vol. 7, No. 4, April 1995, pp. 779–794.

[121] Williamson, C.H.K., "Oblique and Parallel Modes of Vortex Shedding in the Wake of a Circular Cylinder at Low Reynolds Number", *Journal of Fluid Mechanics*, Vol. 206, 1989, pp. 579–627.

[122] Persillon A. and Braza, M., "Physical Analysis of the Transition to Turbulence in the Wake of a Circular Cylinder by Three-dimensional Navier-Stokes Simulation", *Journal of Fluid Mechanics*, Vol. 365, 1998, pp. 23–88.

[123] Kravchenko, A.G., Moin, P. and Shariff, K., "B-spline Method and Zonal Grids for Simulations of Complex Turbulent Flows", *Journal of Computational Physics*, Vol. 151, 1999, pp. 757–789.

[124] Posdziech, O. and Grundmann, R., "Numerical Simulation of the Flow around an Infinitely Long Circular Cylinder in the Transition Regime", *Theoretical and Computational Fluid Dynamics*, Vol. 15, No. 2, 2001, pp. 121–141.